Diplomarbeit

ESTABLISHMENT OF A WORKFLOW FOR HIGH RESOLUTION VISUALIZATION OF IRON DEPOSITS IN THE HUMAN BRAIN BY ANALYTICAL ELECTRON MICROSCOPY

eingereicht von

Daniel Funk

zur Erlangung des akademischen Grades

Doktor der gesamten Heilkunde

(Dr. med. univ.)

an der

Medizinischen Universität Graz

ausgeführt am

Institut für Zellbiologie, Histologie und Embryologie

unter der Anleitung von

Assoz. Prof. Priv.-Doz. Mag. Dr.rer.nat. Gerd Leitinger

Assoz. Prof. Univ.-Doz. Dipl.-Ing. Dr. Stefan Ropele

Graz, am 26.06.2018

Eidesstattliche Erklärung

Ich erkläre ehrenwörtlich, dass ich die vorliegende Arbeit selbstständig und ohne fremde Hilfe verfasst habe, andere als die angegebenen Quellen nicht verwendet habe und die den benutzten Quellen wörtlich oder inhaltlich entnommenen Stellen als solche kenntlich gemacht habe.

Graz, am 26.06.2018 *Daniel Funk eh*

Acknowledgements

First, I would like to thank Prof. Gerd Leitinger for his initial approach regarding the project, the opportunity, confidence, support and patience he gave while conducting the research presented in this paper, and thank you to my second advisor, Prof. Ropele, for his interest and input in the progress.
I would like to thank all the members of my family for the support they gave me on the long journey at the Medical University of Graz.

Furthermore, I would like to give my acknowledgements to all the other great people who supported my diploma thesis in all various kinds of ways:

- Elisabeth Bock for supplying me with all available samples at all times.
- Rudi Schmidt for his constant availability, incredible patience and calmness in assisting me with all kinds of problems regarding electron microscopy techniques and errors in the software.
- Elisabeth Pritz and Dominique Pernitsch for always caring for proper nitrogen cooling in the days prior to my EDX sessions.
- Gig Searle, Michaela Wernbacher and my father Dan Funk for the English proof reading of the final version.
- My colleague Daniel Havas for his input on statistical analysis (especially for bringing me to the point of considering pseudo-replication in neuroscience) and advice regarding the possibilities and limitations of image particle analysis.
- All other members and affiliates of the Institute of Cell Biology, Histology and Embryology who I gratefully got to know at various meetings at the institute.

For someone who has been focused on clinical research in the past, working in fundamental research and being able to draw the translational line between the two fields, has been an intense experience for me - I wouldn’t want to have missed it in any way, despite the challenges and the extensive time exposure it took to finalize this project. Thanks for being part of the way.

Table of Contents

Zusammenfassung

Einleitung: Eisen ist ein essentielles Spurenelement in Säugetieren und obligatorisch für die Funktionserhaltung lebender Zellen. Ein Übermaß an Eisen kann jedoch zu diversen Krankheitsbildern führen, wobei vor allem Eisen-Überladung im Gehirn durch oxidative Stressreaktionen eine Neurodegeneration verursachen kann. Mehrere neurologische Erkrankungen, einschließlich Morbus Alzheimer, Parkinson und Multiple Sklerose wurden mit erhöhter Eisenakkumulation im Gehirn in Verbindung gebracht. Bis heute ist nur wenig über die Zellen, sowie deren unterliegenden subzellulären Strukturen, die im Alterungsprozess zu Eisenablagerungen im Gehirn führen, bekannt. Eine Studie soll die kausale Rolle der Eisenablagerungen mit elektronenmikroskopischen Verfahren in Korrelation mit Magnetresonanztomographie und Massen-spektrometrie elaborieren.

Ziele: Postmortale Hirnproben von älteren PatientInnen, die an keiner neurologischen Erkrankung litten, wurden für die bevorstehende multidisziplinäre Studie bereitgestellt. Die vorliegende Diplomarbeit ist eine Machbarkeitsstudie mit Fokus auf den elektronenmikroskopischen Verfahren. Weiters diente die Diplomarbeit der Ausarbeitung eines Workflows in Hinsicht auf die Bilderfassung, das Datenmanagement und der statistischen Evaluierungsmöglichkeiten.

Methoden: Für die hochauflösende Visualisierung des Eisengehaltes wurde eine Kombination aus elektronenmikroskopischen Methoden angewandt: Bilder wurden mittels energiegefilterter Transmissionselektronenmikroskopie (EFTEM) akquiriert, um die Verteilung der Übergangsmetalle innerhalb der Zellen und der subzellulären Strukturen zu visualisieren, und energiedispersive Röntgen-mikroanalyse (EDX) wurde verwendet, um Spektrenanalysen von Eisen im Gehirn anzufertigen. Die Datenbank “DATEM“ wurde angelegt, um einen konsistenten Überblick auf die Bilder zu gewährleisten, und eine Musterbildanalyse inklusive statistischer Auswertungen wurde durchgeführt.

Schlussfolgerung: EFTEM zeigte sich als geeignet für den Nachweis von Eisen in biologischen Proben. Sofern Osmiumtetroxid als Fixierungschemikalie eingesetzt wird, sollte der Eisen L-Peak verwendet werden, um Überlappungen zu vermeiden. DATEM als Datenmanagement-Tool bietet einen flexiblen und

adaptierbaren Überblick auf die akquirierten Bilder zur Weiterverarbeitung. In den Beispielbildern wurde das meiste mutmaßliche Eisen in Lipofuszingranula, deren zugrundeliegenden Lipidtröpfchen, sowie in Myelinscheiden und Oligodendrozyten detektiert. Diese Ergebnisse sind aber möglicherweise darauf zurückzuführen, dass für die Musterbilder der Eisen M Peak verwendet wurde, welcher Überschneidungen mit Osmium aufweist.
Schlagwörter: Eisenablagerung, Eisen im Gehirn, EFTEM, Elektronen-mikroskopie

Abstract

BACKGROUND: Iron is an essential trace element in the mammalian body and is required for the functioning of living cells. However, excess iron may lead to several distinct disorders, and – especially iron overload in the brain – may cause neurodegeneration by oxidative stress reactions. Several neurological diseases, including Alzheimer's Disease, Parkinson's Disease and Multiple Sclerosis were proposed to be associated with elevated brain iron accumulation. To date, little is known about cells and the underlying subcellular structures involved in brain iron accumulation at advancing age. A forthcoming research study will elaborate the role of iron accumulation using electron microscopy methods in correlation with MRI and mass spectrometry.

OBJECTIVE: Post-mortem brain samples of aged patients not suffering from neurological diseases were obtained for the upcoming, multidisciplinary study. This diploma thesis is a feasibility study and focuses on the electron microscopy methods to be used, with the intention of establishing a workflow in terms of image acquisition, data management and statistical evaluation.

METHODS: For high resolution visualization of potential iron content, a combination of transmission electron microscopy methods were used: Energy filtered transmission electron microscopy (EFTEM) images were acquired for elemental distribution maps of cells and structures, and energy dispersive X-ray (EDX) was used for spectra analysis of transition metal content in the brain. A database (DATEM) for the overview of the images was set-up and a sample image analysis, including statistical evaluation, performed.

CONCLUSION: EFTEM is suitable for detection of iron particles in biological samples. However, if osmium-tetroxide is utilized as a fixation chemical, the iron L peak should be used to avoid overlaps. DATEM as a data management tool offers a flexible and adaptable overview of acquired images for processing. In the sample images, most putative iron was found in lipofuscin granules and their underlying lipid droplets, as well as in the myelin sheaths and oligodendrocytes. This, however, might be because the iron M peak was used for the sample image acquisition, which was found to overlap with the osmium peak.

Keywords: Iron Accumulation, Brain Iron, EFTEM, Electron Microscopy

REMARK

A computational transition of comma (,) and dot (.) for decimal numbers was not feasible within the German versions of MS Access and SPSS. Therefore, all decimal numbers within the present diploma thesis will be displayed with a comma, according to the ÖNORM A 1080 of the Austrian Standards Institute.

Abbreviations

AC	Astrocyte
Acp	Astrocytic Process
AD	Alzheimer's Disease
ALS	Amyotrophic Lateral Sclerosis
AX	Axon
Axp	Axoplasm
BBB	Blood Brain Barrier
CC	Corpus Callosum
CCD	Charge-coupled device
CNS	Central Nervous System
CSF	Cerebrospinal Fluid
DATEM	Data(base) Analysis in Transmission Electron Microscopy
DMT	Divalent Metal Transporter
DN	Dendrite
DNA	Deoxyribonucleic acid
Ds	Dendritic Spines
eCRF	Electronic Case Report Form
EELS	electron energy-loss spectroscopy
EDX	Energy – dispersive X ray spectroscopy
EFTEM	Energy-filtered transmission electron microscopy
EM	Electron Microscopy
ERK	Extracellular Signal-regulated Kinase
FA	Friedreich's Ataxia
FC	Frontal Cortex
Fe^{2+}	Ferrous Iron
Fe^{3+}	Ferric Iron
FFT	Fast-Fourier-Transformation
FHC	ferritin H chain
FLC	ferritin L chain
Ft	Ferritin
FtMt	Mitochondrial ferritin
FWM	Frontal White Matter
Gl	Glycogen
GP	Globus pallidus
HAADF	High-angle annular dark field
HC	Healthy control
HD	Huntington's Disease
Hm	Hemosiderin
IL-6	Interleukin-6
Ld	Lipid droplets
Lg	Lipofuscin granules

Mc	Mitochondrium
MRI	magnetic resonance imaging
MS	Multiple Sclerosis
Ms	Myelin sheath
NBIA	Neurodegeneration with Brain Iron Accumulation
Nc	Nucleus
Nrt	Neurite
NTBI	non-transferrin-bound iron
$O_2^{\bullet-}$	Superoxide radical
OC	Occipital Cortex
OD	Oligodendrocyte
Odp	Oligodendrocitic process
OWM	Occipital White Matter
PD	Parkinson's Disease
PT	Putamen
QSM	Quantitative Susceptibility Mapping
ROI	Region of Interest
ROS	Reactive Oxygen Species
STEM	Scanning Transmission Electron Microscopy
Sy	Synapse
Tf	Transferrin
TfRs	Transferrin receptors
TNF	Tumor necrosis factor

Table of Figures

List of Tables

1 Introduction

In the late nineteenth century, the first quantitative research on iron (Fe) in the human brain was conducted and revealed that non-heme iron can also be found within the central nervous system (CNS) (1). Later it was shown that, as within the rest of the body, the amount of iron is strictly balanced within the nervous system and that disturbances of brain iron homeostasis may occur at several stages in iron metabolism, including uptake and release, storage, intracellular metabolism, and regulation (2). While several neurologic diseases of both inflammatory and neurodegenerative etiology are presumably associated with defects of cerebral iron hemostasis, little is yet known about brain iron accumulation and cellular distribution of iron particles within the senescent human brain. Parkinson's Disease (PD), Alzheimer's Disease (AD), Friedreich's Ataxia (FA), Amyotrophic Lateral Sclerosis (ALS), neurodegeneration with brain iron accumulation (NBIA) and Huntington's Disease (HD) have all been correlated with brain iron dysregulation compared to the normal population (3). What remains clear to this date is that excess iron in brain parenchyma consequently leads to neurodegeneration. In order to clarify the pathogenic factor of increased iron accumulation in neurodegenerative diseases, a correlative, multidisciplinary research study consisting of three parts is being conducted by the Institute of Cell Biology, Embrology and Histology at the Medical University of Graz (electron microscopy section), the department for Neurology at the University Hospital Graz (magnetic resonance imaging section) and the Institute for Analytical Chemistry at the Karl-Franzens University of Graz (mass spectrometry section). This diploma thesis focuses on the methodology of the electron microscopy section of the upcoming study.

1.1 Iron Metabolism

Iron is an essential element for processes in living cells, including oxygen transport, oxidative phosphorylation and DNA biosynthesis (4). External iron intake is a fundamental part of adequate nutrition and is necessary for the development and maintenance of neurodevelopmental functions (5). The mammalian body follows a strict order to keep an equilibrium between absorption and excretion of iron, as low body concentrations cause iron-deficiency anemia and increased iron concentrations result in siderosis (6). Iron is distributed within the mammalian body in two different types, heme and non-heme compounds. Heme iron is found within proteins such as myoglobin or hemoglobin, and non-heme iron is linked to several iron regulatory proteins (7). Whilst it is estimated that heme iron contributes to over 40% of total absorbed iron, non-heme iron is absorbed less in the body (8). Non-heme iron is present within the mammalian body in two physical states (7): ferrous iron (Fe^{2+}) and ferric iron (Fe^{3+}). In the small intestine, iron is absorbed by enterocytes with the assistance of divalent metal transporter 1 (DMT-1), especially in the duodenum and jejunum (9). The non-bioavailable oxidized Fe^{3+} form must be transformed to its Fe^{2+} form by reduction through *ferrireductase* prior to transportation into enterocytes through DMT-1 (10). The enzyme *heme oxygenase* causes iron to leave enterocytes and enter the blood plasma in form of non-heme iron (6).

In contrast to iron's major role in essential cellular functions, it is also notorious for creating the cytotoxic radical superoxide and radical hydroxide (11), which cause severe cell damage in organs. To prevent iron from damaging cells, it must be bound to proteins to impede formation of free radicals (12). In the mammalian body *transferrin*, which is responsible for iron uptake and transport, and *ferritin*, the protein involved in intracellular iron storage, can be found (13). *Transferrin* (Tf) is a glycoprotein in the plasma and interstitial fluids (14) and serves as the main transporter of Fe^{3+} to cells which express transferrin receptors (TfRs) (15). Whenever circulating in the vascular system, iron is bound to *transferrin* (10). *Ferritin* (Ft) - as the most abundant non-heme compound - acts as the major intracellular protein involved in iron storage and is found in cell cytoplasm, nuclei

and mitochondria (4). Ft is a spherical molecule consisting of two major types, ferritin H chain (FHC) and ferritin L chain (FLC) (16). While *ferritin* was previously only considered responsible for the storage of iron, research conducted on mice found it to also trigger iron deposition, whereas uptake is presumed higher for FHC (17). *Hemosiderin* (Hm) is a non-soluble protein proposed as a proteolytic product of ferritin and is referred to as the second iron storage molecule within the body (18). Increased presence can be detected in pathological iron deposition as well as associated diseases as hemochromatosis and siderosis (18). Mitochondria contain their own iron-storage ferritin, which is referred to as mitochondrial ferritin (FtMt) (19). FtMt not only serves as protection for mitochondria against oxidative damage resulting from iron overload (20), but also plays a vital role in homeostasis of cytosolic and mitochondrial iron distribution (19).

1.2 Iron in the Brain

Iron is required in the brain for metabolic processes such as neurotransmitter production and myelinogenesis (4), and is highly depending on regulation, as both iron deficiency as iron excess may lead to tissue damage (14). In the CNS, iron is essential for the non-heme enzyme ribonucleotide reductase, which is involved in cell division and DNA synthesis (5, 11). In order for iron to pass through the blood brain barrier (BBB), complex transcellular processes come into play (15). The majority of iron transport from blood to the brain is the result of receptor-mediated endocytosis of transferrin by brain vascular endothelial cells (21), where iron is released from transferrin, which is then recycled to the blood (14). As a second mechanism, iron transport to the brain also results from a receptor-mediated transcytosis across the capillary wall (14). Iron uptake into neurons and glial cells is thought to be controlled by the number of transferrin receptors and therefore dependent on the amount of iron present (14). Transferrin however is abundantly traceable in oligodendrocytes within the CNS (22), while transferrin receptors can be found in brain capillary endothelial cells, choroid plexus epithelial cells and neurons within the brain (14). Fe-transfer via transferrin through the blood-cerebrospinal fluid barrier has been described, proposedly due to the transferrin

receptors on the choroid plexus epithelial cells (14). DMT-1 is also responsible for iron uptake in brain cells and is predominantly available in neurons (23).

Observation showed that receptor-mediated and clathrin-dependent transcytosis of ferritin in BBB cell culture models were required for iron to be deposited in the brain (17). Ji et al further proposed that *lactoferrin* as a ligand might play a role in the reported *ferritin* crossing the BBB (24). In the human brain, *ferritin* is expressed within oligodendrocytes, microglia, and neurons (22). Next to *ferritin*, also *hemosiderin* is considered to be a molecule involved in brain iron storage (18),(25).

1.3 Iron in Neurodegeneration

In the process of aging, the human body constantly loses the ability to remove toxic compounds and supply the brain with relevant nutritional factors, with both the BBB and the blood-cerebrospinal fluid barrier increasing in their permeability (26). Elevated brain iron accumulation is often associated with neurodegenerative diseases such as PD, AD and HD, whereas its distinct coherence to disease progression remains unknown (27). Nevertheless, a negative correlation between brain iron accumulation and cognitive functions has been proposed (28). Generally, iron carries neuro-damaging properties which unfold through the Fenton (***Figure 1***) and Haber-Weiss reactions, in which reactive oxygen species (ROS) such as superoxide and hydroxyl radical are produced (12, 29). Therefore, elevated intra-cellular iron accumulation causes oxidative stress and leads to neuronal dysfunction and degeneration (27). Furthermore, it is also hypothesized that intracellular calcium release, which is triggered via Extracellular Signal-regulated Kinase (ERK) signaling pathway by iron-generated ROS, might be an additional contributive factor to neurodegeneration (30, 31).

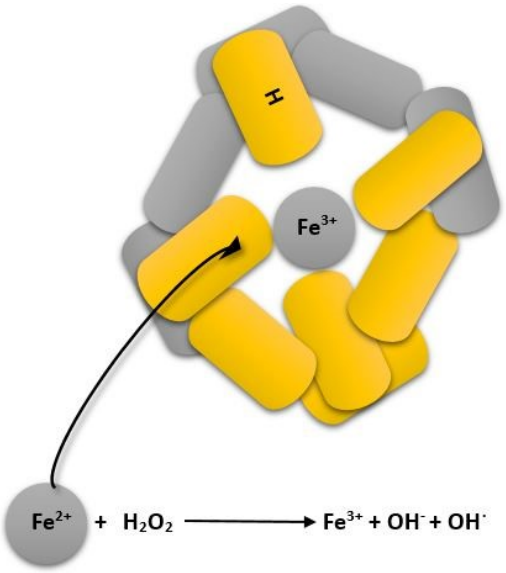

Figure 1: Fenton reaction in Iron Neurodegeneration
Image adapted from (4): Reduction of ferric iron (Fe^{3+}) to ferrous iron (Fe^{2+}) by the superoxide radical ($O_2^{\bullet -}$) via $Fe^{3+} + O_2^{\bullet -} \rightarrow Fe^{2+} + O_2$. Ferrous iron ($Fe^{2+}$) can also react with hydrogen peroxide (H_2O_2), generating the hydroxyl free radical ($^{\bullet}OH$) ($Fe^{2+} + H_2O_2 \rightarrow Fe^{3+} + {}^{\bullet}OH + OH^-$), known as the Fenton reaction (27). The reaction's outcomes are highly reactive oxygen species (ROS). *(modified from Batista-Nascimento (27): "Iron and Neurodegeneration: From cellular homeostasis to disease", 2012)*

With a first work published in 1947 (32), a specific group of genetically inherited diseases linked to excessive iron accumulation have put the focus of scientific research on the role of iron in cognitive decline, which are summarized as “neurodegeneration with brain iron accumulation” (NBIA) diseases (33). Currently, results of oxidative stress due to excess iron are considered as one of the pivotal elements of neurodegeneration in the aging brain (29), with authors stating that also systemic diseases as atherosclerosis, diabetes, inflammatory as well as autoimmune diseases are linked to iron dysregulation (34). In the past, results of iron accumulation resulting in oxidative stress due to Fenton’s reaction were also discussed as being hallmarks of Alzheimer’s disease and its associated neurofibrillary tangles and senile plaques (35). As for Parkinson’s Disease, reduced systemic bioavailability of iron and concurrently present excess brain iron tissue as pathogenic and exacerbating factors have been discovered in various scientific research (36-40). Histological studies conducted in 1982 had already found iron deposits in proximity to demyelinated plaques found in brains of patients suffering from multiple sclerosis (41), while recent MRI findings confirmed increased iron accumulation in cerebral structures of MS patients (42). MRI in-vivo evaluation on brain iron conducted on Alzheimer patients supported that the basal ganglia contained higher amounts of ferritin compared to healthy controls (43).

The basal ganglia are dopamine-dependent nuclei located within both brain hemispheres, which are primarily responsible for motor functions, executive functions and emotions (44). Their major components are subcortical nuclei such as globus pallidus (GP) and the striatum, consisting of the putamen (PT) and the caudate nucleus (45) (***Figure 2***). MR imaging studies conducted on AD, HD and PD patients have showed that high brain iron accumulation can be found within the basal ganglia (46, 47). The globus pallidus is regarded as a functional antagonist to the putamen and caudate nucleus (48). The GP and the substantia nigra pars reticulata, are both considered the main output nuclei in the basal ganglia system (49). The GP consist of an internal (GPi) and external segment (GPe), wheareas the GPe is considered to be involved in basal ganglia dysfunction as seen in PD (50). Previous research on iron in the globus pallidus

indicated that iron particles are mainly distributed in the neuropil and around veins and arteries within the GP (51). The putamen is a curved structure (52) located lateral to the globus pallidus (48). It functionally belongs the basal ganglia system and is – together with the caudate nucleus - considered part of the striatum (52), one of the main input nuclei for motor function information from the cortex (53). Recent MRI studies showed increased iron content in putamen, indicating brain iron content to be positively correlated with volume decrease (54).

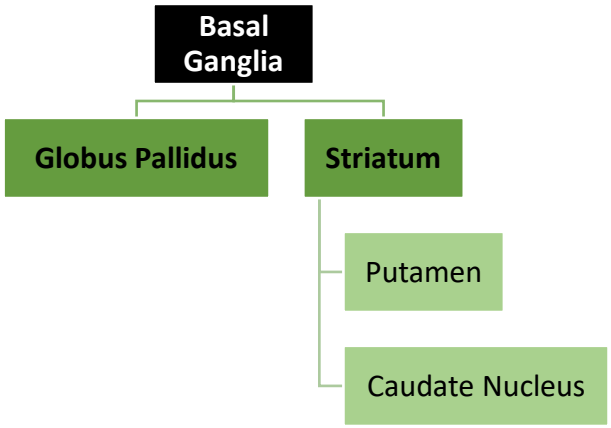

Figure 2: Functional Designation and Assignment of Basal Ganglia Nuclei

1.4 Main Cells Types within the Brain

Wherever iron is to be expected in the brain, it can potentially be found within the main cell types in the CNS. In general, even outnumbering neurons, the majority of cells in the CNS are glial cells, which can be classified as astrocytes, oligodendrocytes and microglia (55). For the electron microscopy part of the upcoming study in iron deposits, the focus should not only be put on cell types, but also on their underlying subcellular structures for quantification. Despite a variety of substructures present in cells, one can expect to see the following overlying cell types when observing nerve tissue samples on a microscopic level:

Neurons

Although neurons may differ in morphological aspects (56), most neurons exhibit dendrites, a cell body, axons, and axon terminals (57). Neuronal function is highly dependent on iron homeostasis, with iron transported into the neuron along axons

and dendrites (15). The need for internalization of iron in neurons is evident by the presence of transferrin receptors and DMT-1 on neuronal structures (58). But previous research conducted with Perl's and Turnbull's methods with light microscopy showed only low staining for iron in neurons, which was often difficult to distinguish from the surrounding neuropil, which exhibited higher staining for iron (51).

Oligodendrocytes

Oligodendroglial cells, commonly referred to as oligodendrocytes, are responsible for the formation of shovel-shaped myelin sheaths around axons (59). In myelinogenesis, iron serves as a co-factor for the biosynthesis of lipids (60), of which mainly galactosylceramide and cholesterol are created (61). In previous research on human brains, Connor et al. (62) found that in a middle-aged and older group transferrin, ferritin, and iron are found especially in the perikaryal cytoplasm of proposed oligodendrocytes in all investigated brain regions. Several other studies on cellular distribution of iron in the brain have proposed that oligodendrocytes contain the highest amount of Fe in the brain (11, 13, 60, 63, 64). Especially in white matter tracts, ferritin proposedly constitutes a main source of iron in oligodendrocytes (65).

Astrocytes

Astrocytes are glial cells found throughout the CNS and are involved in synaptic transmission and information processing (66). Furthermore, perivascular astrocytes are specifically involved in function of the blood brain barrier (67). As the most numerous glial cells in the brain, their main function is protection of neuronal function (68). Research on brain iron homeostasis suggested a major involvement of both ascorbate and DMT-1 involved in non-transferrin-bound iron accumulation into astrocytes (69). In inflammation processes, both tumor necrosis factor (TNF) and interleukin-6 (IL-6) stimulate the expression of DMT-1 in neurons and glial cells, including astrocytes (23, 70).

2 Objectives

The main objective of the present diploma thesis is a feasibility study for the main research on iron accumulation in the aging brain in order to establish a possible workflow for suitable electron microscopy methods. Two electron microscopy techniques (Energy filtered transmission electron microscopy (EFTEM) and energy dispersive X-ray spectroscopy (EDX)) were applied in the feasibility study with the objectives of answering the following research questions:

- Are EFTEM and EDX reliable for the detection of iron at a nanometer scale? Which EFTEM elemental edge is most suitable for the detection of iron?
- How can cells within EFTEM images be categorized in order to also differentiate between potential iron content in cells, cellular substructures and brain areas?
- Which techniques for image analysis are appropriate for the detection of iron in the obtained sample images?
- How can ferritin cores be quantified via image analysis and which parameters are suitable for subsequent statistical analysis?
- How can large amounts of image data be handled efficiently, especially in terms of overview, data consistency and potential statistical analysis?

3 Material

3.1 Brain Samples

Brain samples of deceased patients who underwent autopsy and did not suffer from neurological diseases were collected by the Department of Neuropathology at the University Hospital Graz. At the time of image acquisition of the sample images for the diploma thesis, samples from three brains were already available at the Institute of Cell Biology, Histology and Embryology at the Medical University of Graz. Brain samples were obtained by the Institute of Neuropathology at the University Hospital and placed into a glutaraldehyde-formaldehyde solution as soon as the pathologist released the sample. Preparation of tissue samples was performed at the Institute of Cell Biology, Histology and Embryology at the Medical University of Graz, generating a 1mm x 1mm x 1mm specimen. Fixation was performed using 2% of paraformaldehyde and 2.5% of glutaraldehyde, dissolved in cacodylate buffer. As post-fixation, 2% of osmium tetroxide in a 0.1 molar cacodylate buffer were added for membrane lipid fixation and to give subsequent contrast to images. Dehdyration was performed with an ascending alcohol series of 50%, 70% and 100%. Tissue samples were embedded in synthetic resin and cut into 0.5 µm semi-thin sections. In addition, Gallyas-Braak staining on tissue samples in order to differentiate between potential onset of Alzheimer's Disease within the brains is planned for the main study. This specific staining method has been shown to reveal Alzheimer-like neurofibrillary tangles as well as neuroglial inclusions found in diseases of brain neurodegeneration (71). However, Gallyas-Braak staining has not been applied to any tissue samples during this feasibility study.

In total, seven regions of interest were already available for acquisition of sample images: ***Corpus callosum*** (CC), ***Globus pallidus*** (GP), ***Frontal cortex*** (FC), ***Occipital cortex*** (OC), ***Frontal white matter*** (FWM), ***Occipital white matter*** (OWM), and the ***Putamen*** (PT). Most of the regions can be seen when cutting the human brain at the height of the temporal lobe (***Figure 3***).

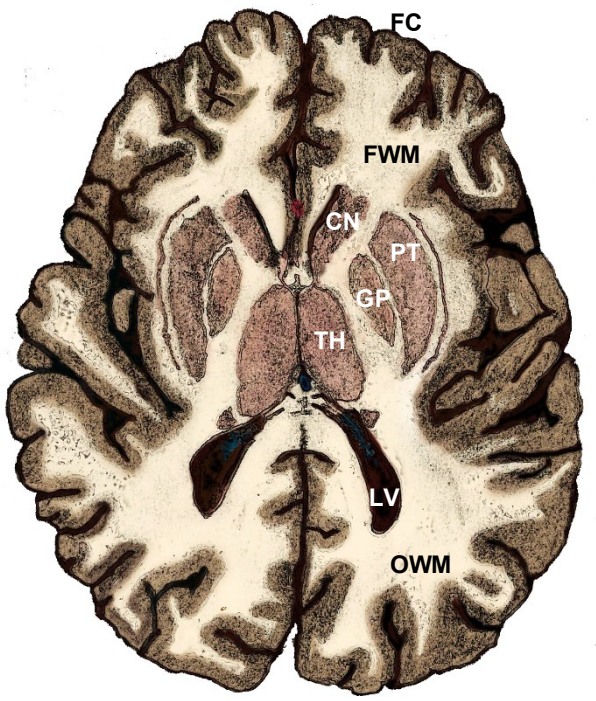

FC	Frontal Cortex
FWM	Frontal White Matter
CN	Caudate Nucleus
PT	Putamen
GP	Globus Pallidus
TH	Thalamus
LV	Lateral Ventricle
OWM	Occipital White Matter

Figure 3: Human brain cut in cranial view at edge of temporal lobe
Re-drawn and modified according to Prometheus, by D. Funk

4 Methods

Several techniques derived from transmission electron microscopy have been used in the past to detect elements in biological tissues (72-74). In order to establish a workflow for the detection of iron within human brain tissue for the upcoming study, two special transmission electron microscopy techniques were applied and compared to each other: Energy filtered TEM and X-ray spectroscopy TEM. While transmission electron microscopy images were obtained for overview of specific cells, EFTEM elemental maps were created of the same areas to detect iron. For validation purposes of the proposed iron in elemental maps, EDX spectra were obtained within the same areas that had previously been observed with EFTEM. In order to comprehend the principles of the electron microscopic methods, the underlying physical background has to be elaborated first:

4.1 Transmission Electron Microscopy

Transmission electron microscopy (TEM) has been around since the early 1940s and uses the technology of an electron beam passing through the samples in order to produce images at nanometer resolution (75). The high resolution provided by transmission electron microscopy compared to traditional light microscopic techniques enables the visualization of distinct cell structures and organelles. When electrons pass through a specimen, their direction is diverted – depending on whether the electron interacts with the atomic nucleus or its surrounding shells (K,L,M) - they can be categorized into elastically and inelastically scattered electrons (76) (***Figure 4***). The process of absorption and scattering then gives contrast to the image that can be captured by a charge couple device (CCD) camera (75).

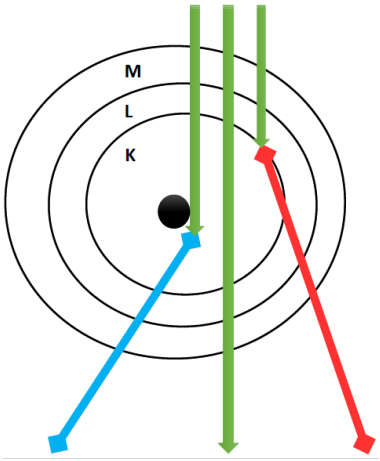

Green arrows(↓): Electrons passing through specimen.

Blue arrow (↙): Elastically scattered electron passing by the nucleus (center black dot).

Red arrow (↘): Inelastically scattered electron passing through the inner electron K-shell.

Figure 4: Electron Interaction with Specimen

4.2 Energy Filtered Transmission Electron Microscopy

Energy filtered transmission electron microscopy (EFTEM) is used in both material sciences and life sciences to acquire high resolution elemental distribution images (77). Generally, inelastically scattered electrons lose some of their kinetic energy when interacting with the specimen. This energy loss is characteristic for the chemical element that the interaction occurred with and, more specifically, for the shell of the particular electron that the interaction occurred with. The spectrometer is a device that disperses electrons according to their energy. Thus, element specific energy-loss of the electrons can be recorded, depending on the distance between these electrons and those that did not lose energy. The energy loss of the electrons passing through the specimen can either be measured and displayed in a spectrum (electron energy-loss spectroscopy (EELS)), or, for EFTEM, a retractable slit is placed into the beam below the specimen. The slit is adjusted to specify which part of the energy spectrum is used for imaging (***Figure 5***). Thus, only those electrons whose energy loss corresponds to a certain element are used for imaging and the brighter the image, the higher the concentration of this element within the sample.

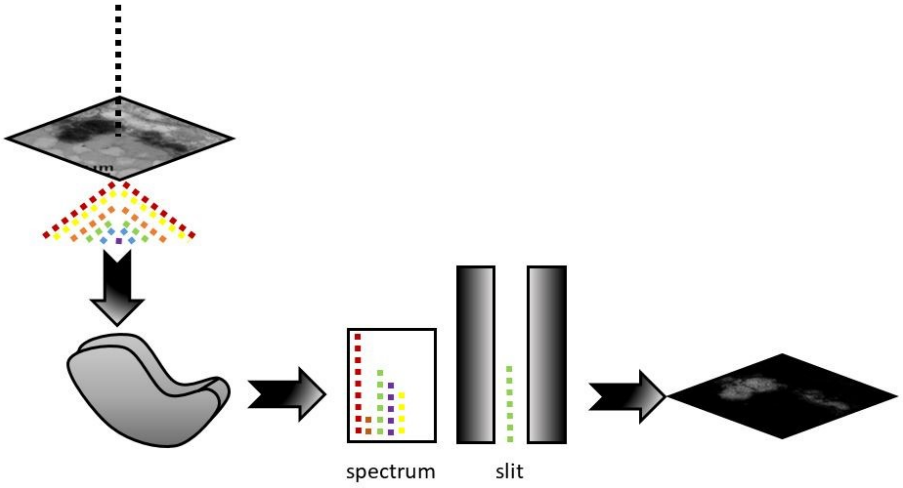

Figure 5: Principles of EFTEM
Electron beam passes through the sample and through the magnetic prism. The desired part of the spectrum is selected by the retractable energy-selecting slit. Through extrapolation of acquired images, the energy-filtered image is generated. (modified by D.Funk from Grogger, "Energy-Filtering Transmission Electron Microscopy (EFTEM) basics", Presentation by Graz University of Technology)

As EFTEM can be utilized for quantifying electron energy-loss, its elemental mapping feature is able to create images of inelastically scattered electrons. EFTEM sample images were acquired with a CCD camera with the retractable energy-selective slit (78) set for the iron peak. In the experimental setting the three-window method for elemental mapping was used, thus creating a pre-edge 1, pre-edge 2, post-edge and elemental map image (***Figure 6***). After the two pre-edge images are acquired, the extrapolated background image is subtracted from the post-edge image (79). Immediately after having applied the three-window method, the slit was placed around an energy loss of zero to cut off all the inelastically scattered electrons, and an image was made with the same field of view as before. Images created this way are termed "elastic" images, and these images were thus saved with the suffix "elastic".

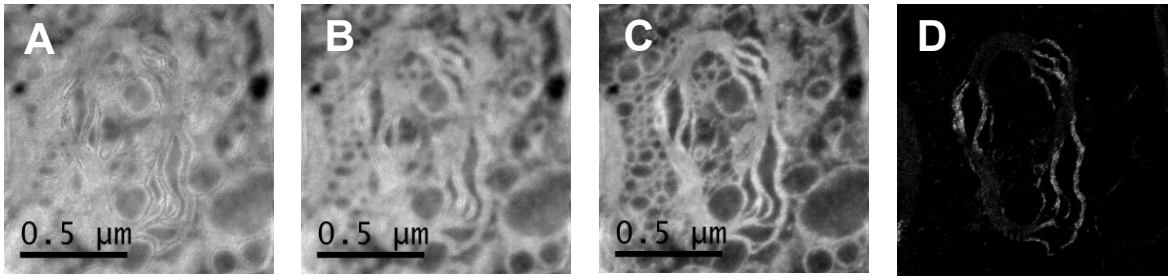

Figure 6: Three Window Method
Images represent the three window method including images of pre-edge 1 at 40 eV **(A)**, pre-edge 2 at 48 eV **(B)**, post-edge at 64 eV **(C)**. The calculated elemental map for the iron M peak constitutes the outcome of the method **(D)**. The elemental map was acquired at 19 k from an axon in the frontal white matter.

There are three major edges for iron in the EELS spectrum: L_2 at 702 eV, L_3 at 708 eV, $M_{2,3}$ at 54 eV. For purposes of the sample images, iron elemental maps at the $M_{2,3}$ edge were selected in the periodic table within Digital Micrograph elemental map settings (***Figure 7***). It was concluded after sample image acquisition that for the main study the iron L peak should be used due to observed overlaps between iron M peak and the O peak of osmium-tetroxide used in fixation. Details on this finding will be presented in the results (***section 5.2***).

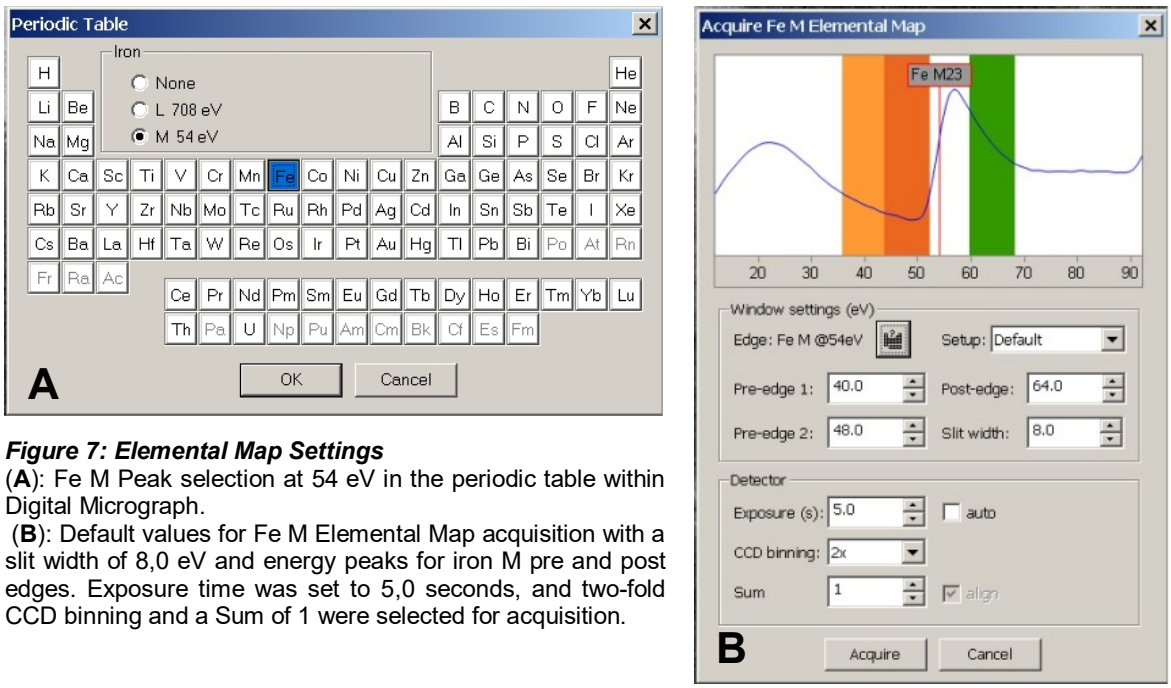

Figure 7: Elemental Map Settings
(**A**): Fe M Peak selection at 54 eV in the periodic table within Digital Micrograph.
(**B**): Default values for Fe M Elemental Map acquisition with a slit width of 8,0 eV and energy peaks for iron M pre and post edges. Exposure time was set to 5,0 seconds, and two-fold CCD binning and a Sum of 1 were selected for acquisition.

4.3 Energy Dispersive X-Ray Spectroscopy

Energy Dispersive X-Ray Spectroscopy (EDX) enables the measuring of electrons that bounce off the surface of the sample. Generally, an ionized atom may fill its vacancy by an electron jumping from an outer shell to an inner shell, thereby emitting characteristic X-ray radiation which can be measured with a detector (80). The X-ray quantum is specific for each element and is therefore used to quantify particles.

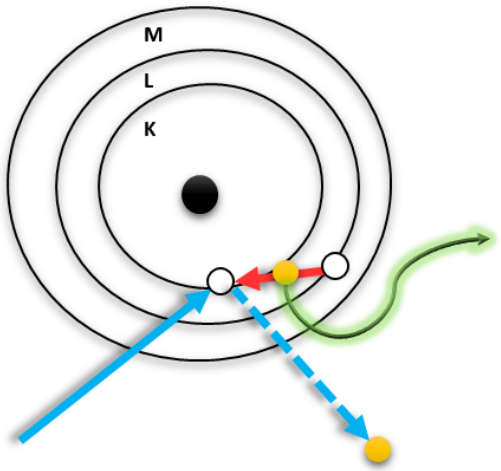

Continuous blue arrow (↗):	External stimulus on electron in inner shell
Yellow dot:	Electron
White dot:	Vacant electron
Dotted blue arrow (↘):	Electron is ejected from inner shell
Red arrow (↙):	Electron from outer shell fills hole
Green arrow:	Emitted X-ray

Figure 8: X-Ray Emission in Specimen

A specific low-background EDX holder was used when applying the EDX methods, and images were acquired in STEM (Scanning Transmission Electron Microscopy) mode with a high-angle annular dark field (HAADF) detector at a magnification of 7000x and a spectrum acquisition time of 60 seconds. EDX spectrum analyses were taken at points which, according to the previously obtained EFTEM images, have a high iron content. Additionally at each region of interest (ROI) a reference point was taken where no iron content was expected. The EDX method was used to ensure that conclusive results may be obtained regarding iron distribution maps in EFTEM mode.

4.4 Sample Image Acquisition

For sample image acquisition, the FEI Tecnai G2 20 was used at 120 kV. It was equipped with a STEM unit, a high-angle annular dark field detector (HAADF) for capturing STEM images, an energy dispersive X-ray (EDX) spectrometer for X-ray spectroscopy and a Gatan Quantum GIF energy filter for EFTEM imaging and EELS. Images were acquired with either one of two Gatan Ultrascan cameras at 1024x1024 pixels. A bottom mount camera (Gatan US 1000) was used for routine bright field imaging. For EFTEM imaging and elastic imaging, another US 1000 camera placed behind the imaging filter was used. For the latter camera, the condensor was set to EFTEM mode. The magnifications used are listed in ***Table 1***. Several software packages were used for EFTEM imaging: Tecnai User Interface (FEI) to control the microscope, TIA (TEM Imaging and Analysis, FEI) and Digital Micrograph (GATAN) to acquire the images, and Gatan Filter Control to set the filter parameters. At the beginning of each session, TEM calibration was performed with a cross-grating as a specimen.

To avoid selective bias, different regions of the grid were selected randomly at low magnification and the coordinates were saved. After switching to EFTEM mode at the selected areas the three window method was applied to the various pre-selected regions in the sample. Several images were acquired for each structure and its surroundings in EFTEM mode. The corresponding coordinates of the acquired elemental maps were saved for each structure in order to re-trace the structures in later processing. For the purpose of standardized procedures, all EFTEM images for analysis were acquired at a magnification of 19 k (which corresponds to 34 k when switching to EFTEM mode).

In the next stage, the corresponding TEM images of the previously saved coordinates were acquired in bright field TEM mode. For a general overview of the obtained structures a magnification between 5 k and 11,5 k was used. ***Table 1*** shows the respective conversion of magnifications when switching from bright field TEM to EFTEM mode, whereas magnifications not used for EFTEM are displayed as not applicable (N/A).

Table 1.: Magnifications in TEM/corresponding EFTEM magnifications

TEM	EFTEM
11,5 k	N/A
14,5 k	N/A
19 k	**34 k (standard)**
29 k	53 k
62 k	100 k

Before starting the image acquisition, the sections had do undergo a “baking” process to prevent drift. For this, the beam intensity was set to step 3, and the sample was illuminated in the beam for approximately 20 minutes at low magnification. Additionally, live Fast-Fourier Transformation (FFT) view was constantly active and objective stigmatism was corrected when needed. For each magnification change, the z-position of the specimen was set to eucentric height using the alpha wobbler. All acquired images in TEM and EFTEM were saved as Digital Micrograph *.dm3 files and were subsequently batch-converted to *.tiff format. The image file names were composed of the sample’s grid storage box number, its compartment identification letter and number combination, the sample’s brain area abbreviation, the stage coordinates identification number of the image and the magnification used (***Table 2***). As a suffix for each image in a dataset, the specification of image type was added (***Table 3***).

Table 2: Example of General Image File Name

ID	Example Data
Box number	175
Compartment Number	N1
Brain Area	PT
Saved Stage Number	009
Magnification	19 k
Image File Name:	**175_N1_PT_009_19k**

Table 3: File Name Endings for Acquired TEM and EFTEM Image Files

Image Spec		Ending
TEM		"_TEM"
EFTEM	**Zero Loss Image**	"_Elastic"
	Pre Edge 1	"_Fe Pre Edge 1"
	Pre Edge 2	"_Fe Pre Edge 2"
	Post Edge	"_Fe Post Edge"
	Elemental Map	"_Iron M Map"

4.5 Data Management

During the time of the sample image acquisition, the question of how to achieve a structured overview of datasets became inevitable. Initially, acquired images were available in a growing number within folders of Microsoft Windows (***Figure 9***). However, the conjunction of the subsequent particle analysis and their corresponding images using only their file name constituted a challenge in view of the fact that large datasets may be planned for the upcoming research.

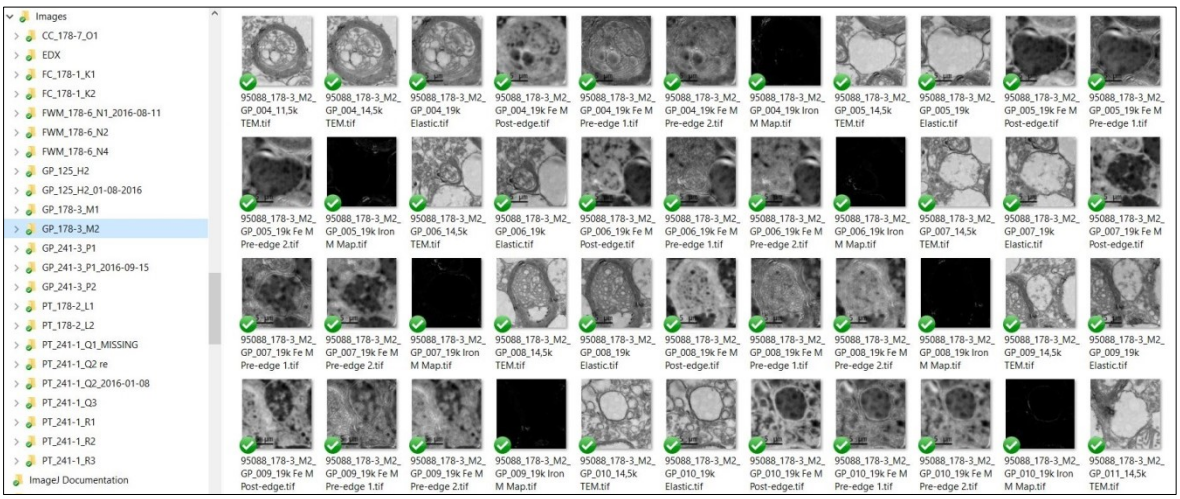

Figure 9: Windows Explorer View of Sample Images

In order to sort images, the Microsoft Access 2013 database DATEM ("*Data Acquisition for Transmission Electron Microscopy"*) was created within the scope of this diploma thesis. DATEM constitutes an electronic case report form (eCRF), allowing the saved images to be displayed with their underlying information and export the generated datasets as *.xls spreadsheets for subsequent statistical analysis. To successfully display images in DATEM, the *.tiff files were initially

downscaled to a factor of 0.25 and batch-converted into *.bmp files via the open source image processing application IrfanView 4.38 (http://irfanview.tuwien.ac.at/). ***Table 4*** summarizes the rescaled sizes of image types acquired within the study.

Table 4: Original pixel size and downscaled size for DATEM Image Import

Image Type	Original Size	Reduction Factor	DATEM Final Size
TEM	2048 x 2048 px	0,25	512 x 512 px
EFTEM	1024 x 1024 px	0,25	256 x 256 px

TEM and EFTEM sample images were then loaded into DATEM for data management and image overview, supervisor review and subsequent data output for statistical analysis. First, the overlying TEM overview images were loaded into DATEM and their corresponding brain sample, area and magnification were assigned within the database. Next, each image of the EFTEM elemental set was loaded into DATEM, which were linked via image identification (*imageid*) on a 1:n relationship. Each structure in an image that could be categorized for subsequent particle analysis was separately colored with Adobe Photoshop CS3 with low opacity and also loaded into DATEM. ***Figure 10*** shows the TEM/EFTEM images single dataset view as available in DATEM. After coloring the individual structures, image sets were uploaded to DATEM, linked to image identification on a 1:n basis. The categories of cell types and structures each (listed in ***Table 5***) were assigned to the colored images.

Table 5: Cell Types and Cell Structures for Categorization in DATEM

Cell	Full Description
AC	astrocyte
AX	axon
DN	dendrite
OD	oligodendrocyte
MG	microglial cell
UND	undefinable

Structure	Full Description
AXP	axoplasm
CP	cytoplasm
MC	mitochondrium
MS	myelin sheath
NC	nucleus
SY	synapse
ODP	oligodendrocitic process
NRT	whole neurite
ACP	astrocytic process
DS	dendritic spines
LD	lipid droplet
GL	glycogen
LG	lipofuscin granules

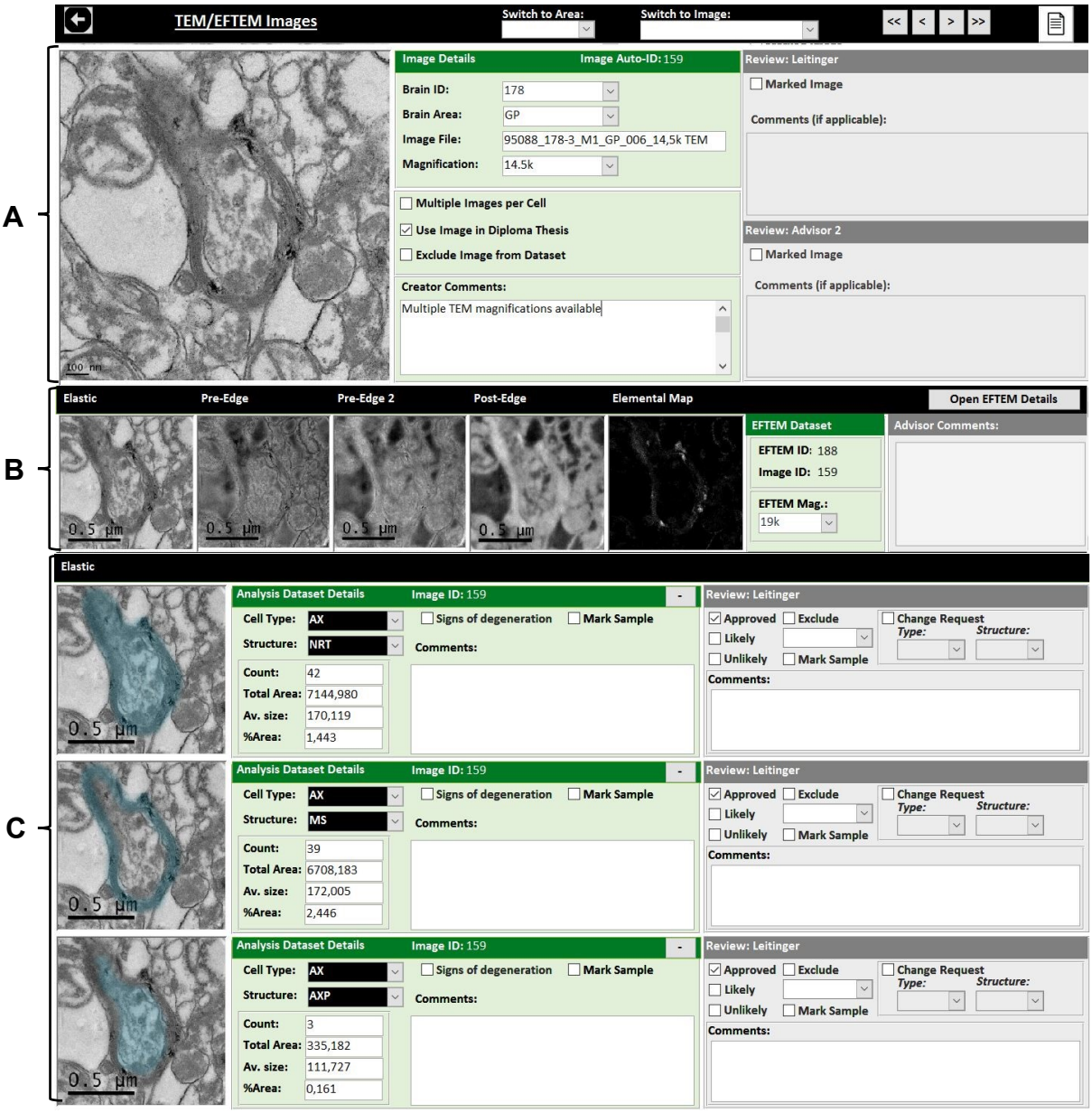

Figure 10: Total View of one Dataset in DATEM

This DATEM image was taken when being logged in with the security setting of data manager, allowing for source data to be entered (*green*). The first section (**A**) displays the uploaded TEM image with its corresponding information. The second section (**B**) includes the EFTEM dataset linked to the TEM image. The third section (**C**) incorporates the different colored structures within the Elastic EFTEM image, were cell type and structure categorization were performed and particle analysis data was entered. On the far right of the section the advisor's review section can be seen in read-only mode (*grey*).

After DATEM was populated with images and categorizations were assigned (***Figure 10***), reviews on colored structures were performed by the supervisor, by choosing from the predefined assessment scales listed within ***Table 6***. Prof. Leitinger's approval was needed for the cell type and structure specification for each acquired image used for analysis. Datasets for subsequent statistical analysis in DATEM were only exported after certification by the advisor as either "*Approved*" or "*Likely*". The change request section also allowed the advisor to give alternative proposals for different structures for assignment.

Table 6: Advisor Review Assessment Categories within DATEM

Assessment	Description
Approved	Colored area highly resembles proposed structure
Likely	Colored area possibly resembles proposed structure
Unlikely	Colored area is unlikely to be proposed structure
Change Request	Alternative proposal for structure by reviewer
Exclude	Image needs to be excluded (incl. reason for exclusion, see ***Table 7***)

In case an image was dismissed from the dataset, several reasons could be given as the exclusion criteria. ***Table 7*** shows the different reasons for excluded images for the sample dataset.

Table 7: Image Exclusion Reasons within DATEM

Assessment	Description
Duplicate Structure	Structure is already present in another image for analysis.
EFTEM not replicable	EFTEM image seems highly unreasonable (i.e. every structure visible seems stained).
Erroneous coloring	Several distinct structures were colored and wrongly categorized.
Non-standardized Magnification	Images were taken at another magnification as the defined standard (i.e. first sample images were acquired at 29 k instead of standardized 19 k).
Type/Structure undefinable	Cell type and/or structure is undefinable at currently given magnification.
Weak preservation	Structure is so weakly preserved no clear conclusions can be drawn.

Data integrity was checked on a regular basis by using the EFTEM cells data list (***Figure 11***) to look for inconsistent and missing information within datasets.

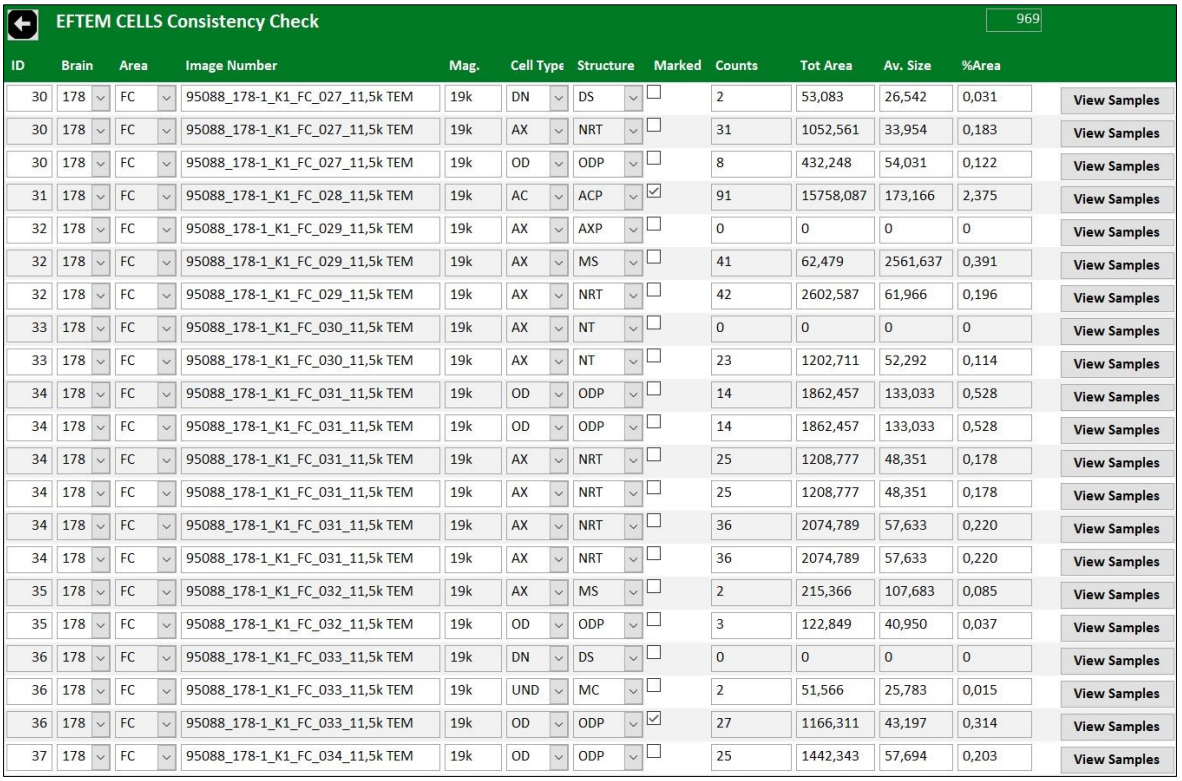

EFTEM CELLS Consistency Check 969

ID	Brain	Area	Image Number	Mag.	Cell Type	Structure	Marked	Counts	Tot Area	Av. Size	%Area	
30	178	FC	95088_178-1_K1_FC_027_11,5k TEM	19k	DN	DS	☐	2	53,083	26,542	0,031	View Samples
30	178	FC	95088_178-1_K1_FC_027_11,5k TEM	19k	AX	NRT	☐	31	1052,561	33,954	0,183	View Samples
30	178	FC	95088_178-1_K1_FC_027_11,5k TEM	19k	OD	ODP	☐	8	432,248	54,031	0,122	View Samples
31	178	FC	95088_178-1_K1_FC_028_11,5k TEM	19k	AC	ACP	☑	91	15758,087	173,166	2,375	View Samples
32	178	FC	95088_178-1_K1_FC_029_11,5k TEM	19k	AX	AXP	☐	0	0	0	0	View Samples
32	178	FC	95088_178-1_K1_FC_029_11,5k TEM	19k	AX	MS	☐	41	62,479	2561,637	0,391	View Samples
32	178	FC	95088_178-1_K1_FC_029_11,5k TEM	19k	AX	NRT	☐	42	2602,587	61,966	0,196	View Samples
33	178	FC	95088_178-1_K1_FC_030_11,5k TEM	19k	AX	NT	☐	0	0	0	0	View Samples
33	178	FC	95088_178-1_K1_FC_030_11,5k TEM	19k	AX	NT	☐	23	1202,711	52,292	0,114	View Samples
34	178	FC	95088_178-1_K1_FC_031_11,5k TEM	19k	OD	ODP	☐	14	1862,457	133,033	0,528	View Samples
34	178	FC	95088_178-1_K1_FC_031_11,5k TEM	19k	OD	ODP	☐	14	1862,457	133,033	0,528	View Samples
34	178	FC	95088_178-1_K1_FC_031_11,5k TEM	19k	AX	NRT	☐	25	1208,777	48,351	0,178	View Samples
34	178	FC	95088_178-1_K1_FC_031_11,5k TEM	19k	AX	NRT	☐	25	1208,777	48,351	0,178	View Samples
34	178	FC	95088_178-1_K1_FC_031_11,5k TEM	19k	AX	NRT	☐	36	2074,789	57,633	0,220	View Samples
34	178	FC	95088_178-1_K1_FC_031_11,5k TEM	19k	AX	NRT	☐	36	2074,789	57,633	0,220	View Samples
35	178	FC	95088_178-1_K1_FC_032_11,5k TEM	19k	AX	MS	☐	2	215,366	107,683	0,085	View Samples
35	178	FC	95088_178-1_K1_FC_032_11,5k TEM	19k	OD	ODP	☐	3	122,849	40,950	0,037	View Samples
36	178	FC	95088_178-1_K1_FC_033_11,5k TEM	19k	DN	DS	☐	0	0	0	0	View Samples
36	178	FC	95088_178-1_K1_FC_033_11,5k TEM	19k	UND	MC	☐	2	51,566	25,783	0,015	View Samples
36	178	FC	95088_178-1_K1_FC_033_11,5k TEM	19k	OD	ODP	☑	27	1166,311	43,197	0,314	View Samples
37	178	FC	95088_178-1_K1_FC_034_11,5k TEM	19k	OD	ODP	☐	25	1442,343	57,694	0,203	View Samples

Figure 11: DATEM: EFTEM Cells Consistency Check
Data list views within DATEM were used quickly skim through data (such as image ID, brain identification, image file name, magnification, categorization of cell type and structure, particle analysis) in order to detect missing or erroneous datasets.

4.6 Image Analysis

To perform analysis on images, all elastic images (including colored structures) and iron M map images were batch-converted to a separate analysis folder. Prior to particle analysis of EFTEM, the elemental maps were also batch-converted with the settings listed in ***Table 8***. This resulted in an inverted, binary image with additional gamma correction to reduce noisy and scarcely stained artefacts.

Table 8: Settings for Irfan View Batch-Conversion

Irfan View Settings	
✓	**2 Colors (black/white) (1BPP)**
✓	**Use Floyd Steinberg Dithering**
✓	**Negative**
✓	**Gamma Correction 1.20**

For the image analysis, the java based NIH open source application ImageJ was used in the Fiji distribution version (http://imagej.net/Fiji/Downloads). A macro was recorded for automation to adjust a standardized threshold and convert the *.tiff image to a binary mask for subsequent particle analysis.

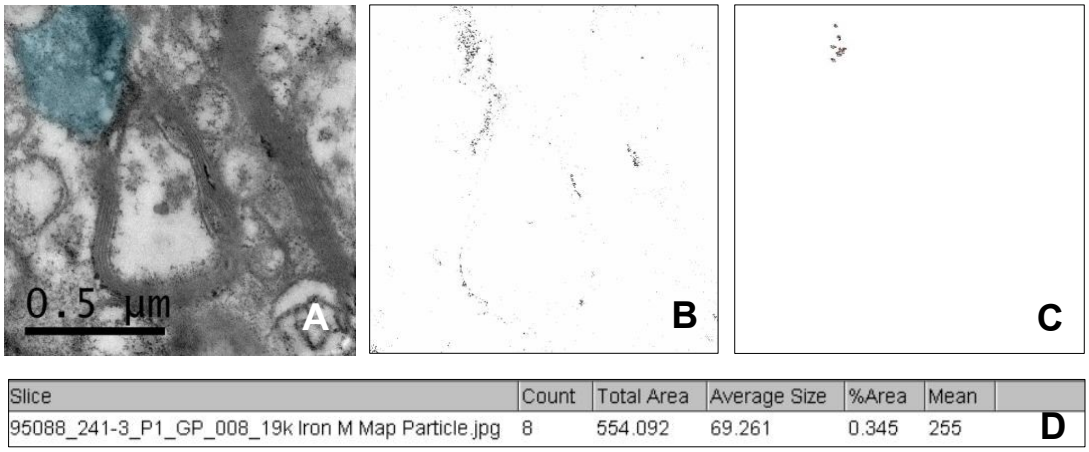

Slice	Count	Total Area	Average Size	%Area	Mean
95088_241-3_P1_GP_008_19k Iron M Map Particle.jpg	8	554.092	69.261	0.345	255

D

Figure 12: Particle Analysis of ROI
(**A**): Oligodendrocyte process colored in Adobe Photoshop CS3 on the elastic image for categorization within DATEM. (**B**): EFTEM iron map distribution after applying the macro filters prior to particle analysis by elemental map batch conversion in Irfan View. (**C**): After boundaries of colored area of elastic were manually re-drawn and selected within ImageJ, particle counts including bare outlines of the corresponding ROI were created. (**D**): Summary of particle analysis performed on the colored ROI after selection.

While various publications diverge on the size of ferritin cores, research revealed a core size of around 8 nm in ferritin solutions (81), and electron microscopy research indicated single crystal formation with 6-7 nm across (82). Other research implicates a 12 nm protein structure with an 8 nm central iron storage cavity (83). Data published by Quintana et al. (18) indicated that ferritin cores of human brain samples appear much smaller on transmission electron microscopes than previous publications indicate. By adjusting scale within Fiji and measuring ferritin cores in images published in the paper (18), ferritin cores were only 20-22 nm² in area. Given the fact that ferritin cores appear almost circular, the ferritin cores in Quintana's publication therefore have a radius of approximately 2,5 nm, when solving the equation of the area of a circle for the measured radius. Therefore, for the particle analysis of the obtained sample images for the feasibility study, all particles below 20 nm² were excluded in Fiji (***Figure 13***).

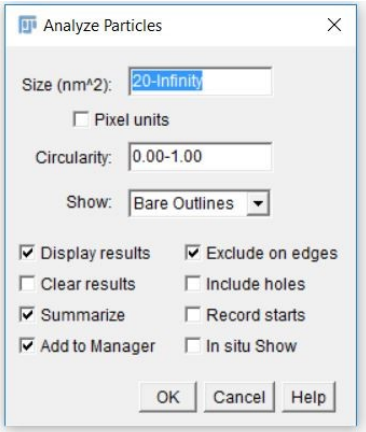

Figure 13: Particle Analysis Settings within Fiji
For size settings, only particles equal to or larger than 20 nm² were included in the analysis.

4.7 Statistical Methods

Statistical analysis was performed using the software SPSS 23.0 (SPSS Inc., Chicago, Illinois, USA), provided by the Medical University of Graz via Citrix Remote Desktop Server. The small sample size of brains (a total of 3) available at the time of sample image acquisition for the present diploma thesis did not allow inferential statistics to be used. Therefore, only descriptive statistics were applied for the sample images dataset. However, thoughts on an inferential approach for the expanded future study are given in ***section 6.1***.

For the descriptive statistics, the final dataset was exported as *.xls spreadsheet from DATEM. Data were imported into SPSS and variables were re-defined as present in DATEM. Main endpoint was the metrical variable *%area* according to the categorical variables such as “brainarea” (constituting regions of the brain), “celltypes” and “cellstructure” (structure underlying the cell type). Analysis involved frequencies of observed data, including percent and cumulative percent, and descriptive statistics constituted *N*, Minimum, Maximum, Mean and Standard Deviation (*SD*). For visualization of the results, bar graphs and histograms were generated.

5 Results

Sample image/particle analysis techniques as well as the utilization of DATEM as a database for sorting of images were explained within the methods section. The remaining objectives of this feasibility study will be treated within the results section as follows:

I. To determine whether EFTEM and EDX are suitable for the detection of iron in biological samples, both applied methods will be compared in the same field of view within the same specimen.

II. It will be specified which EFTEM element edge is useful in obtaining iron EFTEM images from resin embedded, osmium fixed specimens.

III. Categorization of cell structures, DATEM uploads, image analysis of specific structures of datasets obtained in the feasibility study will be shown, including descriptive statistics of the sample images analysis.

Within the scope of the feasibility study, a total of 17 tissue samples were observed with EFTEM. ***Table 9*** summarizes the number of different EFTEM images obtained according to the available brains and underlying samples.

Table 9: EFTEM Sets, Specimens and Brains per ROI available for analysis

ROI	EFTEM Sets	# Specimens	# Brains
CC	36	1	1*
FC	47	2	1*
FWM	46	2	1*
GP	134	4	3
PT	149	8	2
TOTAL:	**412**		

**Results of ROIs where only a sample size of 1 is given may not be seen as a common predictor.*

5.1 Comparison of EFTEM and EDX

While EFTEM was used to create elemental maps at mainly iron M edge, EDX spectra were also obtained of areas where EFTEM at various time points had registered the presence of iron in order to verify these findings. It is pivotal to combine EFTEM with a spectroscopic analytical electron microscopy method such as EDX or electron energy loss spectroscopy to avoid false positive signals.

Initially the iron M edge was used for EFTEM imaging, and EDX spectroscopy was used for validating the results of EFTEM imaging. For this, structures that were positive for iron in EFTEM mode were identified in STEM mode of the same area of the same specimen. An EDX spectrum within a rectangle surrounding this structure was obtained. As a control, another EDX spectrum was used in a nearby area that was unlikely to contain iron (i.e. axoplasm with no visible structures). ***Figure 14*** and ***Figure 15*** elaborate two example STEM images with the corresponding EFTEM analysis.

This validation was conclusive in most parts, as integrated intensity values for iron content were measured at the areas where corresponding staining in EFTEM was visible. However, the values of integrated intensities did not match the intensity of the staining observed in the EFTEM image. In ***Figure 14***, the elemental map of the suspected oligodendrocitic iron inclusion (**D**) shows an intense staining, whereas spectrum analysis shows a Fe-K associated integrated intensity with a low value of *6,798*. ***Figure 15*** shows diffuse, but clearly recognizable staining in the elemental map of lipofuscin granules (**D**), whereas again the integrated intensity of spectrum analysis reveals a peak of Fe-L with only *5,184*. Nevertheless, both control areas with no iron content also showed no intensities in the EDX spectrum analysis.

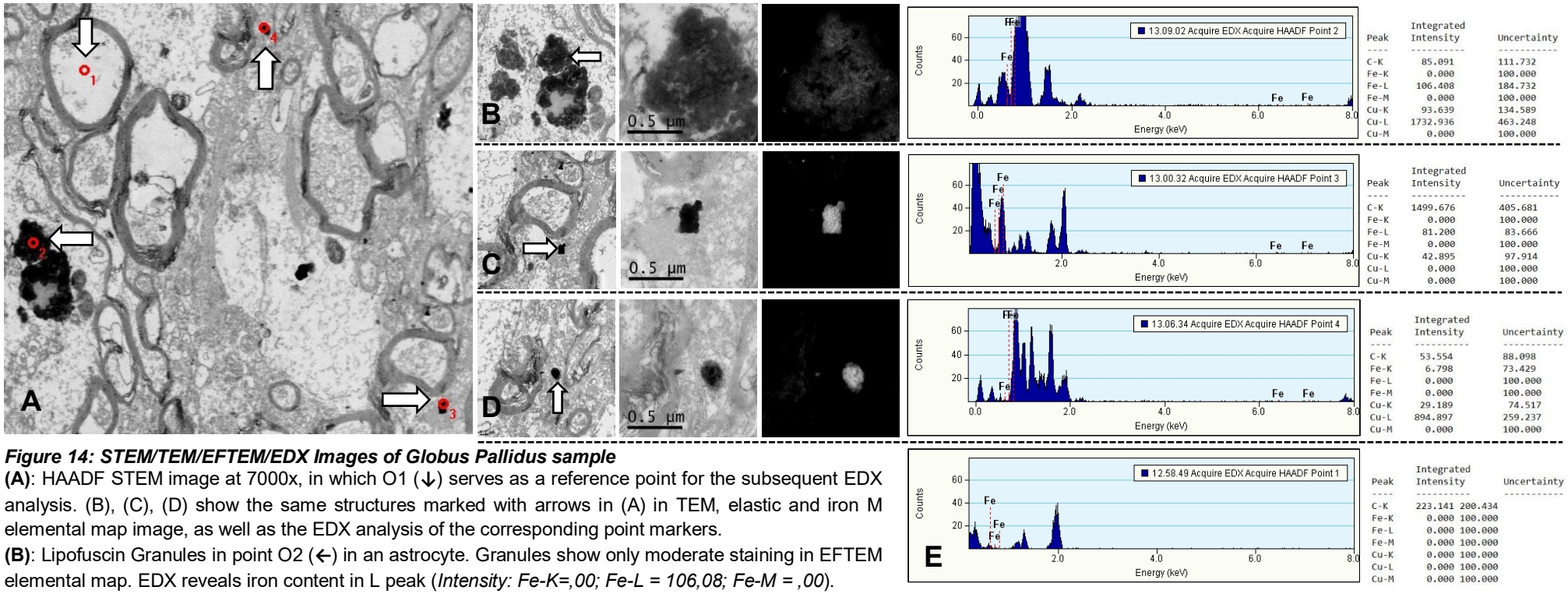

Figure 14: STEM/TEM/EFTEM/EDX Images of Globus Pallidus sample

(A): HAADF STEM image at 7000x, in which O1 (↓) serves as a reference point for the subsequent EDX analysis. (B), (C), (D) show the same structures marked with arrows in (A) in TEM, elastic and iron M elemental map image, as well as the EDX analysis of the corresponding point markers.

(B): Lipofuscin Granules in point O2 (←) in an astrocyte. Granules show only moderate staining in EFTEM elemental map. EDX reveals iron content in L peak (*Intensity: Fe-K=,00; Fe-L = 106,08; Fe-M = ,00*).

(C): A suspected contamination (i.e. dust particle) on an oligodendrocitic process (→) with strong staining in EFTEM elemental map. Oligodendrocitic process reveals iron content in L peak (*Intensity: Fe-K=,00; Fe-L = 81,200; Fe-M = ,00*).

(D): Another suspected contamination in an oligodendrocitic process (↑) originating from the same oligodendrocyte, also showing strong staining for iron content. EDX particle analysis detects little iron content in the oligodendrocitic process in point 4 (↑) at Fe-K peak (*Intensity: Fe-K=6,798; Fe-L = ,00; Fe-M = ,00*).

(E): EDX analysis of the reference point O1 showed no spectrum of Fe (*Intensity: Fe-K=,00; Fe-L = ,00; Fe-M = ,00*).

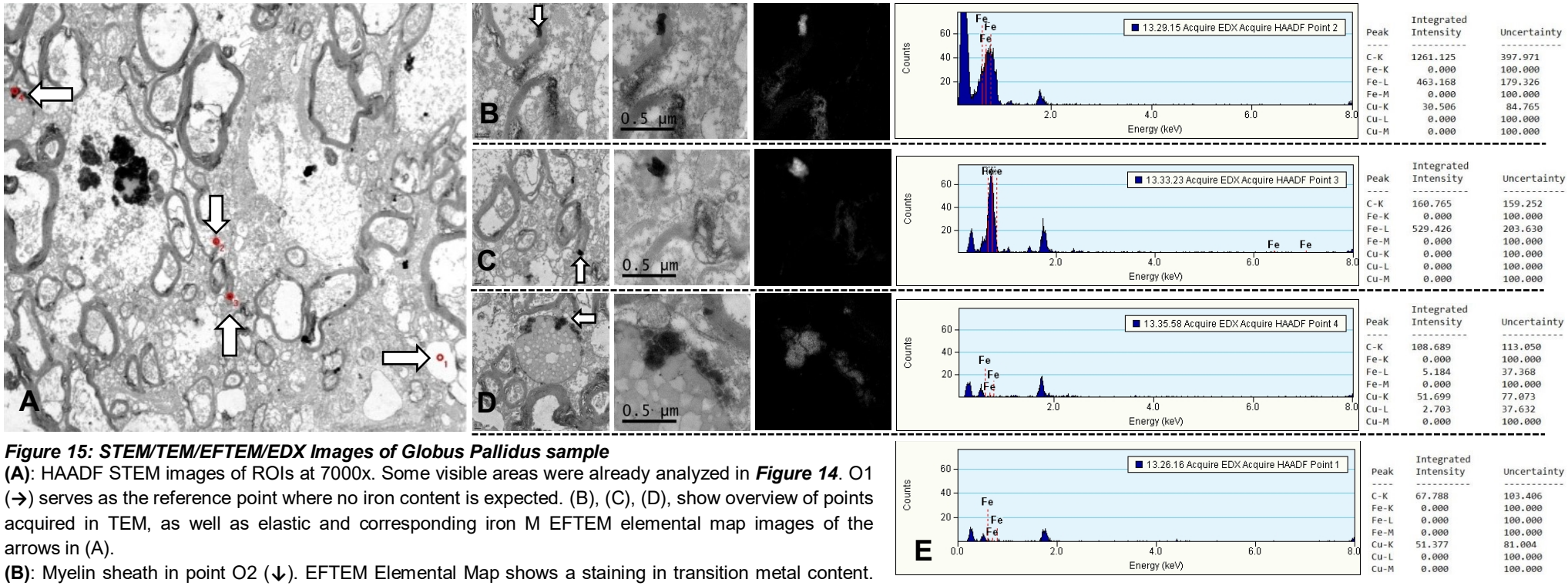

Figure 15: STEM/TEM/EFTEM/EDX Images of Globus Pallidus sample

(A): HAADF STEM images of ROIs at 7000x. Some visible areas were already analyzed in ***Figure 14***. O1 (→) serves as the reference point where no iron content is expected. (B), (C), (D), show overview of points acquired in TEM, as well as elastic and corresponding iron M EFTEM elemental map images of the arrows in (A).

(B): Myelin sheath in point O2 (↓). EFTEM Elemental Map shows a staining in transition metal content. EDX of the point on myelin sheath (↓) shows content in iron L peak (*Intensity: Fe-K=,00; Fe-L = 463,168; Fe-M = ,00*).

(C): Transition metal deposits are visible in an oligodendrocitic process (↑). In EFTEM, the inclusion in axoplasm is clearly stainable. EDX analysis reveals high iron L peaks (*Intensity: Fe-K=,00; Fe-L = 529,426; Fe-M = ,00*).

(D): Inclusion in a huge lipid droplet (←) shows diffuse staining for transition metal content in EFTEM elemental map. Little iron content is detected within the astrocytic lipofuscin granule in point 4 (←) at Fe-L peak of EDX (*Intensity: Fe-K=,00; Fe-L = 5,184 Fe-M = ,00*),

(E): EDX analysis of hole serving as reference point O1 (→) showed no Fe peaks in EDX analysis (*Intensity: Fe-K=,00; Fe-L = ,00; Fe-M = ,00*).

5.2 Iron M Peak Validation

As elaborated in the last chapter, EDX showed replicable, but still at some points inconclusive results given the fact that strong staining in the iron M map did not correlate with an expected high Fe outcome in EDX. Above all, a closer look at the EFTEM iron M peak used for sample images was indispensable. Comparison of iron M and iron L maps in EFTEM showed that stronger staining could be achieved using iron M peak. However, it was described in literature (84) that EFTEM iron M peaks potentially might overlap with osmium peaks. As elaborated in the methods section on p. 17, fixation of specimens was conducted with osmium tetroxide. Therefore, both available iron peaks (*L,M*) were compared to the osmium O peak elemental maps of 4 areas within a specimen. ***Figure 16*** shows the comparison between the three edges and reveals the distinct differences in staining of granules and surrounding structures.

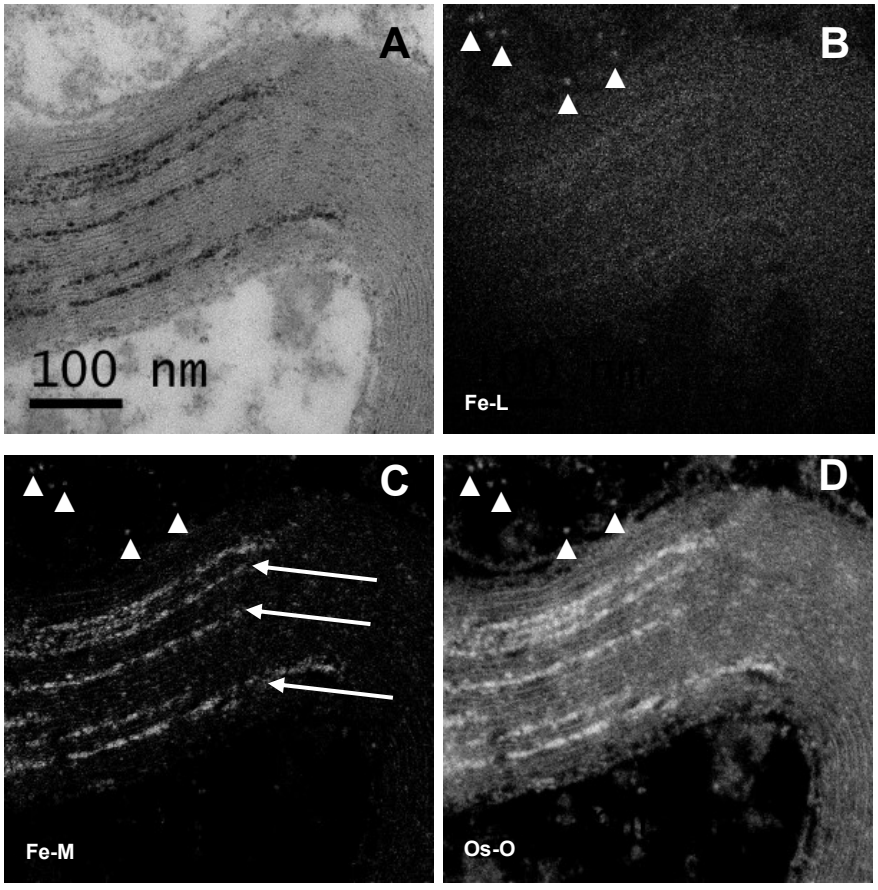

Figure 16: Comparison of Iron L, Iron M and Osmium O Elemental Maps
(**A**): Unfiltered elastic image taken from a myelin sheath in the putamen at 100 k magnification. (**B**) Iron L map of image shows only diffuse staining with some few potential ferritin cores (▲) outside of the sheath. (**C**) Iron M map also shows the proposed iron content seen in the iron L map (▲), but contains far more stained areas within the sheath (←). (**D**) Osmium O map contains among others all visible areas from Iron M map, suspecting an overlap between iron and osmium content which accumulated within the sheath.

5.2.1 Overlapping Peaks in Elemental Maps

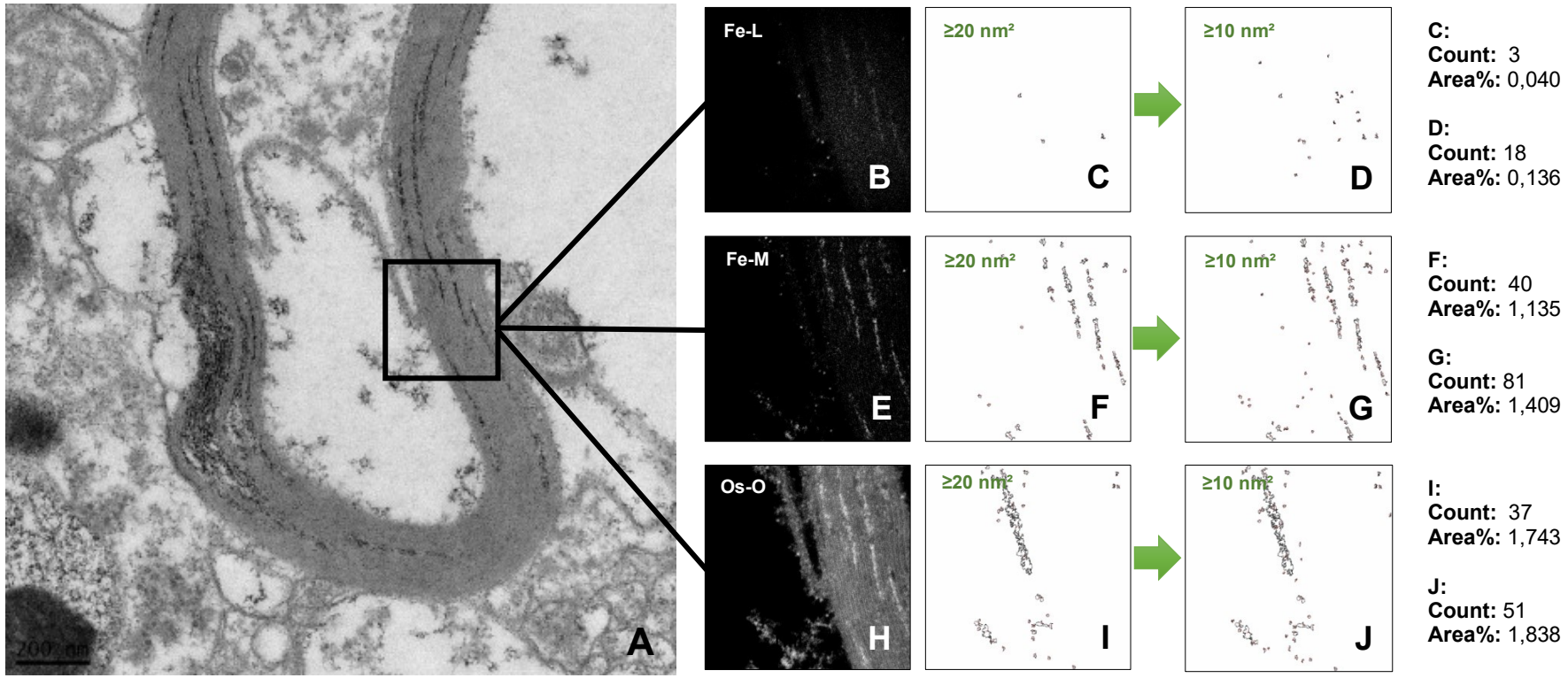

Figure 17: Overlapping Elemental Peaks in a Myelin Sheath

(**A**): Section of a myelin sheath in the putamen, taken at a magnification of 11,5k. (**B**): Iron L map of the myelin sheath section at 100k magnification. Standardized analysis with particles ≥20 nm² are shown in (**C**). (**D**) shows another analysis for particle sizes from 10 nm² and above. A proposed ferritin core in the ≥10 nm² analysis (◄) reaches an area of *14,581* nm², with an approximate diameter of only *4,31* nm. (**E**): Iron M map of myelin sheath again shows distinct staining within the myelin sheath. Particle analysis with sizes ≥20 nm² (**F**) and ≥10 nm² (**G**) proves the assumption. Due to the immense staining in the Osmium O map (**H**), most of the stained areas within myelin sheath are ignored in the analysis (**I**), (**J**). Nevertheless it is clear that staining increases from Iron L to Iron M, whereas Osmium O map contains all structures also visible in Iron M map.

5.2.2 Overlapping Peaks in Elemental Maps

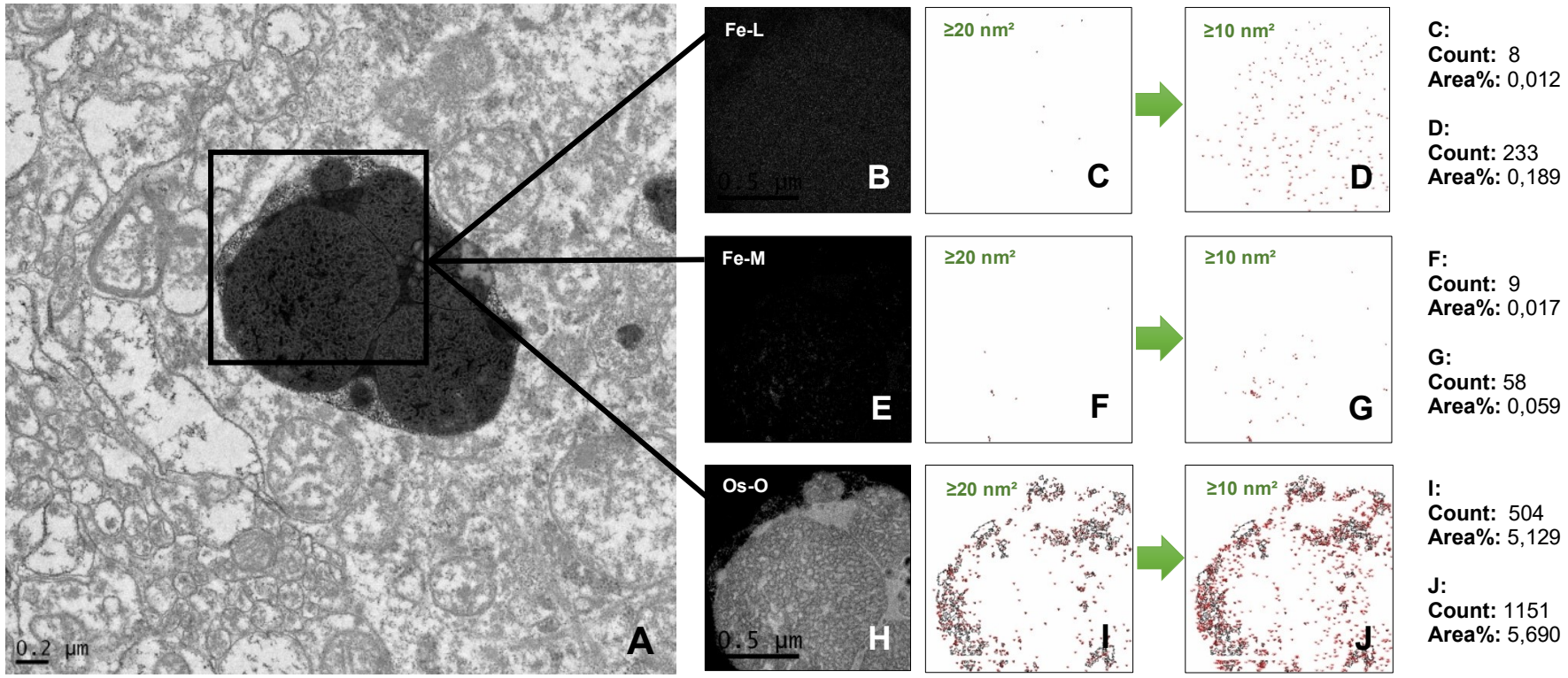

Figure 18: Overlapping Elemental Maps in a Cytoplasmatic Inclusion
(**A**) TEM image of a cytoplasmatic inclusion, putatively from a telolysosome within a putamen section at 5k. (**B**): Iron L map taken at 19 k shows diffuse staining, Particle analysis at sizes ≥20 nm² (**C**) reveal 8 counts (% area of *,012*), which cannot be reproduced clearly when looking at the elemental map in plain view. Analysis of particles ≥10 nm² (**D**) even lead to a particle count of 233 with a % area of *,189*. Iron M map (**E**) show more distinct staining compared to iron L peak. Stained structures in the analysis (**F**), (**G**) do not match the iron L peak. Nevertheless, Osmium O peak (**H**) shows absolute staining of the whole section with no replicable corresponding particle analysis (**I**), (**J**).

When directly comparing the % area outcomes of the myelin sheath in ***Figure 17***, differences in the particles automatically detected can be seen between the iron M, iron L and the osmium O maps (***Table 10***). Analysis of particles ≥20 nm² showed a 28-fold increase from L to M-map and a 10-fold increase for particles ≥10 nm². The largest differences can be seen in % area between iron L and osmium O analysis (43-fold increased % area for ≥20nm² and 13-fold increase for particles ≥10nm²). On the other hand, there is only a minor difference between osmium O and iron M map % area with a factor of 1,5 fold for 20nm² and 1,3 fold increase for 10nm² analysis.

Table 10: Difference of Osmium and Iron L Peaks % Area

	Iron L %Area	Iron M %Area	Osmium O % Area	Factor M/L	Factor O/L	Factor O/M
	≥20nm²					
Myelin Sheath	0,04	1,135	1,743	**28,375**	**43,575**	**1,535**
	≥10nm²					
	0,136	1,409	1,838	**10,360**	**13,514**	**1,304**

It can be concluded that osmium presents itself with an EELS spectrum edge close to the iron $M_{2,3}$ peak, thereby causing potential problems with the detectability of iron at the M edge. As shown in the comparison of elemental maps in ***Figure 17***, reliable outcomes in the detection of iron can therefore only be derived by using an iron L elemental map. Due to this fact, any putative iron content in sample images taken for the establishment of methodology has to be regarded as *transition metal content*, as no clear differentiation can be drawn between suspected iron and interference with osmium-tetroxide as fixative. For the main study, it is recommended to use the iron L map in order to rule out any overlaps with osmium-tetroxide as a fixative. Therefore, the iron L peak is essential to avoid overlaps with osmium peaks in EFTEM. Nevertheless, a large dataset of sample images had already been taken at the iron M peak, and these proved to be valuable for the purpose of this feasibility study for the following reasons: Firstly, they proved to be brighter and thus more reliable at lower magnifications than images taken at the iron L-peak, saving time during image aquisition and rendering them useful for further categorization of individual cells and structures. Additionally, further image acquisition with L peak would go beyond the scope of the present diploma thesis.

5.3 EFTEM Analysis

Altogether, a total of 412 sample EFTEM images were acquired within the scope of this diploma thesis, of which 1061 substructures were colored and extracted for possible categorizations within DATEM. After review by the advisor and follow-ups on categorization of structures, 206 substructure images matched exclusion criteria (***Table 12***) and 9 were reviewed as being unlikely and were therefore dismissed from statistical analysis. The remaining data were exported and consisted of 846 rows for subsequent statistical evaluation. ***Table 11*** shows the frequencies of the categorized cell types distributed within the 846 dataset rows.

Table 11: Frequencies of Cell Types per Brain Area in Sample Images Dataset

		Frequency	Percent
Valid	astrocyte	100	11,8
	axon	411	48,6
	dendrite	188	22,2
	oligodendrocyte	141	16,7
	undefinable	6	,7
	Total	**846**	**100,0**

Table 12: Reasons and Frequencies of Images Excluded from Analysis

Exclusion Criterion	# of images
Duplicate Structure	14
EFTEM not replicable	18
Erroneous coloring	28
Non-standardized Magnification	111
Type/Structure undefinable	31
Weak preservation	4
	206

5.3.1 Parameters for Analysis

First a frequency table will be produced to show the amount of datasets obtained per variable (i.e. brain/cell type/structure) and their corresponding percentage for descriptive statistics. For reasons of clarity, additional frequency parameters, such as cumulative percent, are not displayed in the statistical analysis presented for the sample images. For the statistical evaluation of particle analysis in Fiji, the parameter “% area” of the ROI, respectively of the individual cells and structures highlighted, proved to be the most reliable source of quantification. Percentage

area refers to the percentage of the area (given in nm²) of the detected transition metal particles in the specifically highlighted and categorized region of interest in relation to the total area of the marked region of interest in an EFTEM image. The metrical variable “particle count”, which is also determined within the particle analysis, does not give any relationship as to size or quantity of detected particles within the specified area of the sample and is therefore not appropriate for objective analysis. ***Table 13*** shows an example of how descriptive statistics of % area of transition metal content can be presented according to the previous categorizations of brain area, cell type and cell structure.

Table 13: Example of Descriptive Statistics Datasets of % Area

celltypes	cellstructure	brainarea		N	Min.	Max.	Mean	SD
X	X	X	**%Area**	**X**	**X**	**X**	**X**	**X**
			Valid N (listwise)					

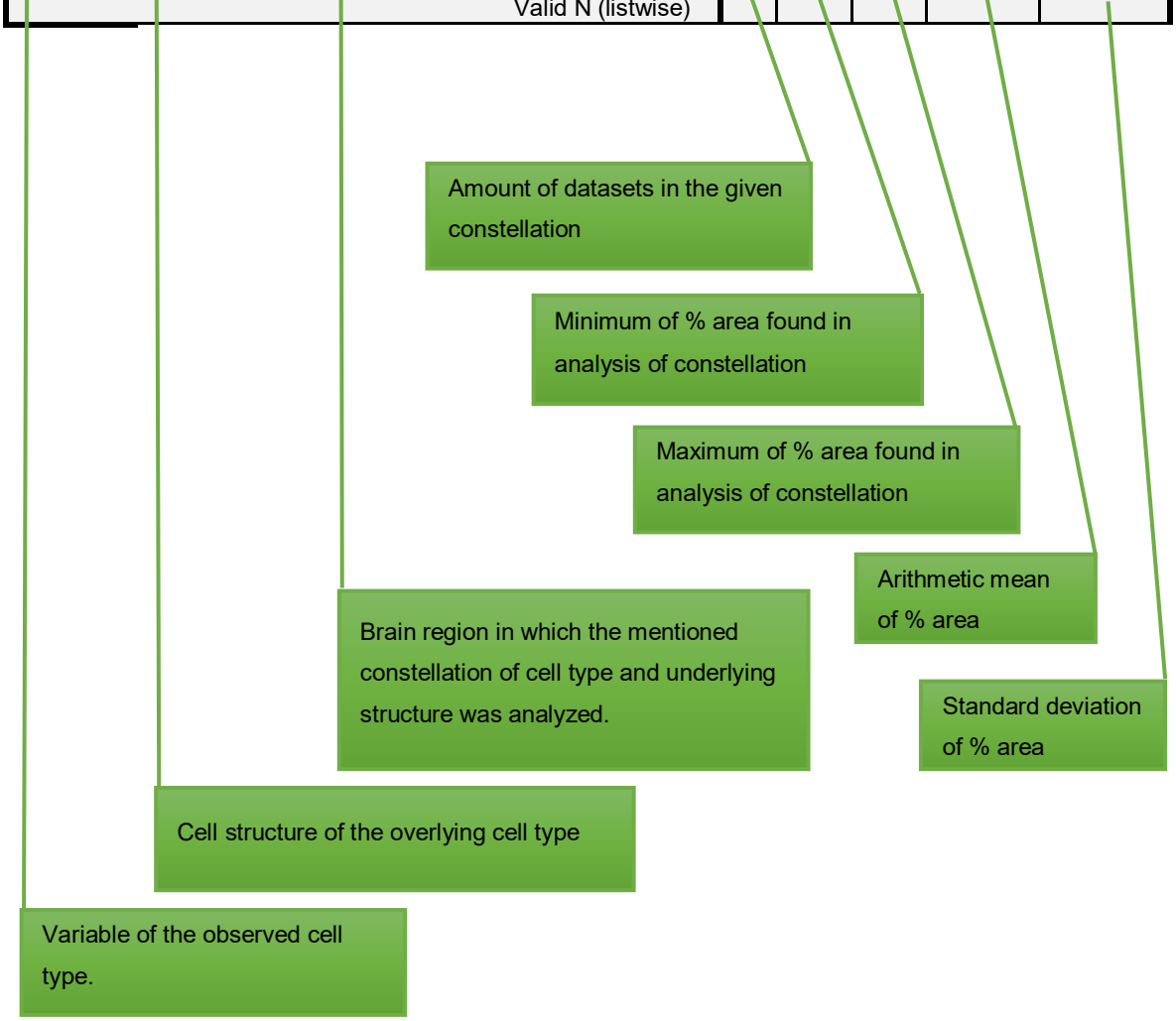

5.3.2 Axons

A total of 411 axons were identified on micrographs within the research (see ***Table 14***), of which the majority were additionally distinguished in their structure between whole neurite (*n=144*), and the substructures axoplasm (*n=57*), myelin sheath (*n=138*), and nerve terminal (*n=53*). The remaining axonal structures contained mitochondria (*n=18*), glycogen (*n=1*) and will be discussed in separate subchapters of the results section.

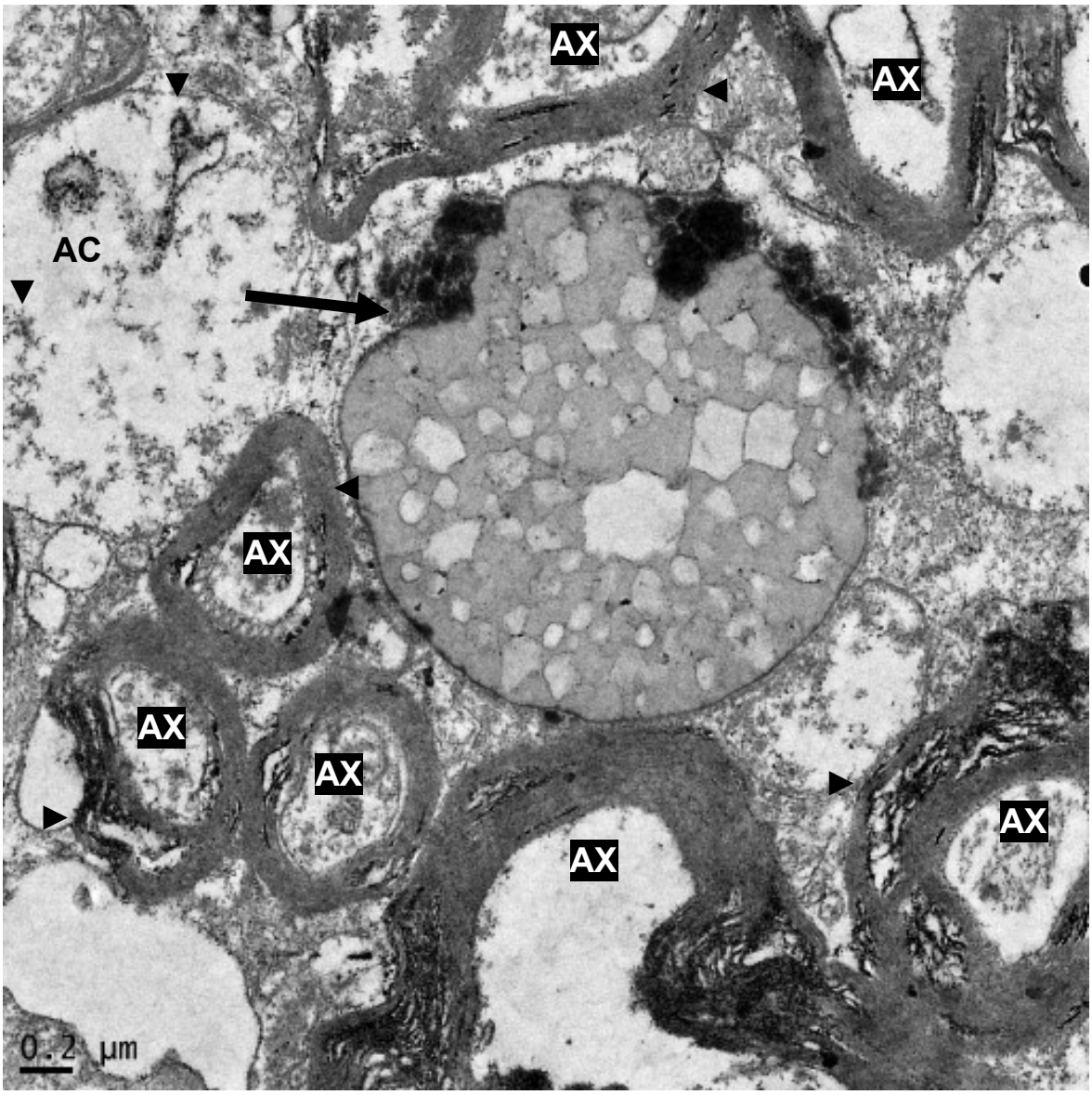

Figure 19: Overview of Axons in the Globus Pallidus
TEM image at 5k of multiple axons surrounded by an astrocyte (AC) in the globus pallidus. While some myelin sheaths are well preserved (◄), others shows clear signs of shearing defects (►). The astrocyte presents itself characteristically with glycogen particles (▼) and a heterogenous cytoplasmatic inclusion (→) with lipofuscine granules (dark spots). Enclosed lipid droplets are distinguishable as light spots.

The reason for the differentiation between whole neurite and the myelin sheath and axoplasm was to find potential differences in transition metal content between the underlying substructures (i.e. myelin sheath and axoplasm). The generalized categorization of “whole neurite” was only used when the whole axon was visible in the area of interest at the standardized magnification in EFTEM.

Table 14: Axon Frequencies per Brain Area

		Frequency	Percent
Valid	corpus callosum	44	10,7
	frontal cortex	31	7,5
	frontal white matter	43	10,5
	globus pallidus	192	46,7
	putamen	101	24,6
	Total	411	100,0

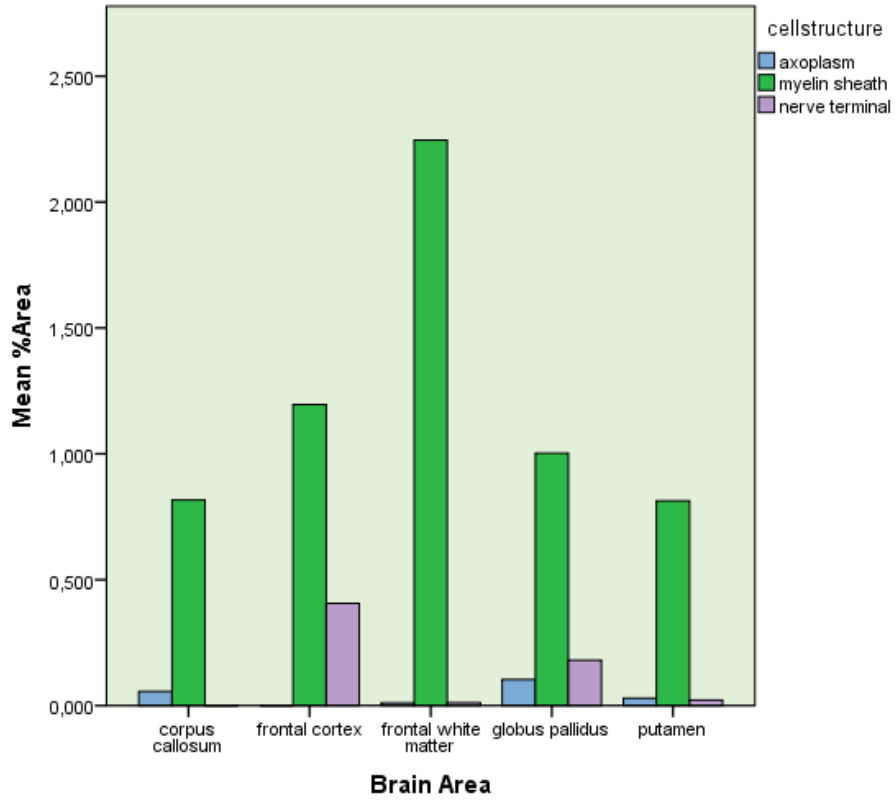

Figure 20: Bar Graph Comparison of Mean % Areas of Axonal Structures per Brain Area
All three main axonal substructures (*axoplasm = blue; myelin sheath = green*; *nerve terminal = purple*) were compared by their mean percentage area within the bar graph. Myelin sheath % areas by far outnumbered the remaining structures, whereas highest percentage areas could be found within the frontal white matter samples. The axoplasm contained the least transition metal content detected in axonal substructures.

Table 15: % Area of Axonal Substructures

Descriptive Statistics

celltypes	brainarea	cellstructure		N	Min.	Max.	Mean	SD
axon	corpus callosum	axoplasm	**%Area**	**8**	**,000**	**,311**	**,05612**	**,108836**
			Valid N (listwise)	8				
		myelin sheath	**%Area**	**19**	**,015**	**5,354**	**,81658**	**1,215195**
			Valid N (listwise)	19				
		nerve terminal	**%Area**	**1**	**,000**	**,000**	**,00000**	**.**
			Valid N (listwise)	1				
		whole neurite	**%Area**	**16**	**,046**	**,754**	**,21506**	**,198577**
			Valid N (listwise)	16				
	frontal cortex	axoplasm	**%Area**	**3**	**,000**	**,000**	**,00000**	**,000000**
			Valid N (listwise)	3				
		myelin sheath	**%Area**	**6**	**,085**	**3,204**	**1,19600**	**1,469176**
			Valid N (listwise)	6				
		nerve terminal	**%Area**	**8**	**,000**	**1,966**	**,40613**	**,643406**
			Valid N (listwise)	8				
		whole neurite	**%Area**	**12**	**,098**	**,735**	**,34217**	**,194279**
			Valid N (listwise)	12				
	frontal white matter	axoplasm	**%Area**	**3**	**,000**	**,033**	**,01100**	**,019053**
			Valid N (listwise)	3				
		myelin sheath	**%Area**	**20**	**,073**	**5,937**	**2,24595**	**2,025316**
			Valid N (listwise)	20				
		nerve terminal	**%Area**	**2**	**,000**	**,023**	**,01150**	**,016263**
			Valid N (listwise)	2				
		whole neurite	**%Area**	**16**	**,000**	**2,406**	**,88356**	**,769493**
			Valid N (listwise)	16				
	globus pallidus	axoplasm	**%Area**	**29**	**,000**	**1,666**	**,10341**	**,330540**
			Valid N (listwise)	29				
		myelin sheath	**%Area**	**67**	**,000**	**5,455**	**1,00263**	**1,306249**
			Valid N (listwise)	67				
		nerve terminal	**%Area**	**25**	**,000**	**1,625**	**,18076**	**,387101**
			Valid N (listwise)	25				
		whole neurite	**%Area**	**59**	**,000**	**3,860**	**,54564**	**,731924**
			Valid N (listwise)	59				
	putamen	axoplasm	**%Area**	**13**	**,000**	**,213**	**,02969**	**,062084**
			Valid N (listwise)	13				
		myelin sheath	**%Area**	**26**	**,000**	**2,226**	**,81323**	**,713948**
			Valid N (listwise)	26				
		nerve terminal	**%Area**	**16**	**,000**	**,198**	**,02231**	**,049562**
			Valid N (listwise)	16				
		whole neurite	**%Area**	**41**	**,000**	**1,973**	**,37171**	**,464061**
			Valid N (listwise)	41				

5.3.2.1 Whole Neurite

144 axons within DATEM sample images were categorized as “whole neurites”, where myelin sheath, axoplasm and other structures enclosed in the axon were all included within the particle analysis. Their frequencies according to the observed brain area are summarized in ***Table 16***.

Table 16: Whole Neurite Frequencies per Brain Area

		Frequency	Percent
Valid	corpus callosum	16	11,1
	frontal cortex	12	8,3
	frontal white matter	16	11,1
	globus pallidus	59	41,0
	putamen	41	28,5
	Total	144	100,0

Table 17: % Area in Whole Neurites per Brain Area

Descriptive Statistics

celltypes	cellstructure	brainarea		N	Min.	Max.	Mean	SD
axon	whole neurite	corpus callosum	**%Area**	**16**	**,046**	**,754**	**,21506**	**,198577**
			Valid N (listwise)	16				
		frontal cortex	**%Area**	**12**	**,098**	**,735**	**,34217**	**,194279**
			Valid N (listwise)	12				
		frontal white matter	**%Area**	**16**	**,000**	**2,406**	**,88356**	**,769493**
			Valid N (listwise)	16				
		globus pallidus	**%Area**	**59**	**,000**	**3,860**	**,54564**	**,731924**
			Valid N (listwise)	59				
		putamen	**%Area**	**41**	**,000**	**1,973**	**,37171**	**,464061**
			Valid N (listwise)	41				

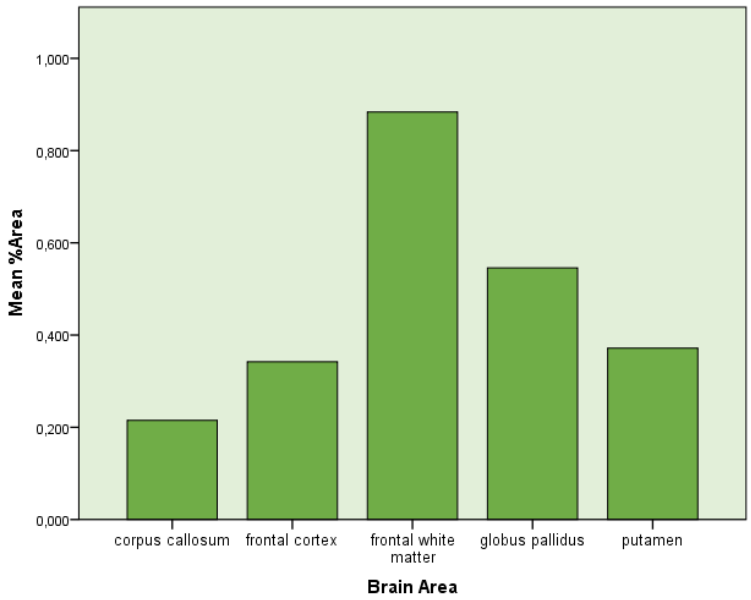

Figure 21: Bar Graph of Mean % Area of Whole Neurites per Brain Area
The frontal white matter showed the highest % area for transition metal content within whole neurites (*N=144*; *M=,10341; SD=,769493*).

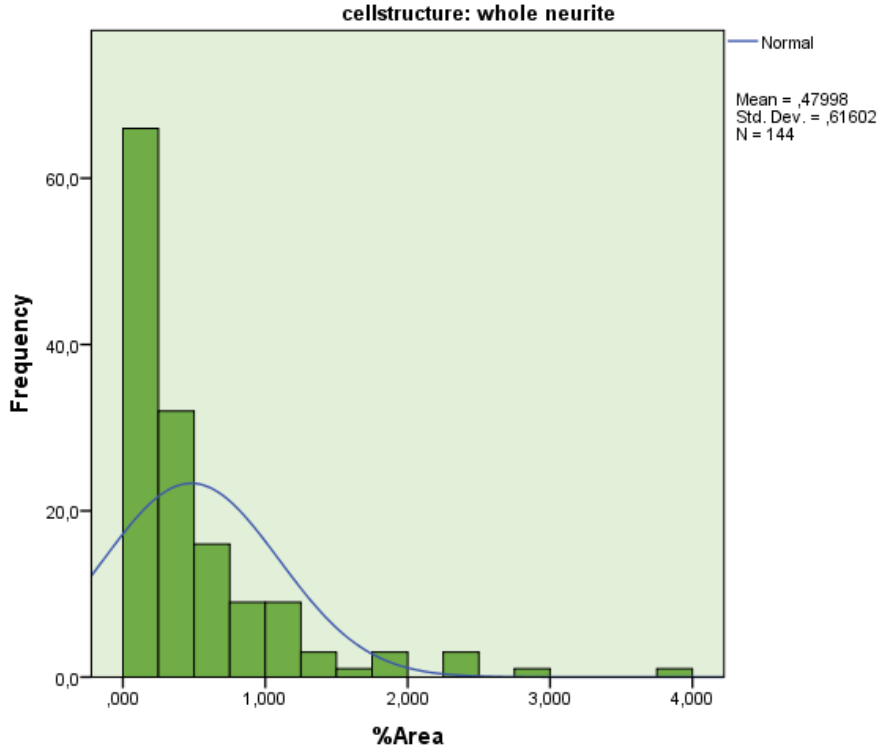

Figure 22: Histogram of % Area Frequencies of Whole Neurites

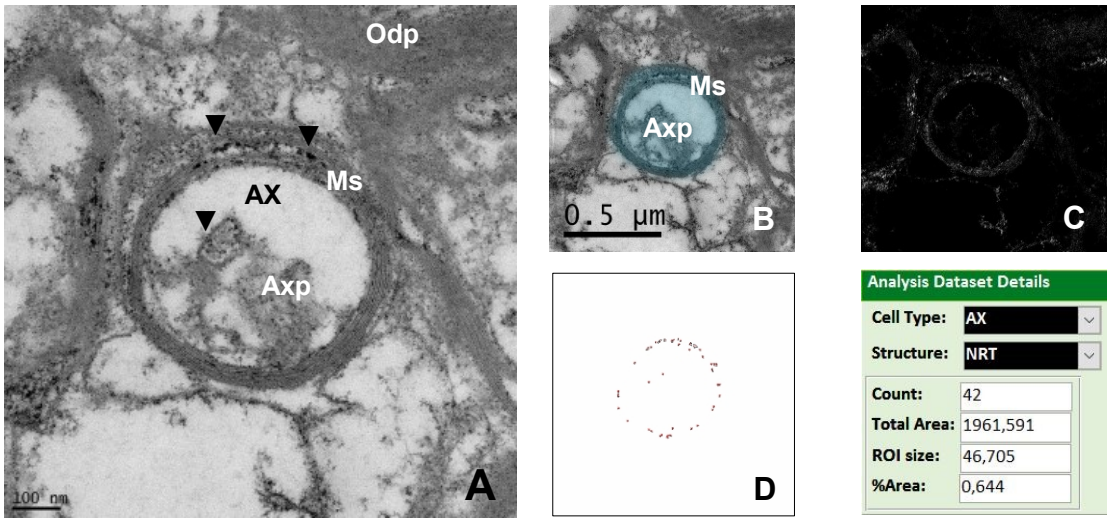

Figure 23: Whole Neurite in Putamen
(**A**): TEM image of a transversally cut axon (AX) taken at 14,5 k. Several diffusely distributed transition metal content can be suspected in the axonal structures (▼). Above a suspected oligodendrocitic process (Odp) can be observed. (**B**): Both myelin sheath (Ms) and axoplasm (Axp) are included in the colored area of the elastic image. (**C**): Iron M elemental map of whole area. (**D**): Inverted elemental mapping shows transition metal content of a % area of *,644* within the axonal structures.

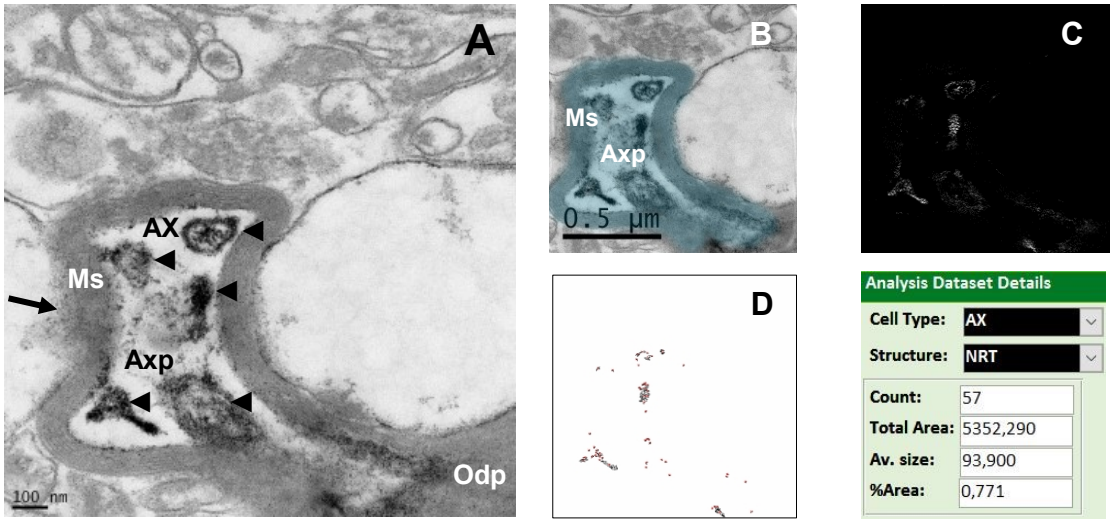

Figure 24: Whole Neurite in Globus Pallidus
(**A**): An axon (AX) taken at 14,5 k in TEM mode with diffuse lysis (→) of myelin sheath (Ms) and unidentifiable cell organelles and inclusions (◀). Several diffusely distributed transition metal content is visible in the axonal structures (◀). An oligodendrocitic process (Odp) forming the myelin sheath is suspected nearby. (**B**): For whole neurite analysis, all structures of the axon are included in the colored elastic image. (**C**): Iron M elemental map of whole area. (**D**): Inverted elemental mapping of the axonal region shows transition metal content of a % area of *,771* in the axoplasmatic inclusions.

5.3.2.2 Myelin Sheaths

Of all 411 observed axons, a total of 138 myelin sheaths as substructures were separately categorized and colored within the DATEM sample datasets. Within the CNS, myelin sheaths wrapped around axons are produced by oligodendrocitic processes enclosing axonal partitions (85). At distinct points, it remains unclear whether study related procedures (sample preparation, fixation) might play a role in the myelin damages visible. The majority of non-degenerated myelin sheaths showed shearing defects, which are described in literature and are basically considered an artifact of sample processing (86). Next to shearing defects, degenerative myelin sheaths were marked within DATEM and their analysis, including comparison to non-degenerative myelin sheaths, is discussed in ***section 5.3.2.2.1)***.

Table 18: Myelin Sheaths Frequencies per Brain Area

	brainarea	Frequency	Percent
Valid	corpus callosum	19	13,8
	frontal cortex	6	4,3
	frontal white matter	20	14,5
	globus pallidus	67	48,6
	putamen	26	18,8
	Total	**138**	**100,0**

Table 19: % Area in Myelin Sheaths per Brain Area

Descriptive Statistics

celltypes	cellstructure	brainarea		N	Min.	Max.	Mean	SD
axon	myelin sheath	corpus callosum	**%Area**	**19**	**,015**	**5,354**	**,81658**	**1,215195**
			Valid N (listwise)	19				
		frontal cortex	**%Area**	**6**	**,085**	**3,204**	**1,19600**	**1,469176**
			Valid N (listwise)	6				
		frontal white matter	**%Area**	**20**	**,073**	**5,937**	**2,24595**	**2,025316**
			Valid N (listwise)	20				
		globus pallidus	**%Area**	**67**	**,000**	**5,455**	**1,00263**	**1,306249**
			Valid N (listwise)	67				
		putamen	**%Area**	**26**	**,000**	**2,226**	**,81323**	**,713948**
			Valid N (listwise)	26				

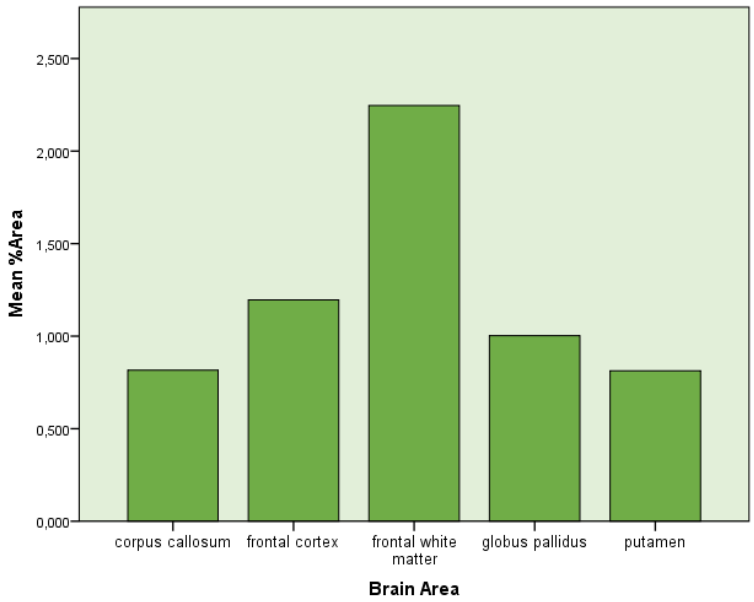

Figure 25: Bar Graph of Mean % Area of Myelin Sheaths per Brain Area
Highest transition metal content can be found within myelin sheaths of the frontal white matter (*N=20*; *M=2,24595*; *SD=2,025316*).

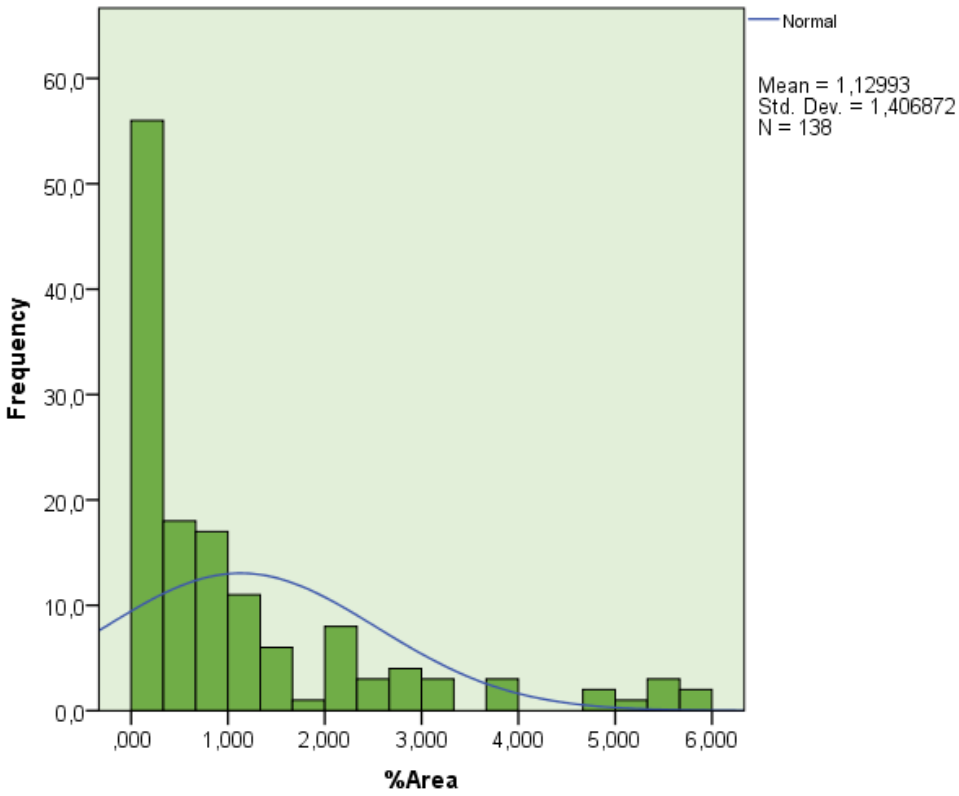

Figure 26: Histogram of % Area Frequencies of Myelin Sheaths
Frequencies of % area of myelin sheaths show a right-skewness in the box-plots. The majority of myelin sheaths showed very little to no transition metal content, whilst highest % areas reach up to a maximum of *5,937*.

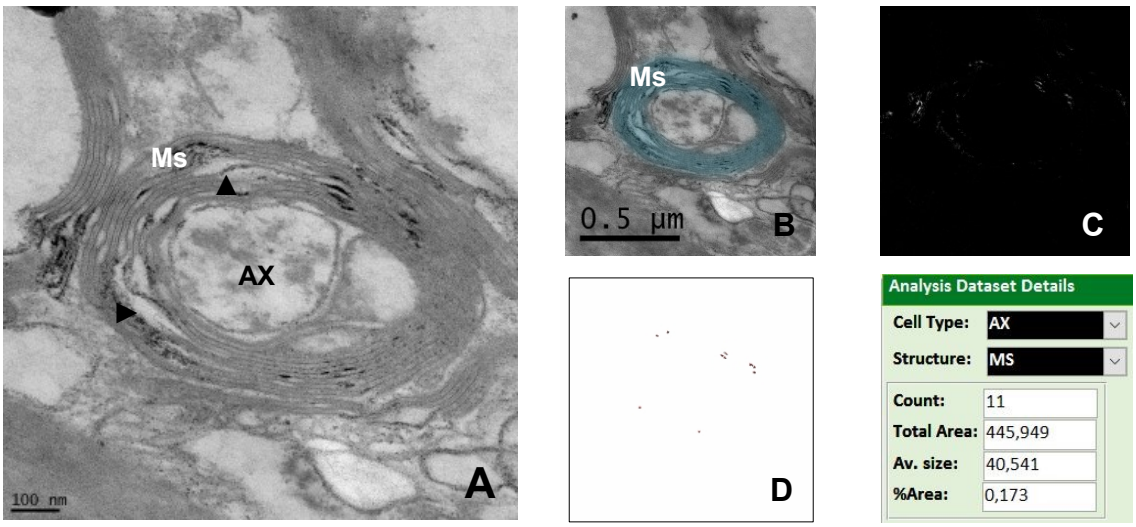

Figure 27: Myelin Sheath in Corpus Callosum
(**A**): TEM image of an axon taken at 19 k magnification. Arrows (▲►) point to different places of shearing defects which are putatively derived from sample processing and do not necessarily reflect senescent neurodegenerative processes (**B**): Elastic image with coloring of the myelin sheath of the center at 19 k. (**C**): Elemental map. (**D**): Particle analysis picture of the colored region of interest, next to it is the particle analysis of the colored area, taken from DATEM after data transmission, and showing a % area of *,173*.

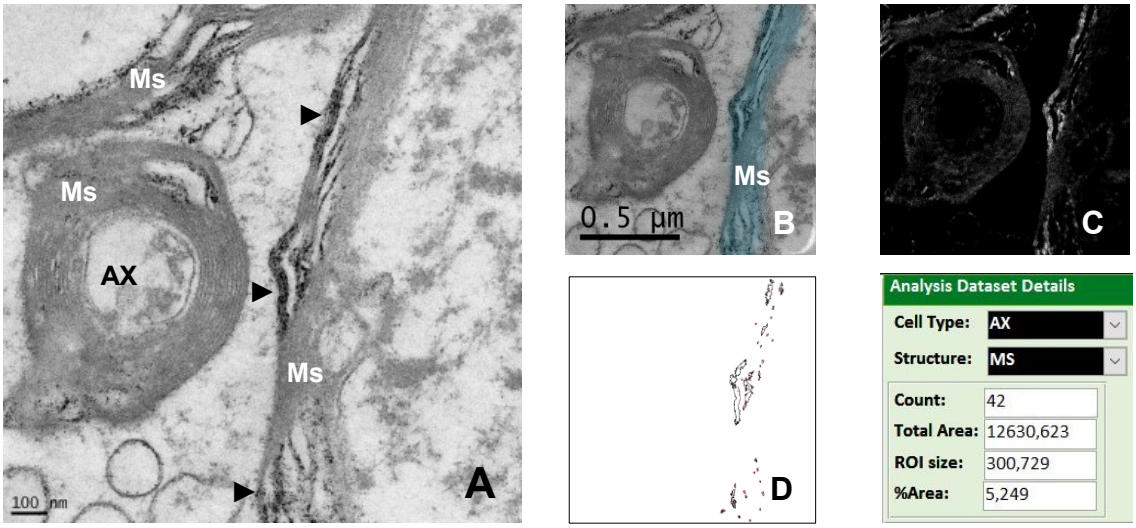

Figure 28: Myelin Sheath in Frontal White Matter
(**A**): TEM image of an axon (AX) and an adjacent separate myelin sheaths (Ms) from another axon taken at 14,5 k. Arrows (►) mark spots with suspected iron content. (**B**): Elastic image with coloring of one of the myelin sheaths at 19 k. (**C**): Iron M Elemental map. (**D**): Particle analysis picture of the colored myelin sheath shows a % area of *5,249*.

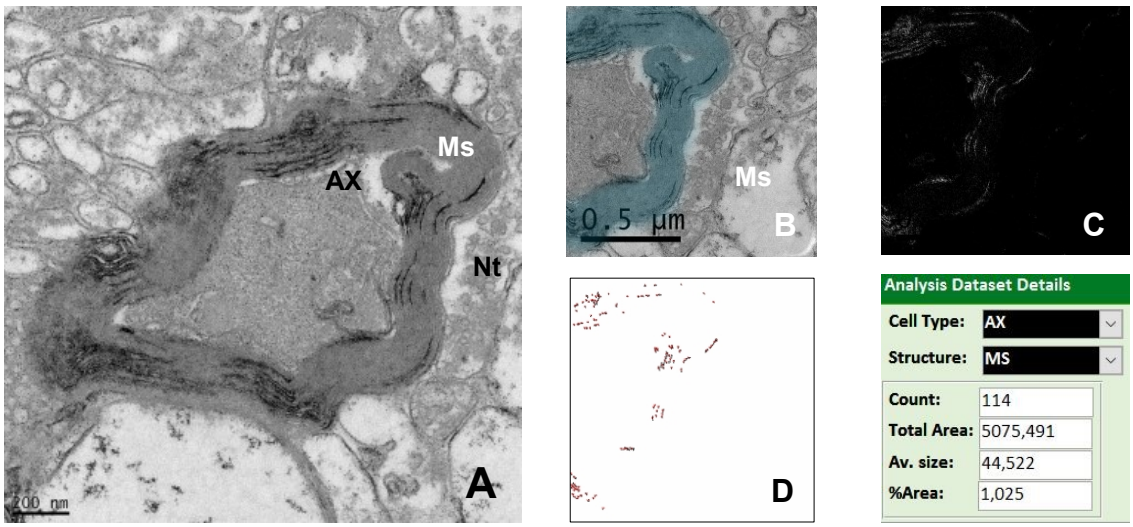

Figure 29: Myelin Sheath in Globus Pallidus
(**A**): TEM image of an axon (AX) and its myelin sheaths (Ms) taken at 11,5 k. Next to the axon a nerve terminal (Nt) can be found (**B**): Elastic image with coloring of one of the myelin sheaths at 19 k. (**C**): Iron M Elemental map. (**D**): Particle analysis picture and analysis of the colored myelin sheath show a % area in transition metal content of *1,025*.

5.3.2.2.1 Degenerated Myelin Sheaths

Of the observed total of myelin sheaths (*n=138*), 79 % (*n=109*) were not rated as degenerative, whereas the remaining 21% (*n=29*) were tagged within DATEM as degenerated. Visible degenerations included loose myelin wrappings, signs of ballooning or other changes in myelin integrity. Nevertheless, the formation of spherical cavities called “balloons” are considered to be age-related changes in myelin sheaths (85). In a few cases, an empty sheath could be observed as previously described in research on senescent primate brains (87). Next to primates, disruptions of myelin were abundantly found in senescent rats and might also be considered as age-related changes in humans without correlating neuropathological clinical symptoms (88). Although not observed frequently, still the highest area percentage can be seen in neurodegenerative myelin sheaths in the corpus callosum, frontal cortex and globus pallidus. The least neurodegeneration in myelin sheaths was marked within the putamen (***Figure 32***).

Table 20: Degenerated/Non-degenerated Myelin Sheath Frequencies

		Frequency	Percent
Valid	not degenerated	109	79,0
	degenerated	29	21,0
	Total	138	100,0

Table 21: % Area of Degenerated/Non-degenerated Myelin Sheaths

Descriptive Statistics

degenerative		N	Minimum	Maximum	Mean	SD
not degenerated	**%Area**	**109**	**,000**	**5,937**	**1,02029**	**1,364526**
	Valid N (listwise)	109				
degenerated	**%Area**	**29**	**,016**	**5,455**	**1,54200**	**1,509961**
	Valid N (listwise)	29				

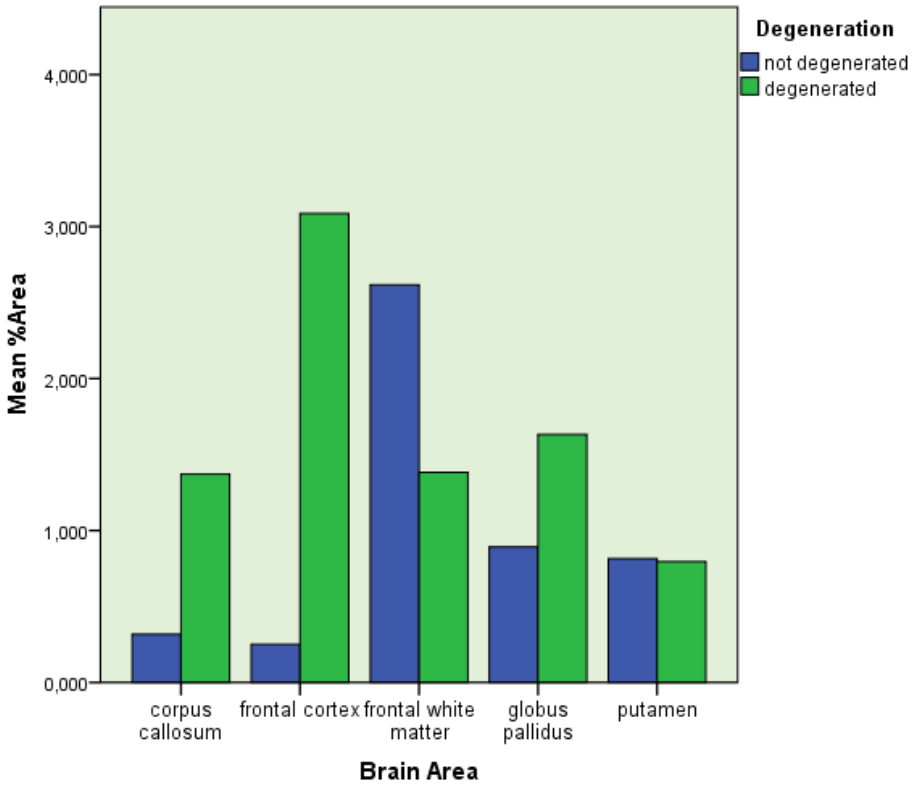

Figure 30: Bar Graph Comparison of Mean % Area of Degeneration in Myelin Sheaths per Brain Area
The frontal cortex contained the highest mean % area of transition metal content in degenerated myelin sheaths marked within dataset.

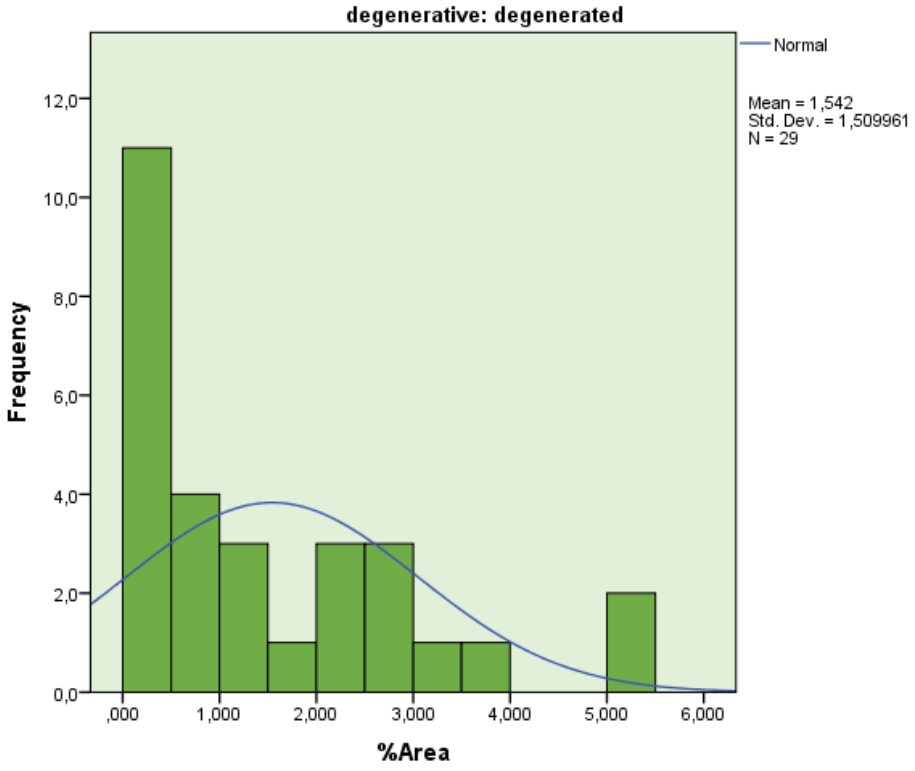

Figure 31: Histogram of % Area Frequencies of degenerated Myelin Sheaths

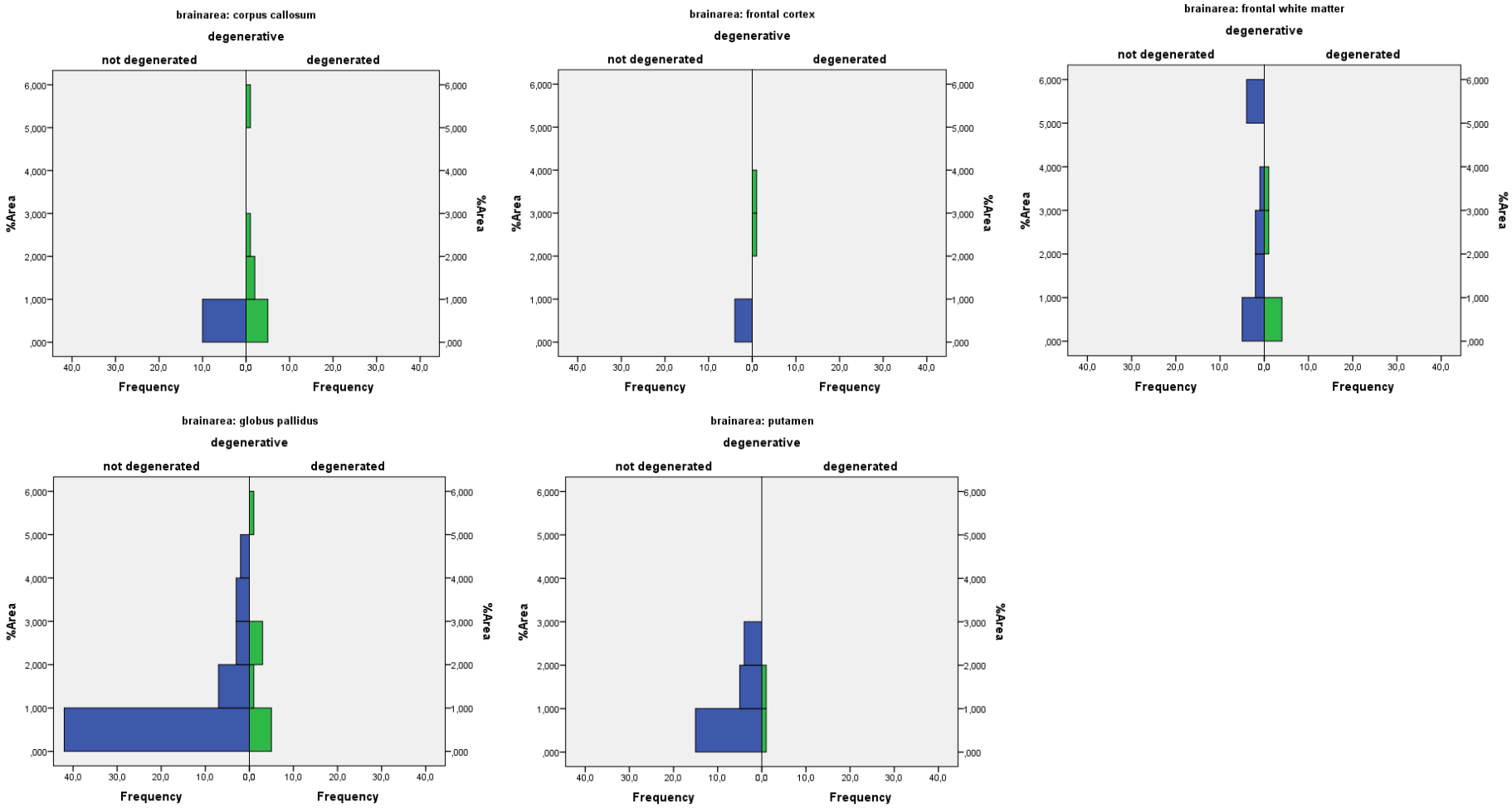

Figure 32: Comparison between degenerated and non-degenerated Myelin Sheaths in Brain Areas

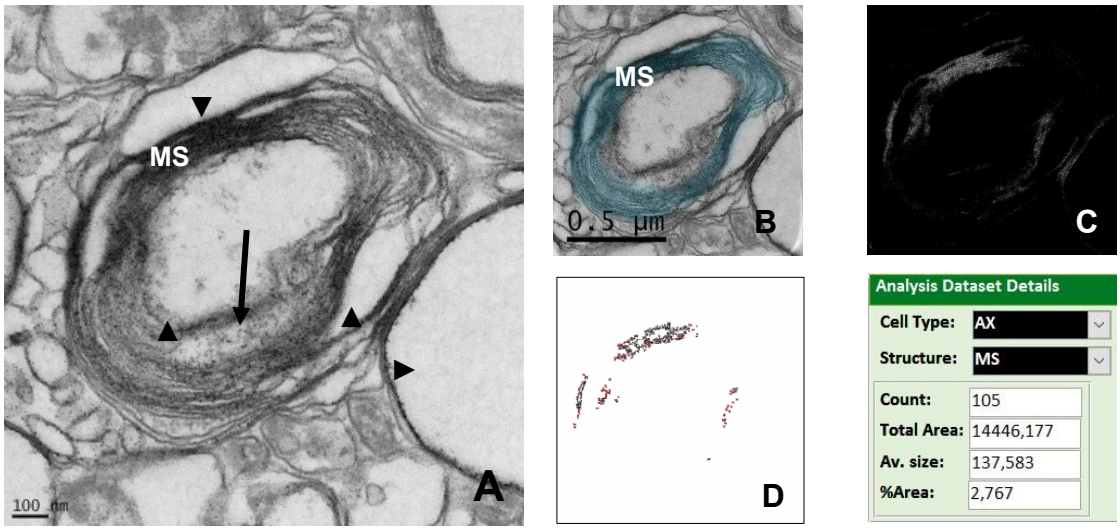

Figure 33: Degenerated Myelin Sheaths in GP
(**A**): TEM image of a degenerated axon taken at 14,5 k magnification. Arrows (▲►▼◄) point to different places of empty sheaths. The dense area within the axon (↓) might be an oligodendrocitic process rebuilding the damaged myelin (**B**): Elastic image with coloring of the myelin sheath of the center at 19 k. (**C**): Elemental map. (**D**) shows particle analysis of the colored area, revealing a % area of *2,767*.

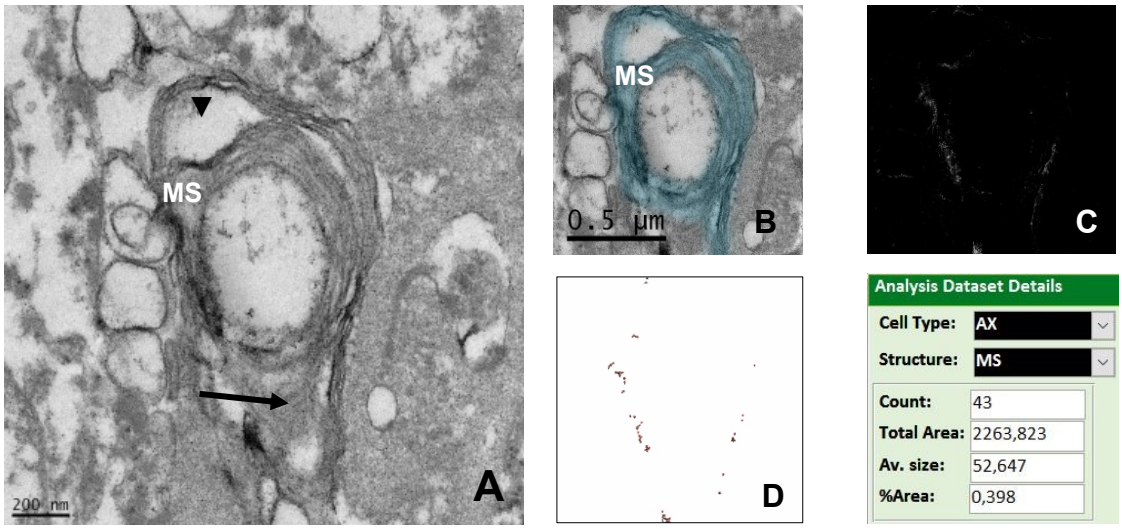

Figure 34: Degenerated Myelin Sheaths in Putamen
(**A**): TEM image of a degenerated axon taken at 11,5 k magnification. Arrow (▼) points to an empty sheath. The dark cytoplasmatic area (→) might be an oligodendrocitic remyelinization process (**B**): Elastic image with coloring of the myelin sheath of the center at 19 k. (**C**): Elemental map. (**D**) shows inverted elemental map, whereas particle analysis of the ROI shows a % area of *,398*.

5.3.2.3 Axoplasm

A total of 57 substructures of axons were categorized and colored as axoplasm in the sample images (***Table 22***).

Table 22: Axoplasm Frequencies per Brain Area

	brainarea	Frequency	Percent
Valid	corpus callosum	8	14,0
	frontal cortex	4	7,0
	frontal white matter	3	5,3
	globus pallidus	29	50,9
	putamen	13	22,8
	Total	57	100,0

Table 23: % Area per Brain Area in Axoplasm

Descriptive Statistics

celltypes	cellstructure	brainarea		N	Min.	Max.	Mean	SD
axon	axoplasm	corpus callosum	**%Area**	**8**	**,000**	**,311**	**,05612**	**,108836**
			Valid N (listwise)	8				
		frontal cortex	**%Area**	**3**	**,000**	**,000**	**,00000**	**,000000**
			Valid N (listwise)	3				
		frontal white matter	**%Area**	**3**	**,000**	**,033**	**,01100**	**,019053**
			Valid N (listwise)	3				
		globus pallidus	**%Area**	**29**	**,000**	**1,666**	**,10341**	**,330540**
			Valid N (listwise)	29				
		putamen	**%Area**	**13**	**,000**	**,213**	**,02969**	**,062084**
			Valid N (listwise)	13				

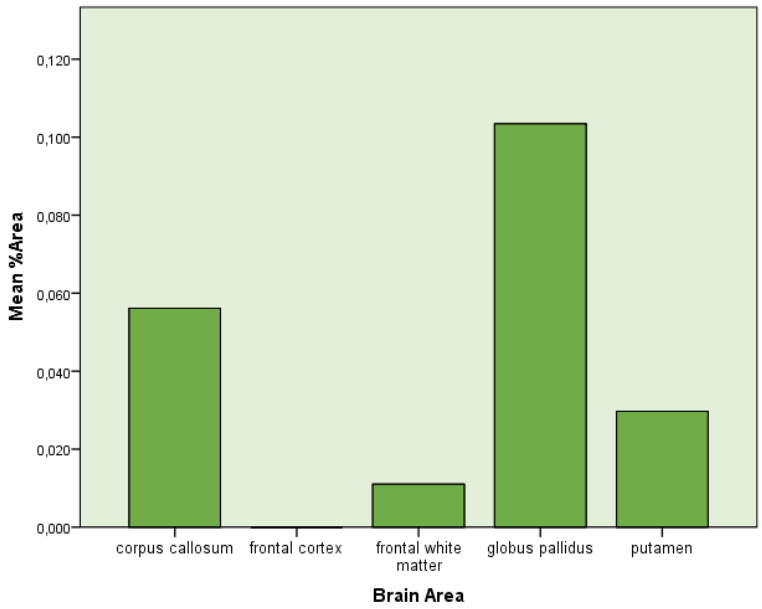

Figure 35: Bar Graph of Mean % Area in Axoplasms per Brain Area
The globus pallidus showed the highest % area for transition metal content within axoplasm (*N=29; M=,10341; SD= ,33054*).

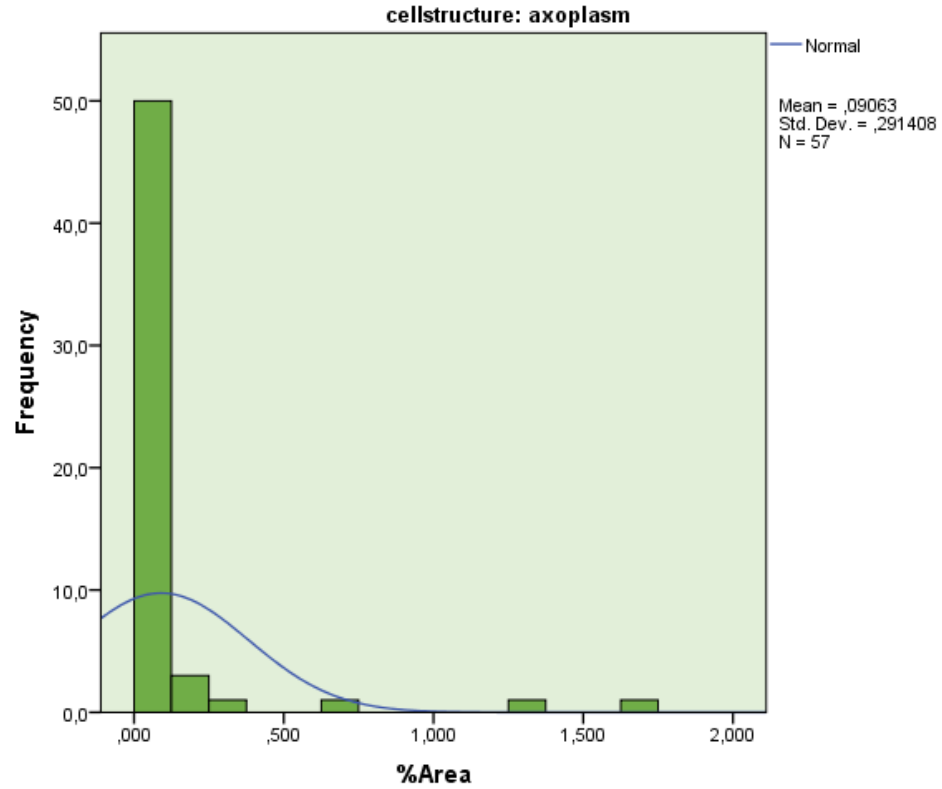

Figure 36: Histogram of % Area Frequencies of Axoplasm
Frequencies of % area of axoplasms show a right-skewness in the box-plots. The majority of axoplasm showed no transition metal content, whilst highest % areas of outliers reach up to a maximum of *1,666 %*.

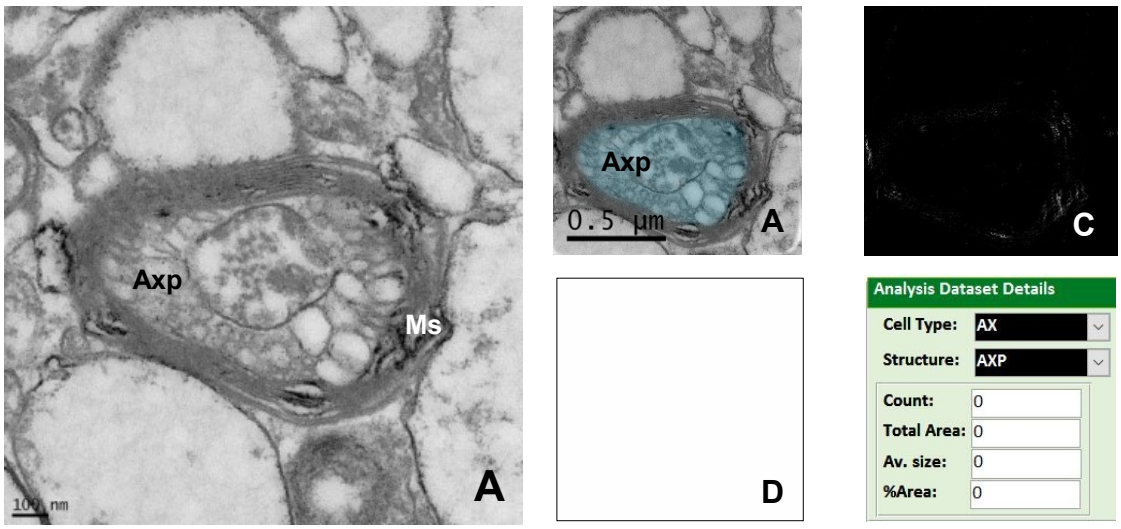

Figure 37: Axoplasm in Globus Pallidus
(**A**): TEM image of an axon taken at 14,5 k magnification in a globus pallidus sample. Axoplasm (Axp) is surrounded by the adjacent myelin sheath (Ms) (**B**): Elastic image with coloring of the axoplasm at 19 k. (**C**): Elemental map. While myelin sheath clearly shows transition metal content, no visible staining can be seen within axoplasmatic structures (**D**) shows particle analysis of the axoplasmatic area, which shows no transition metal content within corresponding analysis.

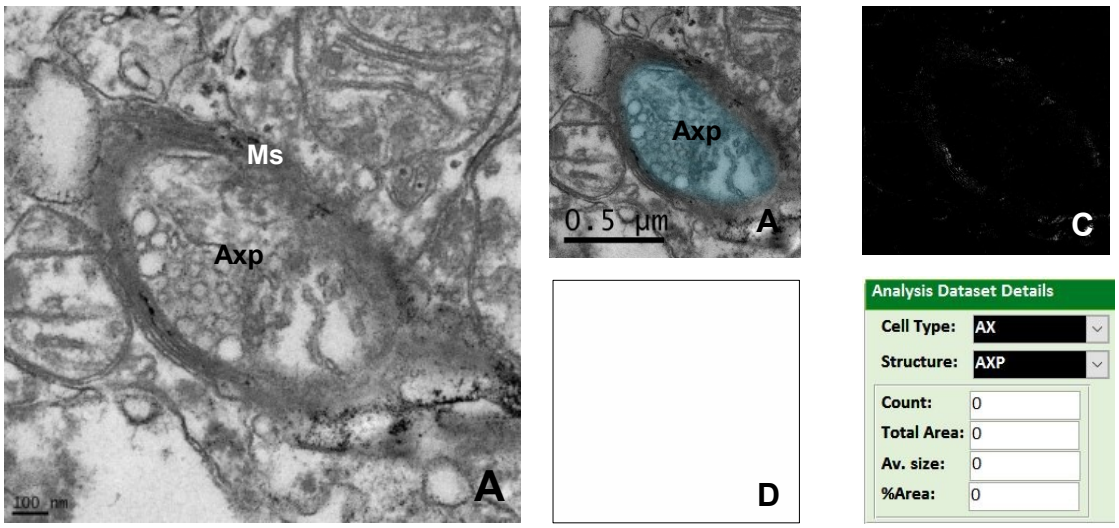

Figure 38: Axoplasm in Frontal Cortex
(**A**): Axon at 14,5 k magnification with clearly visible cytoskeletal elements within axoplasm (Axp) (**B**): Elastic image with coloring of the axoplasm at 19 k. (**C**): Elemental map of whole image shows major staining for myelin sheath. (**D**): Particle analysis of the axoplasmatic area shows no transition metal content within analysis.

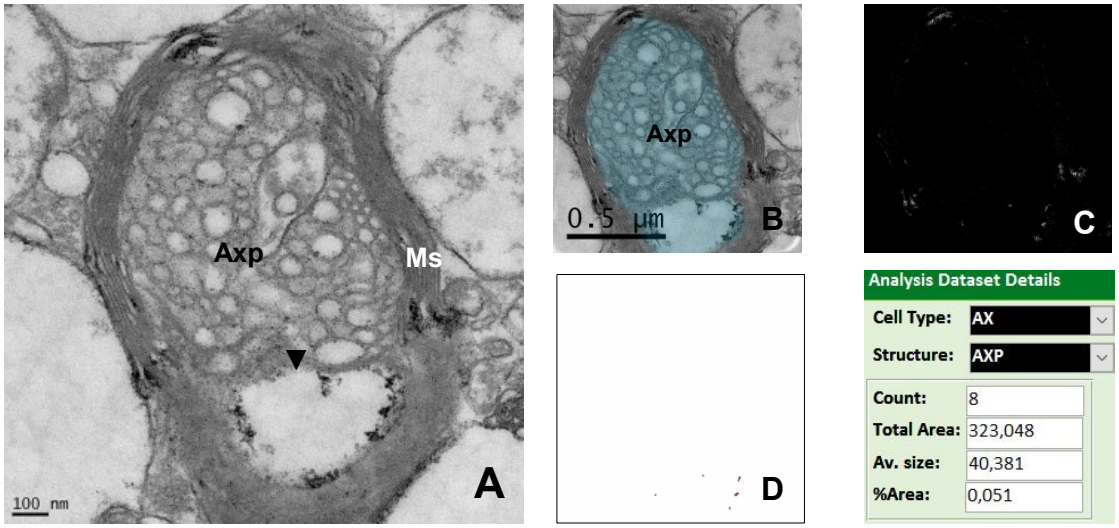

Figure 39: Axoplasm in Globus Pallidus
(**A**): Axoplasm (Axp) of an axon taken at 14,5 k magnification in TEM mode. Multiple cytoskeletal elements are incorporated in the axoplasm (**B**): Elastic image with colored axoplasm at 19 k. (**C**): Elemental map of whole image (**D**): Particle analysis of the axoplasm shows a % area in transition metal content of *,051*, mainly distributed on the border between the vacuole (▼) and myelin sheath.

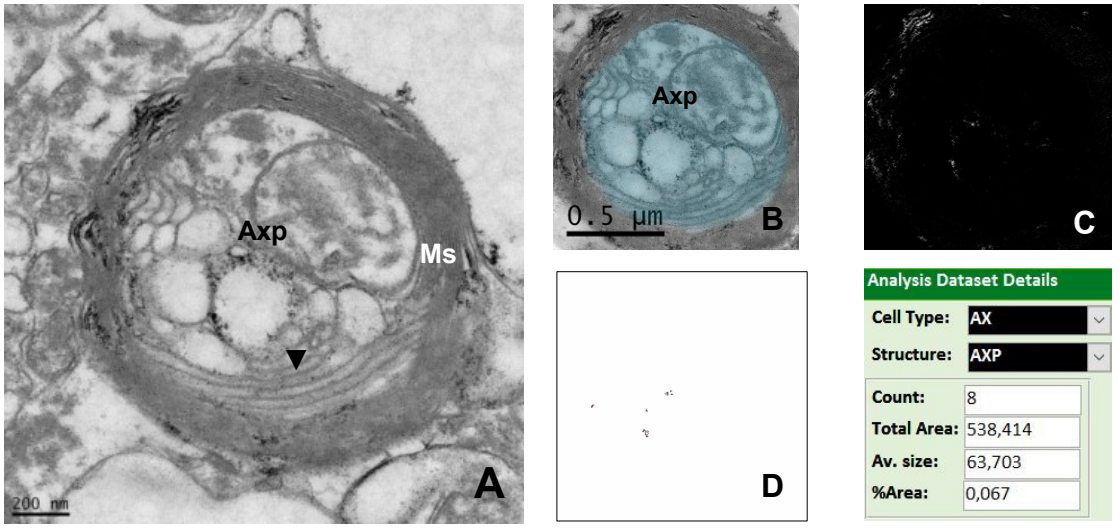

Figure 40: Axoplasm in Globus Pallidus
(**A**): TEM image of an axoplasm (Axp) of an axon taken at 11,5 k magnification. The fine linings of the myelin sheath (▼) on the inner border might also suspect an oligodendrocitic process within the sheath. (**B**): Elastic image with colored axoplasm at 19 k. (**C**): Elemental map of whole image (**D**): Particle analysis of the axoplasm shows a % area in transition metal content of *,067*.

5.3.2.4 Nerve Terminal

Nerve terminals (*N=53*) were categorized as substructures of axons within the sample image dataset (***Table 24***).

Table 24: Nerve Terminal Frequencies per Brain Area

		Frequency	Percent
Valid	corpus callosum	1	1,9
	frontal cortex	8	15,1
	frontal white matter	2	3,8
	globus pallidus	26	49,1
	putamen	16	30,2
	Total	53	100,0

Table 25: % Area per Brain Area in Nerve Terminal

Descriptive Statistics

celltypes	cellstructure	brainarea		N	Min.	Max.	Mean	SD
axon	nerve terminal	corpus callosum	**%Area**	**1**	**,000**	**,000**	**,00000**	**.**
			Valid N (listwise)	1				
		frontal cortex	**%Area**	**8**	**,000**	**1,966**	**,40613**	**,643406**
			Valid N (listwise)	8				
		frontal white matter	**%Area**	**2**	**,000**	**,023**	**,01150**	**,016263**
			Valid N (listwise)	2				
		globus pallidus	**%Area**	**26**	**,000**	**1,625**	**,18050**	**,379283**
			Valid N (listwise)	26				
		putamen	**%Area**	**16**	**,000**	**,198**	**,02231**	**,049562**
			Valid N (listwise)	16				

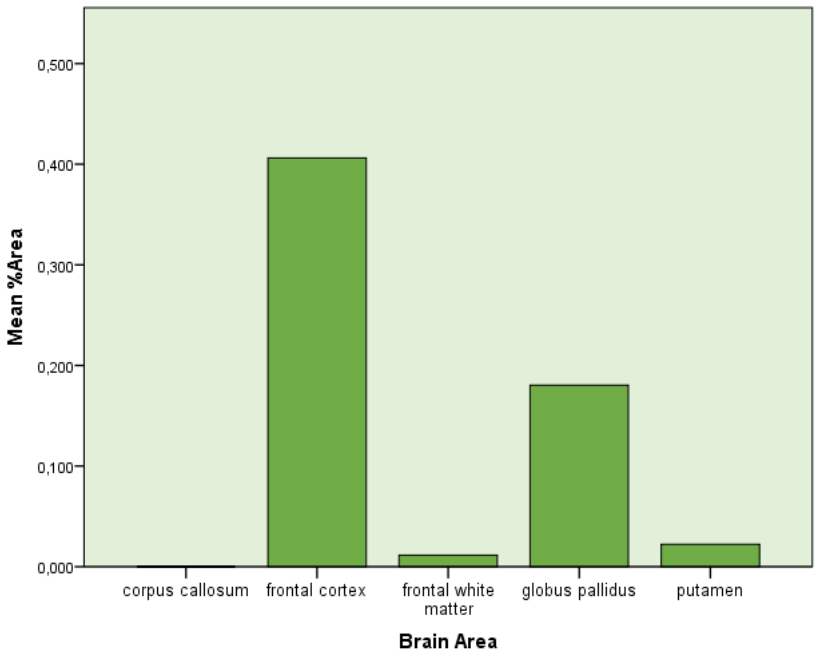

Figure 41: Bar Graph of Mean % Area of Nerve Terminals per Brain Area
The frontal cortex showed the highest % area for transition metal content within nerve terminals (*Max.=1,966; M=,40613, SD=,643*).

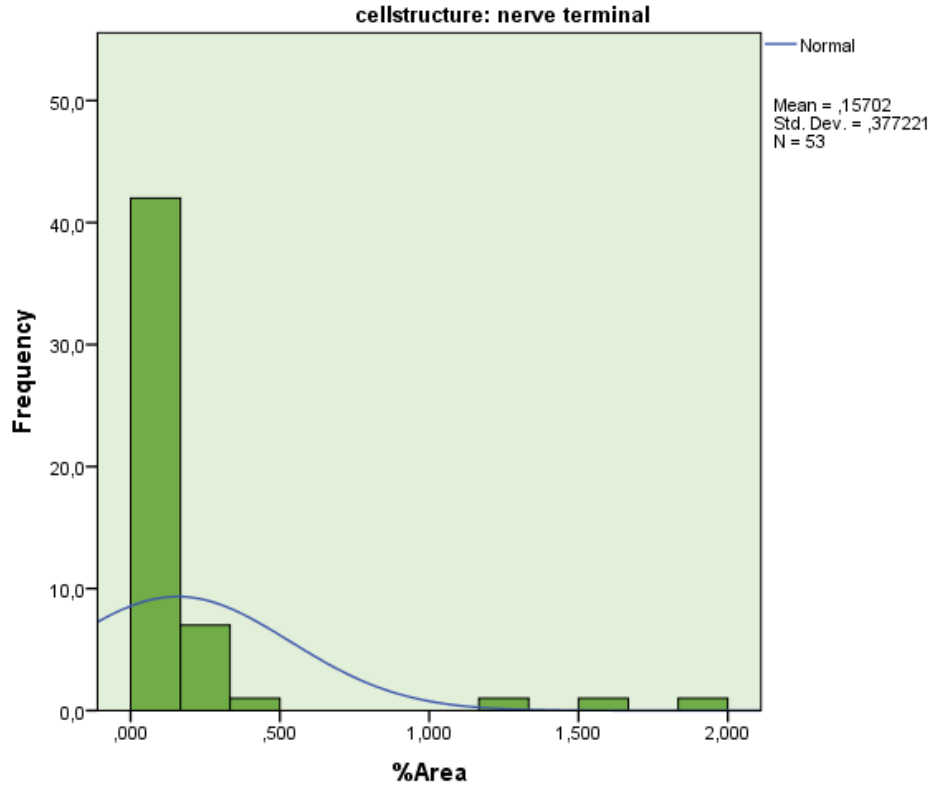

Figure 42: Histogram of % Area Frequencies of Nerve Terminals

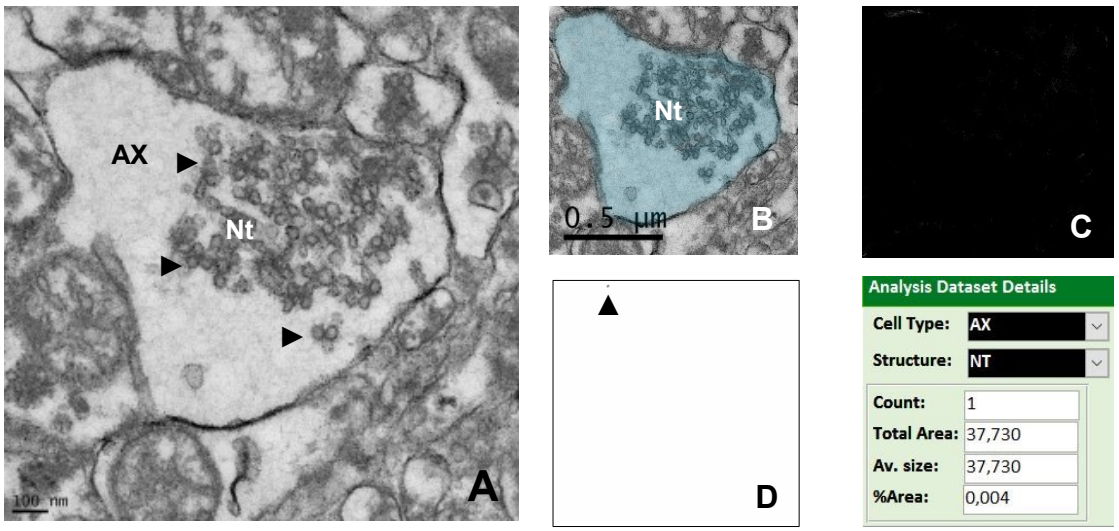

Figure 43: Nerve Terminal in the Putamen
(**A**): TEM image of an axonal nerve terminal with multiple accumulations of vesicles (►) taken at 14,5 k magnification. (**B**): Elastic image of the axon with nerve terminal colored for particle analysis. (**C**): Iron M Elemental Map of the whole region. (**D**) Inverted version after IrfanView processing and after particle analysis shows one transition metal particle (▲). Next to it are the analysis details transmitted into DATEM showing a % area of *0,004*.

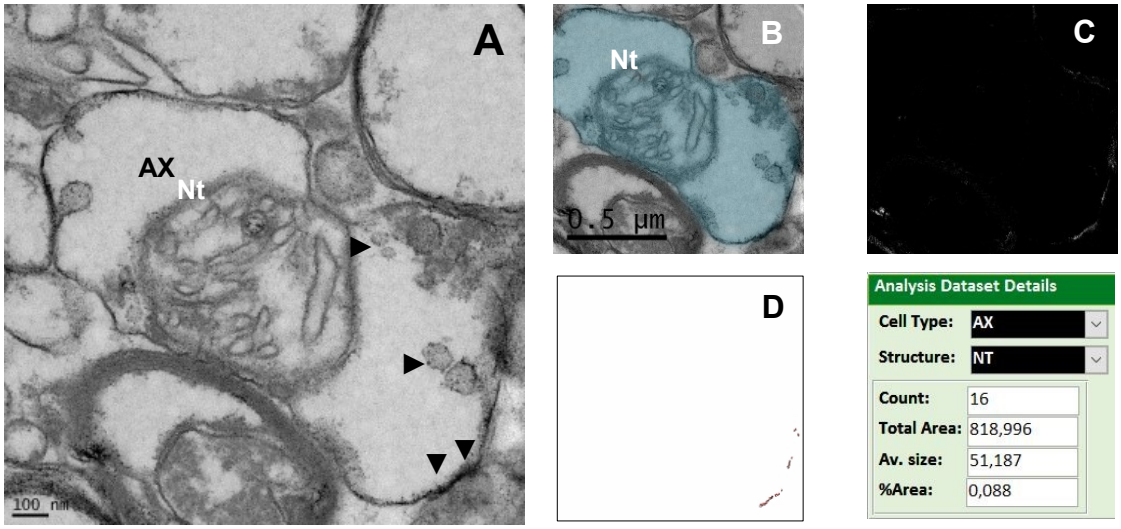

Figure 44: Nerve Terminal in the Globus Pallidus
(**A**): TEM image of an axonal nerve terminal with small and large vesicles (►) at 14,5 k magnification. Arrows (▼) show to the bouton of the nerve terminal (**B**): Colored elastic image of nerve terminal. (**C**): Iron M Elemental Map of the whole image for subsequent analysis at 19 k. (**D**) Inverted elemental map after particle analysis of the region shows transition metal content at the bouton (▼). Analysis shows a % area of *,088*.

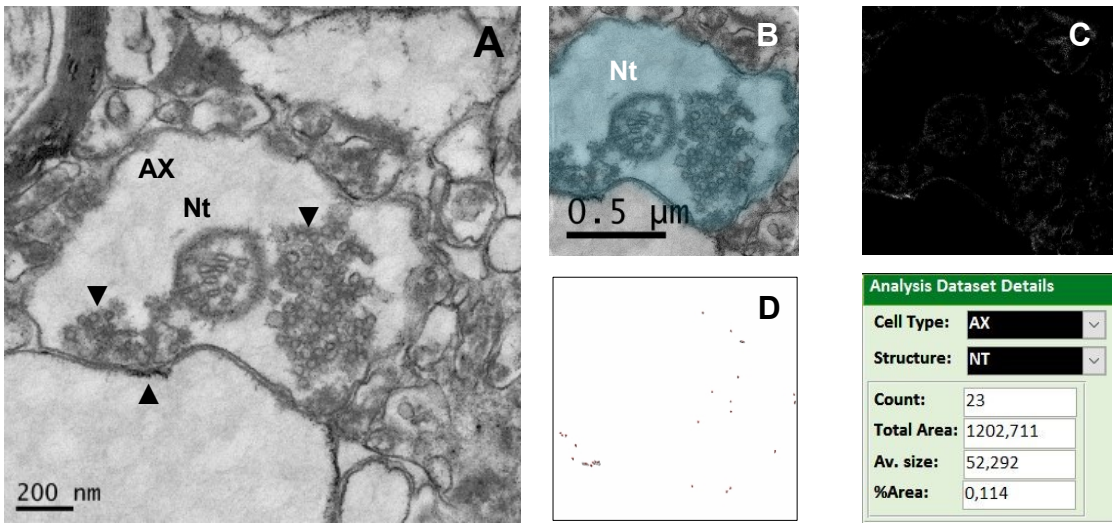

Figure 45: Nerve Terminal in the Frontal Cortex
(**A**): Axonal nerve terminal with multiple vesicles (▼) in TEM at 11,5 k magnification. Synaptic bouton (▲) can be seen on the bottom of the nerve terminal (**B**): Colored elastic image of nerve terminal. (**C**): Iron M Elemental Map of the whole image for subsequent analysis. (**D**) Inverted elemental map after particle analysis of the region shows transition metal content at the bouton (▲) and around the vesicles (▼). Analysis reveals a % area of *,114*.

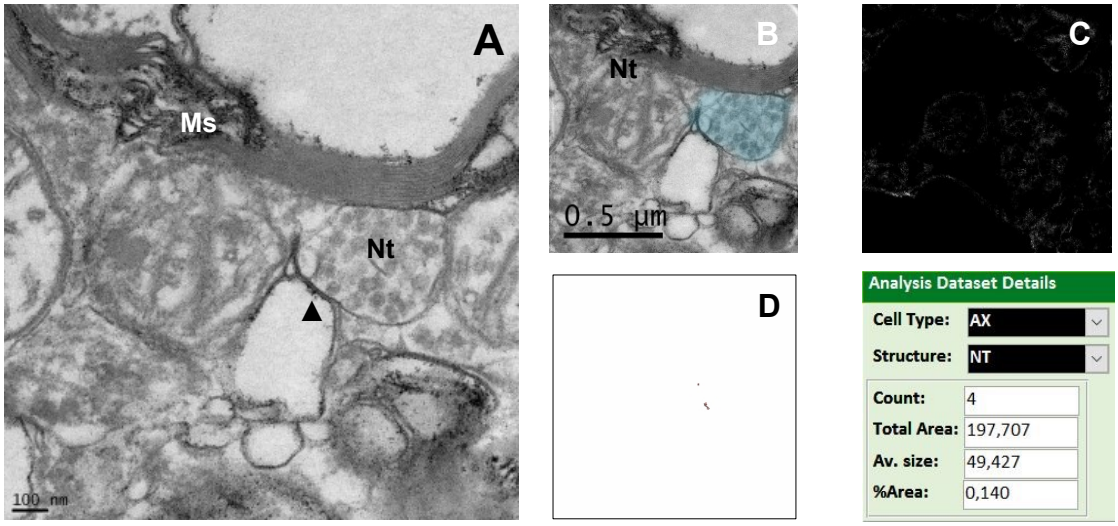

Figure 46: Nerve Terminal in the Frontal Cortex
(**A**): Nerve terminal with vesicles in TEM at 11,5 k magnification with visible synaptic bouton (▲). (**B**): Colored elastic image of nerve terminal. (**C**): Iron M Elemental Map. (**D**) Inverted elemental map after particle analysis of the region of interest. Particle analysis reveals a % area of transition metal content of *,140*.

5.3.3 Dendrites

A total of 188 dendrites as cell types were analyzed within the final dataset (***Table 26***). Dendrites in available brain regions were categorized in two different substructures: Dendritic spines (*N=165*), discussed in this chapter, and underlying mitochondria (*N=23*), discussed in ***section 5.3.6.1***,.

Table 26: Dendritic Spines Frequencies per Brain Area

	brainarea	Frequency	Percent
Valid	corpus callosum	14	8,5
	frontal cortex	14	8,5
	frontal white matter	7	4,2
	globus pallidus	63	38,2
	putamen	67	40,6
	Total	165	100,0

Table 27: Dendrite Frequencies per Cell Structure

		Frequency	Percent
Valid	dendritic spines	165	87,8
	mitochondrium	23	12,2
	Total	188	100,0

Table 28: % Area per Brain Area in Dendritic Spines

Descriptive Statistics

celltypes	cellstructure	brainarea		N	Min.	Max.	Mean	Std. Deviation
dendrite	dendritic spines	corpus callosum	**%Area**	**14**	**,000**	**,033**	**,00321**	**,009150**
			Valid N (listwise)	14				
		frontal cortex	**%Area**	**14**	**,000**	**1,203**	**,23250**	**,334194**
			Valid N (listwise)	14				
		frontal white matter	**%Area**	**7**	**,000**	**,106**	**,03186**	**,042113**
			Valid N (listwise)	7				
		globus pallidus	**%Area**	**63**	**,000**	**5,408**	**,28167**	**,787758**
			Valid N (listwise)	63				
		putamen	**%Area**	**67**	**,000**	**1,686**	**,15036**	**,295244**
			Valid N (listwise)	67				

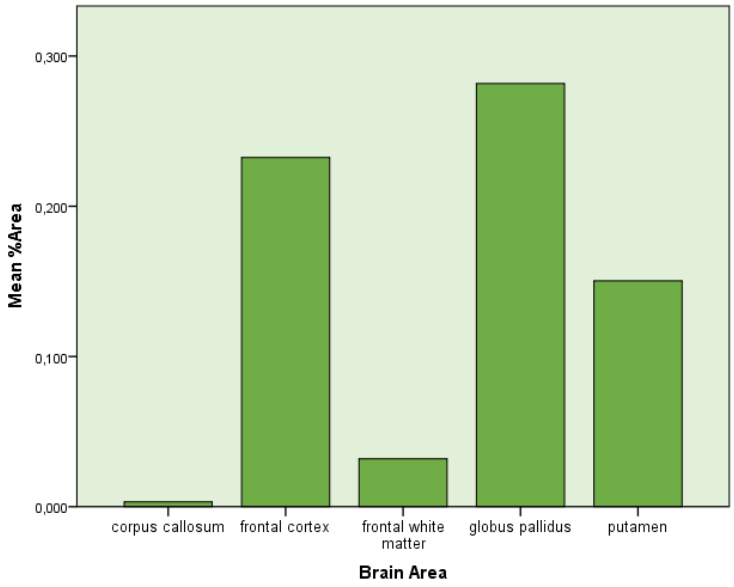

Figure 47: Bar Graph of Mean % Area of Dendritic Spines per Brain Area

The highest % area of transition metal content in cell structures marked as dendritic spines was observed in the globus pallidus (*N=63; M=,2325; SD=,33419*)

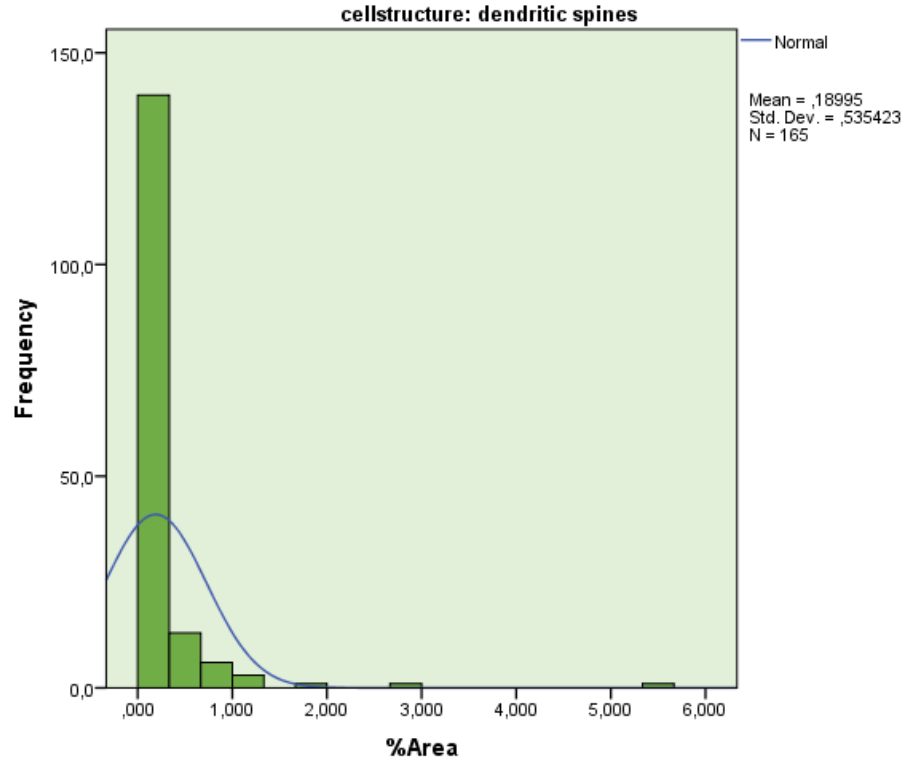

Figure 48: Histogram of % Area Frequencies of Dendritic Spines

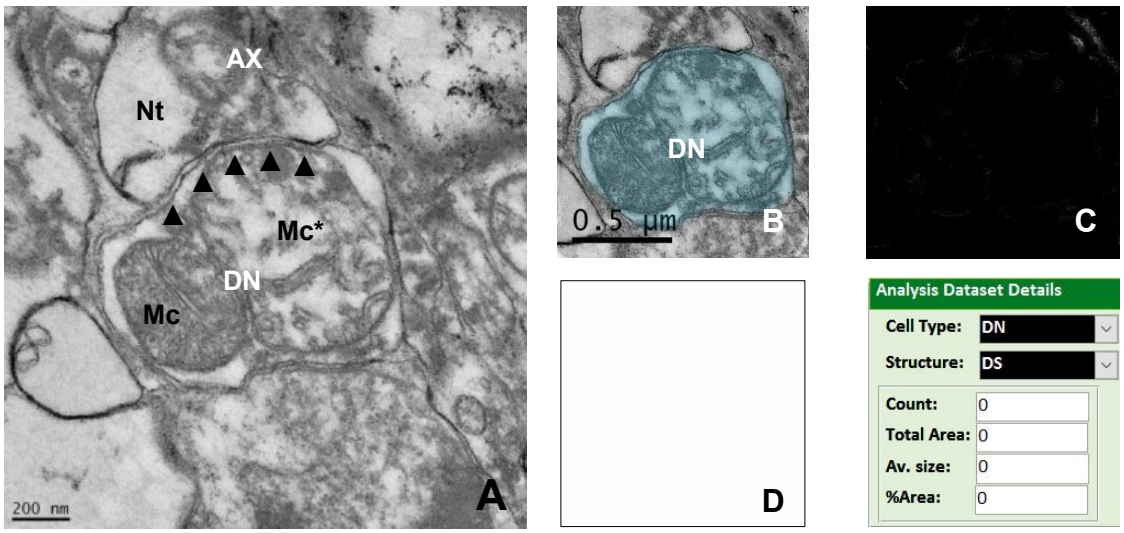

Figure 49: Dendrite in the Putamen
(**A**): TEM image of an axon (AX) nerve terminal (Nt) and an adjacent dendrite (DN) taken at 14,5 k magnification. The synaptic cleft is clearly visible in the horizontal cut (▲) and leads to the dendrite (DN), which also contains two mitochondria (Mc), of which one is clearly swollen (*). (**B**): Elastic image of the area with coloring of the dendrite at 19 k (34 k in EFTEM view). (**C**) shows iron elemental map of the whole image. (**D**): Inversion of the elemental map area with no visible transition metal content and corresponding particle analysis of the marked dendrite.

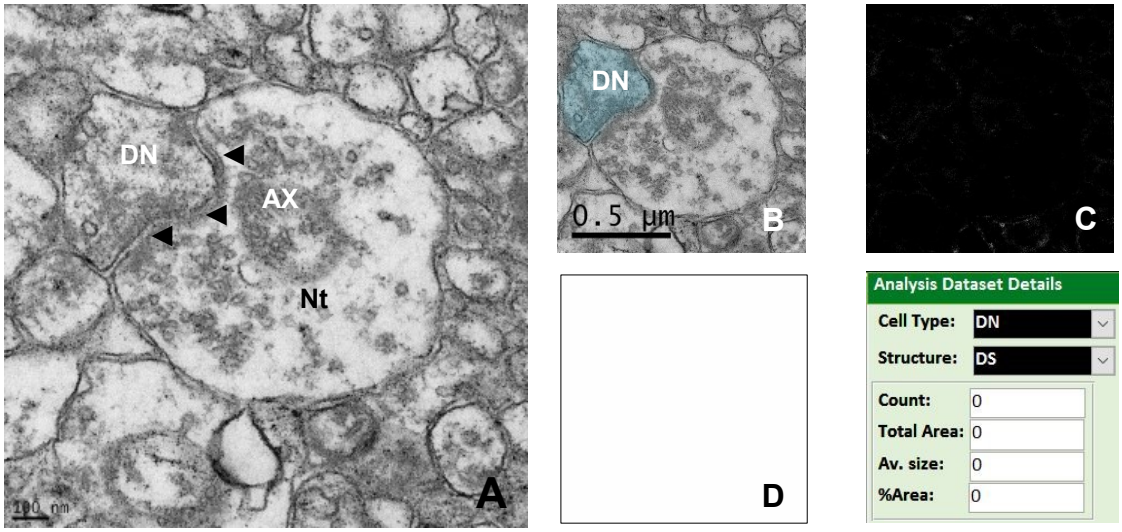

Figure 50: Dendrite in the Globus Pallidus
(**A**): TEM image of an axon (AX) nerve terminal (Nt) and an adjacent dendrite (DN) taken at 14,5 k magnification. Arrows (◄) point to the synaptic bouton between the axon and the dendrite. (**B**): Elastic image with colored dendrite at 19 k. (**C**): Iron elemental map of the whole area. (**D**): Inverted elemental map area with no visible transition metal content and its corresponding analysis.

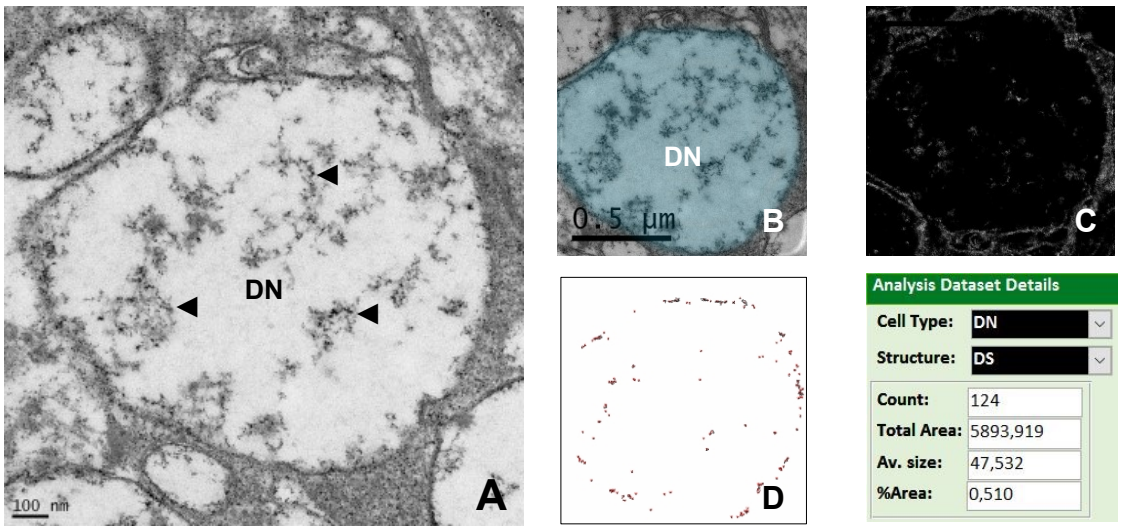

Figure 51: Dendrite in the Putamen
(**A**): A dendrite (DN) taken in TEM mode at 14,5 k magnification. Arrows (◄) show several polyribosomes in the dendrite. (**B**): Elastic image of dendrite coloring at 19 k. (**C**): Iron elemental map of the area. (**D**): Inverted elemental map analysis of the dendritic region shows transition metal content with a % area of *,510*.

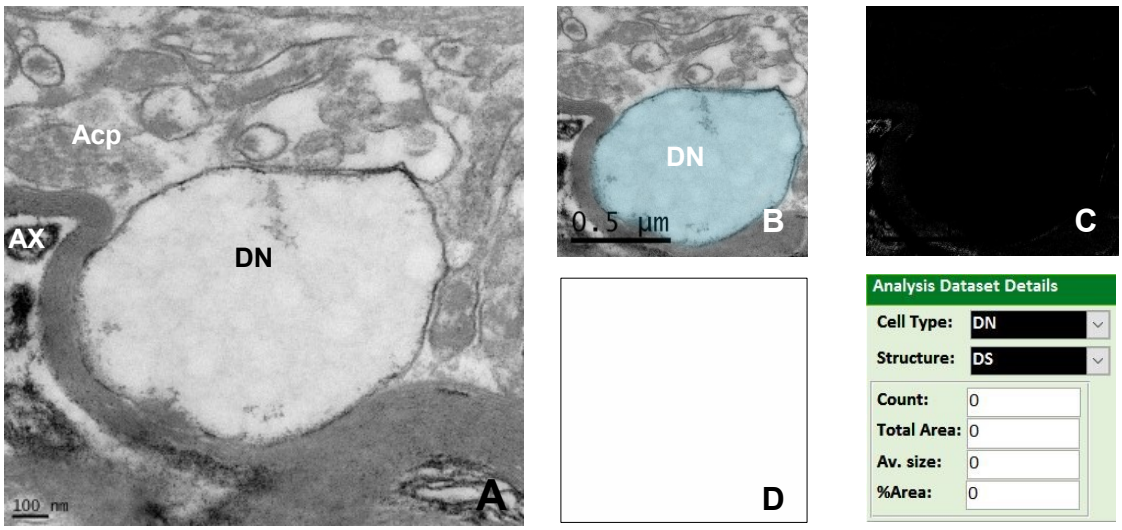

Figure 52: Dendritic Spine in the Globus Pallidus
(**A**): TEM image at 14,5 k magnification of a dendrite (Dn) next to an axon (AX) and an astrocytic process (Acp). (**B**): Elastic image with colored dendrite at 19 k. (**C**): Iron elemental map of the whole area. (**D**): Inverted elemental map area and analysis shows no transition metal content.

5.3.4 Astrocytic Processes

For astrocytes (*N=100*), various underlying cell structures were categorized, including astrocytic processes (*N=73*) as the most abundant types (***Table 30***). Other substructures, such as lipid droplets, lipofuscin granules, mitochondria and the nucleus will be discussed in ***section 5.3.6***. Most astrocyte structures were observed in the globus pallidus (***Table 29***).

Table 29: Astrocyte Frequencies per Brain Area

		Frequency	Percent
Valid	corpus callosum	7	7,0
	frontal cortex	1	1,0
	frontal white matter	8	8,0
	globus pallidus	45	45,0
	putamen	39	39,0
	Total	100	100,0

Table 30: Astrocyte Frequencies per Cell Structure

		Frequency	Percent
Valid	astrocytic process	73	73,0
	lipid droplet	6	6,0
	lipofuscin granules	10	10,0
	mitochondrium	10	10,0
	nucleus	1	1,0
	Total	100	100,0

Table 31: % Area per Brain Area in Astrocytic Processes

Descriptive Statistics

celltypes	cellstructure	brainarea		N	Min.	Max.	Mean	SD
astrocyte	astrocytic process	corpus callosum	**%Area**	**6**	**,000**	**,102**	**,02783**	**,043065**
			Valid N (listwise)	6				
		frontal cortex	**%Area**	**1**	**2,375**	**2,375**	**2,37500**	**.**
			Valid N (listwise)	1				
		frontal white matter	**%Area**	**4**	**,083**	**,302**	**,16025**	**,101700**
			Valid N (listwise)	4				
		globus pallidus	**%Area**	**36**	**,000**	**4,051**	**,24800**	**,723556**
			Valid N (listwise)	36				
		putamen	**%Area**	**26**	**,000**	**1,859**	**,22685**	**,422257**
			Valid N (listwise)	26				

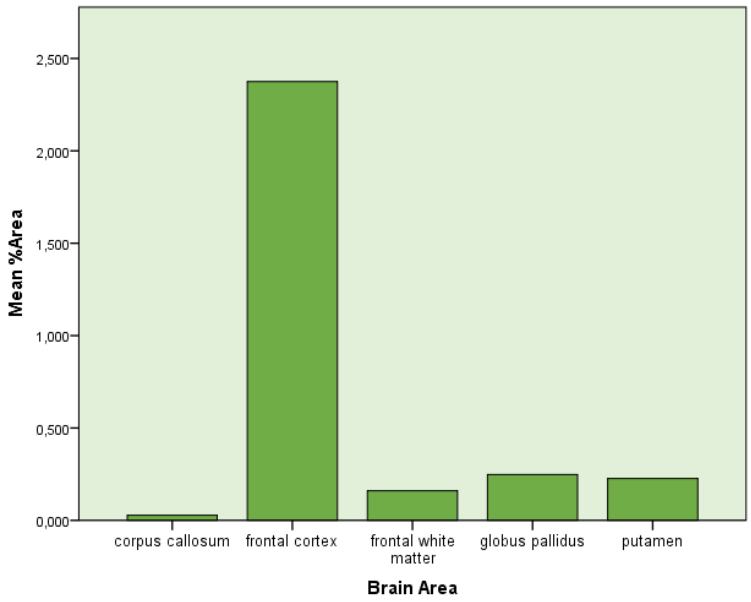

Figure 53: Bar Graph of Mean % Area of Astrocytes per Brain Area

The only suspected astrocyte identified within the frontal cortex also showed the by far highest % area due to glycogen content (*N=1, M=2.375*), which therefore can't be taken for granted. The more replicable and second highest amount of % area in transition metal content was in globus pallidus (*N=36; M=,2480; SD=,7235*).

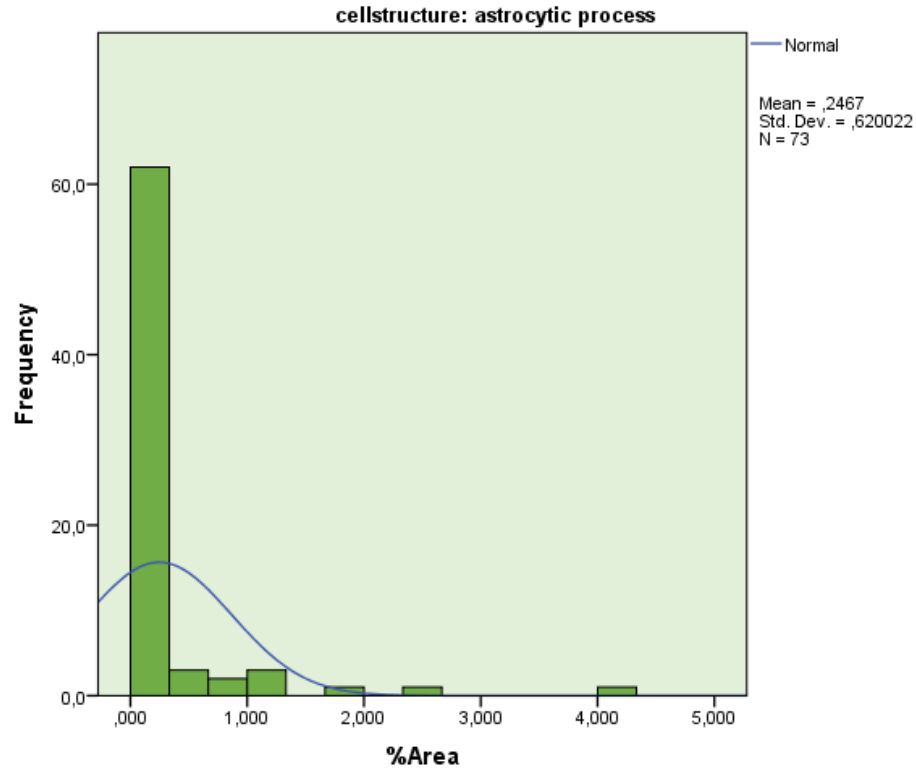

Figure 54: Histogram of % Area Frequencies of Axoplasm

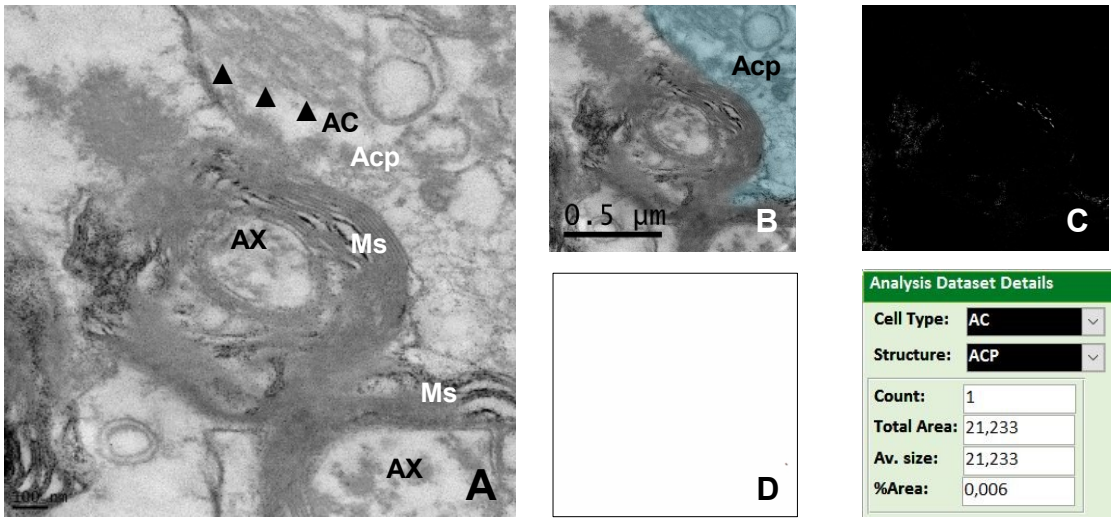

Figure 55: Astrocytic Process in Corpus Callosum
(**A**): An astrocytic process (Acp) embracing the myelin sheaths (Ms) of 2 adjacent axons (AX). The intermediate gliofilaments visible (▲) are characteristic of an astrocyte. TEM image was acquired in at 14,5 k in the corpus callosum. (**B**): Elastic image with coloring of the astrocytic process. (**C**): Iron M elemental map of whole area. (**D**): Inverted elemental mapping of the astrocytic region shows transition metal content of a % area of *,006*.

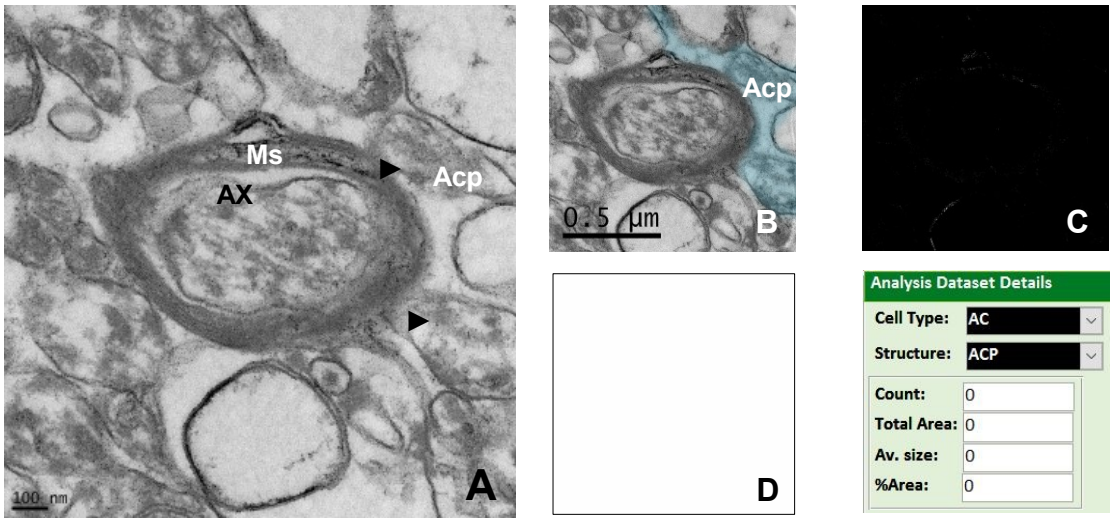

Figure 56: Astrocytic Process in Globus Pallidus
(**A**): An astrocytic process (Acp) around the myelin sheath (Ms) of an axon (AX) taken in TEM mode at 14,5 k. Intermediate filaments (►) can be seen within the process. (**B**): Colored unfiltered elastic image of the astrocytic process. (**C**): Iron M elemental map of whole area. (**D**): Inverted elemental mapping and particle analysis of the astrocytic process show no transition metal content (% area of *,00*).

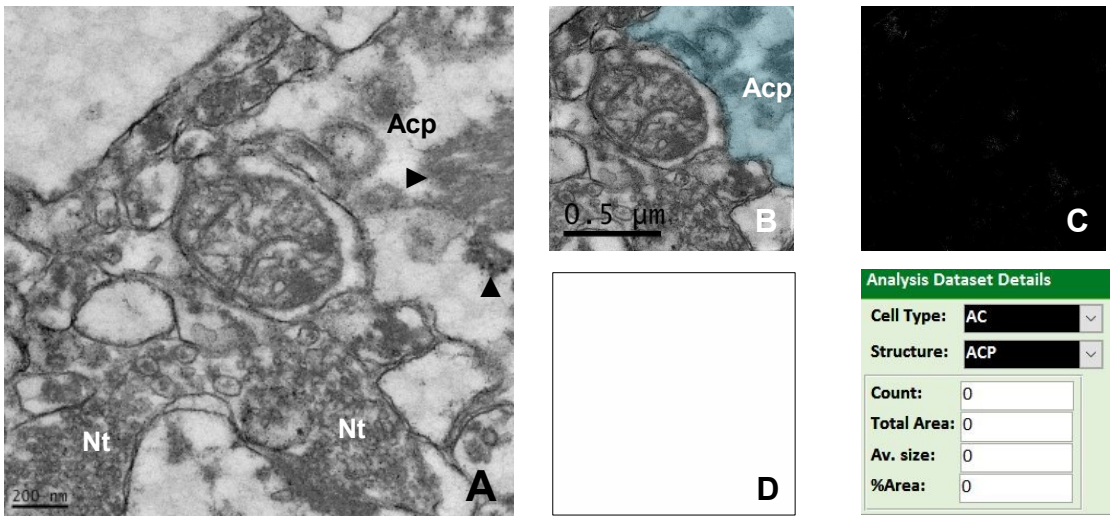

Figure 57: Astrocytic Process in Putamen
(**A**): TEM image of an astrocytic process (Acp) at 19 k, presumed due to characteristic intermediate filaments (►) and glycogen granules (▲). A large nerve terminal (NT) with multiple vesicles is in close proximity (**B**): Elastic image with coloring of the astrocytic process. (**C**): Iron M elemental map of whole area. (**D**): Inverted elemental mapping of the colored region and particle analysis show no transition metal content.

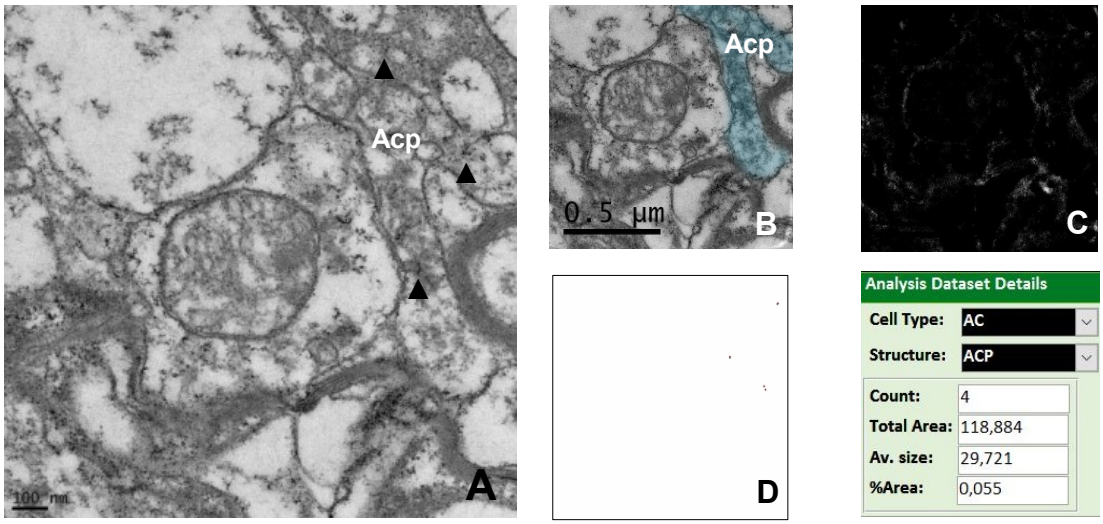

Figure 58: Astrocytic Process in Putamen
(**A**): Suspected astrocytic process (Acp) observed in the putamen at 14,5 k. Some glycogen inclusions are visible (▲). (**B**): Elastic image with coloring of the astrocytic process. (**C**): Iron M elemental map of whole area. (**D**): Elemental map inversion of colored region with particle analysis show transition metal content of a % area of *,055*.

5.3.5 Oligodendrocytes

Oligodendrocytes (*N=141*) were respectively categorized as a substructure of oligodendrocitic processes (*N=134*) and mitochondria (*N=7*). Most oligodendrocitic processes were predominantly identified by their close proximity to observed myelinated axons and their dense cytoplasm. Only a low quantity of oligodendrocitic processes showed any signs of transition metal contents. As mitochondria and their overlying cell types are separately discussed (***section 5.3.6.1***), focus will be put on the oligodendrocitic processes as corresponding substructure of oligodendrocytes.

Table 32: Oligodendrocyte Frequencies per Cell Structure

		Frequency	Percent
Valid	mitochondrium	7	5,0
	oligodendrocitic process	134	95,0
	Total	141	100,0

Table 33: Oligodendrocyte Frequencies per Brain Area

		Frequency	Percent
Valid	corpus callosum	14	9,9
	frontal cortex	11	7,8
	frontal white matter	9	6,4
	globus pallidus	50	35,5
	putamen	57	40,4
	Total	141	100,0

Table 34: % Area per Brain Area in Oligodendrocitic Processes

Descriptive Statistics

cellstructure	brainarea		N	Min.	Max.	Mean	SD
oligodendrocitic process	corpus callosum	**%Area**	**14**	**,000**	**,675**	**,16293**	**,236546**
		Valid N (listwise)	14				
	frontal cortex	**%Area**	**8**	**,000**	**1,472**	**,33325**	**,487491**
		Valid N (listwise)	8				
	frontal white matter	**%Area**	**9**	**,000**	**5,278**	**1,67622**	**2,066763**
		Valid N (listwise)	9				
	globus pallidus	**%Area**	**50**	**,000**	**8,443**	**,66028**	**1,413389**
		Valid N (listwise)	50				
	putamen	**%Area**	**53**	**,000**	**4,714**	**,21387**	**,736086**
		Valid N (listwise)	53				

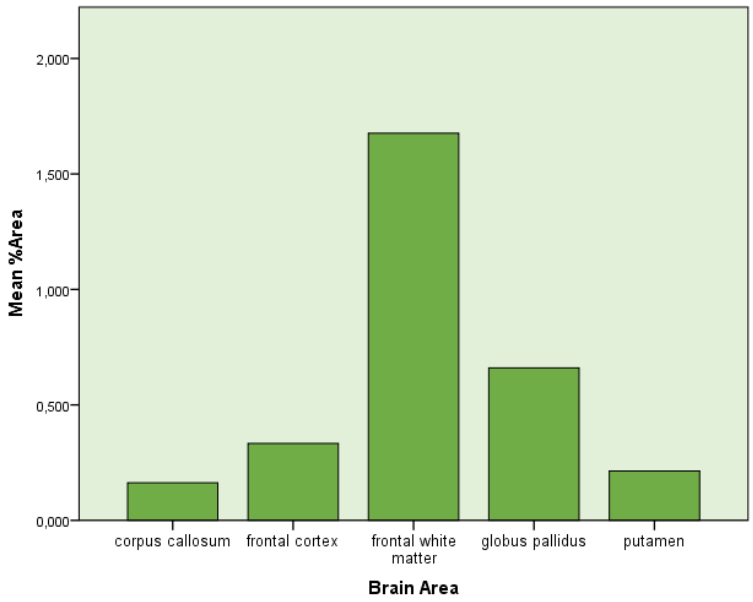

Figure 59: Bar Graph of % Area in Oligodendrocitic Processes per Brain Area
Highest % Area of mitochondrial transition metal content was found in the frontal white matter (*Max.=5,278; M=1,6762; SD=2,0667*).

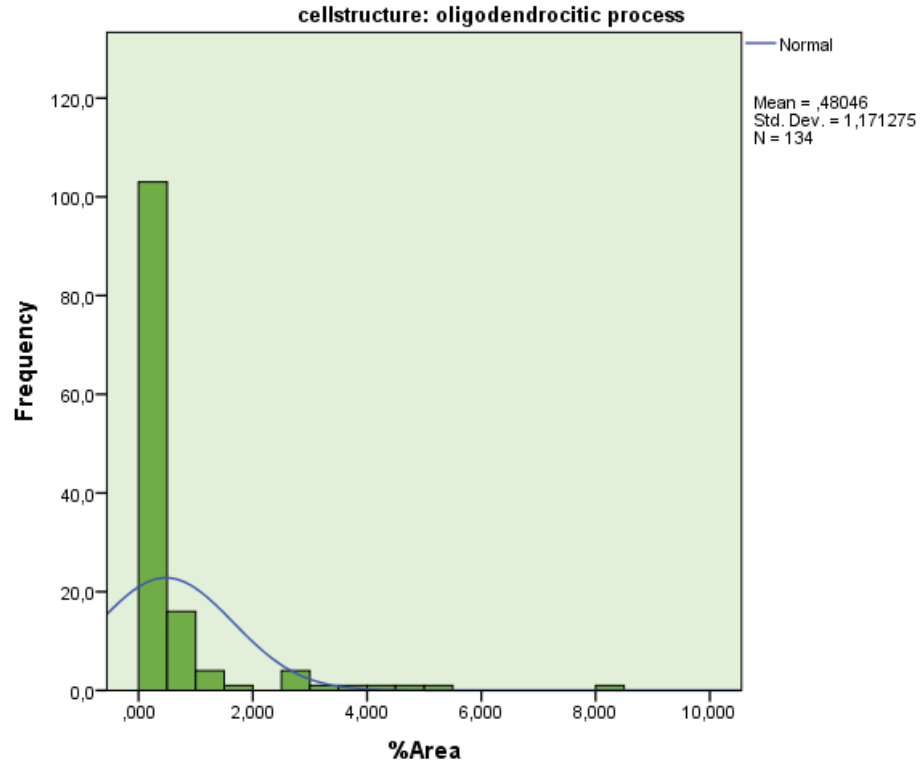

Figure 60: Histogram of % Area Frequencies of Oligodendrocitic Processes

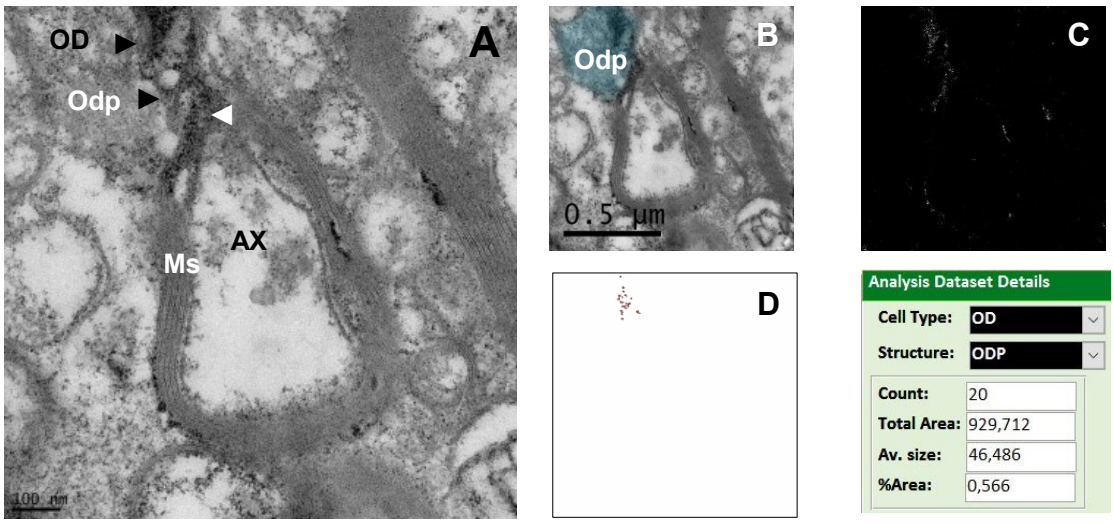

Figure 61: Oligodendrocyte process in Globus Pallidus
(**A**): An oligodendrocitic process (Odp) forming the myelin sheath (Ms) (◄) can be seen next to an axon (AX) in a TEM image taken at 14,5 k in the globus pallidus. Presumed metal content is present as dark spots (►). Note the dense cytoplasm of the oligodendrocitic process (Odp) compared to other related structures. (**B**): Elastic image with coloring of the oligodendrocitic process. (**C**): Iron M elemental map of whole area. (**D**): Inverted elemental mapping shows transition metal content of a % area of *,566* in the oligodendrocitic process.

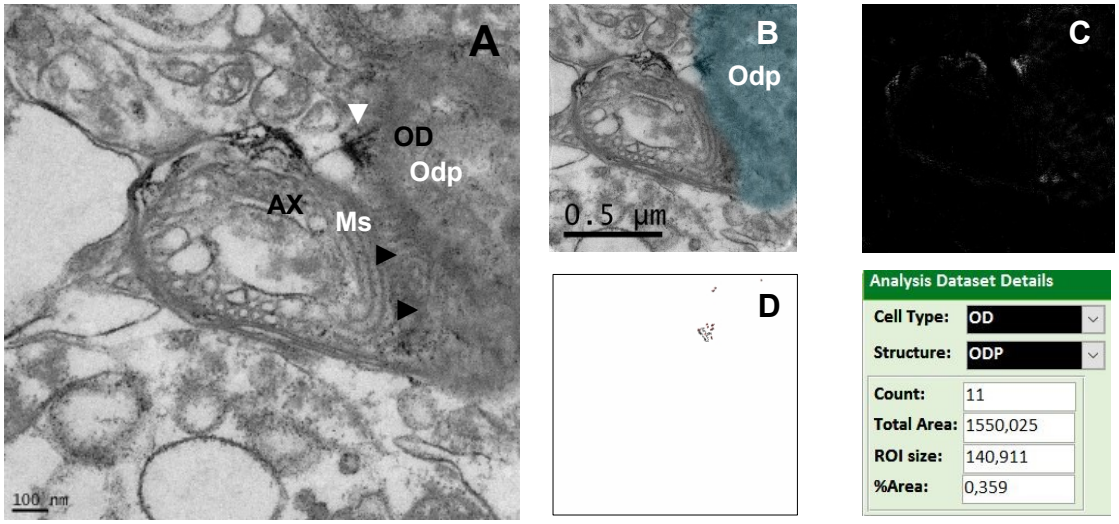

Figure 62: Oligodendrotic Process in the Globus Pallidus
(**A**): Oligodendrocitic process (Odp) from an oligodendrocyte (OD) in TEM at 14,5 k magnification. The transition from the oligodendrocitic process forming the myelin sheath (Ms) from the adjacent axon (AX) is clearly visible (►). Putative iron content with several branches is present within the oligodendrocyte process (▼). (**B**): Colored Elastic image of oligodendrocitic process. (**C**): Iron M Elemental Map. (**D**) Inverted elemental map after particle analysis of the region of interest. Particle analysis reveals a % Area of transition metal content of *,359*.

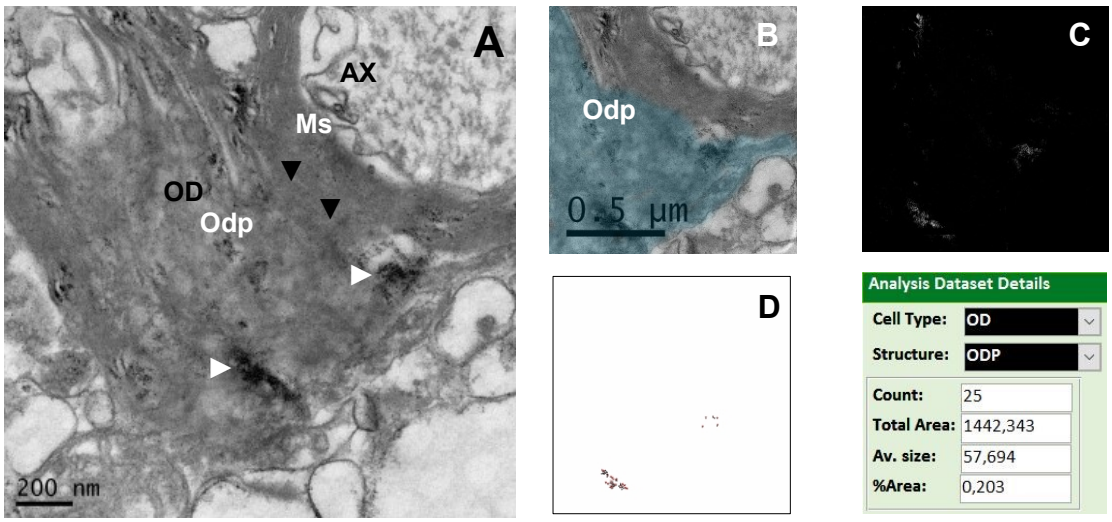

Figure 63: Oligodendrotic Process in the Frontal Cortex
(**A**): Oligodendrocitic process (Odp) in TEM image at 11,5 k magnification with and adjacent myelin sheath (Ms) of an axon (AX). Borders between oligodendrocitic process forming the myelin sheath (Ms) are blurred (▼). Potential iron content can be seen within the oligodendrocyte process (►). (**B**): Colored Elastic image of the oligodendrocitic process at 19 k. (**C**): Iron M Elemental Map. (**D**) Particle analysis of inverted elemental map of the colored region. A % area of transition metal content of *,203* was detected.

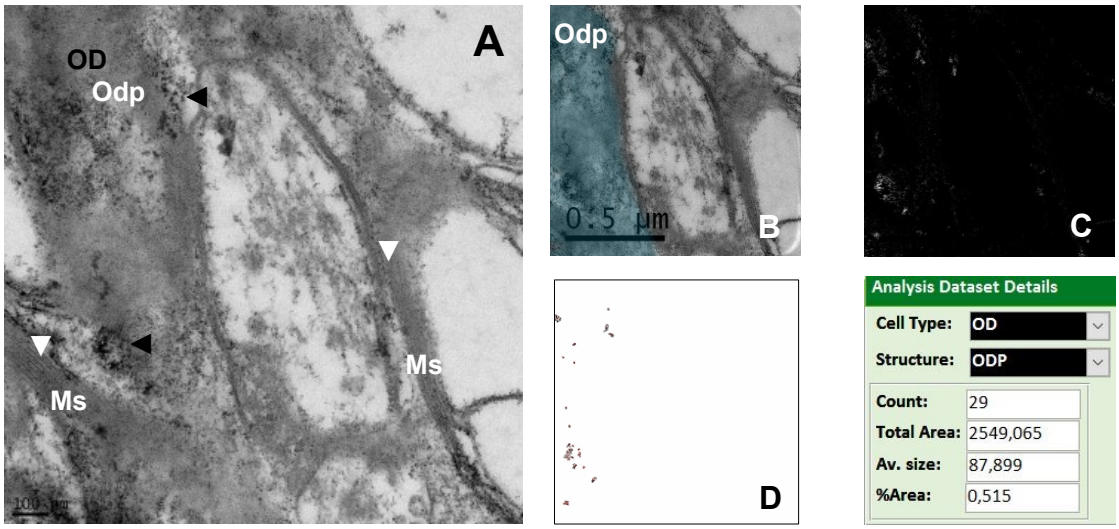

Figure 64: Oligodendrotic Process in the Globus Pallidus
(**A**): Oligodendrocitic process (Odp) from an oligodendrocyte (OD) in TEM at 14,5 k magnification. The formation of myelin sheaths (Ms) by the oligodendrocitic process is marked (▼). Presumed iron content is visible in parts of the oligodendrocyte process (◄). (**B**): Elastic image with left part of oligodendrocitic process colored. (**C**): Iron M Elemental Map. (**D**) Inverted elemental map particle analysis of the marked oligodendrocitic process. Particle analysis reveals a % area of transition metal content of *,515*.

5.3.6 Various Cell Structures

5.3.6.1 Mitochondria

Mitochondria (*N=64*) were found and analyzed within 4 brain regions, of which 18 could be contributed to axons, 23 to dendrites, 7 to oligodendrocytes and 10 to astrocytes (***Table 36***). 6 were categorized as having an undefinable underlying cell type. Most mitochondrial structures were identified in the putamen (***Table 35***).

Table 35: Mitochondria Frequencies per Brain Area

		Frequency	Percent
Valid	frontal cortex	8	12,5
	frontal white matter	3	4,7
	globus pallidus	17	26,6
	putamen	36	56,3
	Total	64	100,0

Table 36: Mitochondria Frequencies per Cell Type

		Frequency	Percent
Valid	astrocyte	10	15,6
	axon	18	28,1
	dendrite	23	35,9
	oligodendrocyte	7	10,9
	undefinable	6	9,4
	Total	64	100,0

Table 37: % Area of Transition Metal Content in Mitochondria

Descriptive Statistics

celltypes	brainarea		N	Min.	Max.	Mean	SD
astrocyte	frontal white matter	**%Area**	**1**	**,037**	**,037**	**,03700**	**.**
		Valid N (listwise)	1				
	globus pallidus	**%Area**	**1**	**,073**	**,073**	**,07300**	**.**
		Valid N (listwise)	1				
	putamen	**%Area**	**8**	**,000**	**,115**	**,01550**	**,040327**
		Valid N (listwise)	8				
axon	frontal cortex	**%Area**	**1**	**,000**	**,000**	**,00000**	**.**
		Valid N (listwise)	1				
	frontal white matter	**%Area**	**1**	**,000**	**,000**	**,00000**	**.**
		Valid N (listwise)	1				
	globus pallidus	**%Area**	**11**	**,000**	**,006**	**,00055**	**,001809**
		Valid N (listwise)	11				
	putamen	**%Area**	**5**	**,000**	**,827**	**,16540**	**,369846**
		Valid N (listwise)	5				
dendrite	frontal cortex	**%Area**	**3**	**,000**	**,059**	**,01967**	**,034064**
		Valid N (listwise)	3				
	globus pallidus		**4**	**,000**	**,080**	**,03525**	**,041436**
		Valid N (listwise)	4				
	putamen	**%Area**	**16**	**,000**	**,173**	**,02394**	**,048894**
		Valid N (listwise)	16				
oligodendrocyte	frontal cortex	**%Area**	**3**	**,000**	**,000**	**,00000**	**,000000**
		Valid N (listwise)	3				
	putamen	**%Area**	**4**	**,000**	**,000**	**,00000**	**,000000**
		Valid N (listwise)	4				
undefinable	frontal cortex	**%Area**	**1**	**,015**	**,015**	**,01500**	**.**
		Valid N (listwise)	1				
	frontal white matter	**%Area**	**1**	**,000**	**,000**	**,00000**	**.**
		Valid N (listwise)	1				
	globus pallidus	**%Area**	**1**	**,127**	**,127**	**,12700**	**.**
		Valid N (listwise)	1				
	putamen	**%Area**	**3**	**,000**	**,195**	**,06500**	**,112583**
		Valid N (listwise)	3				

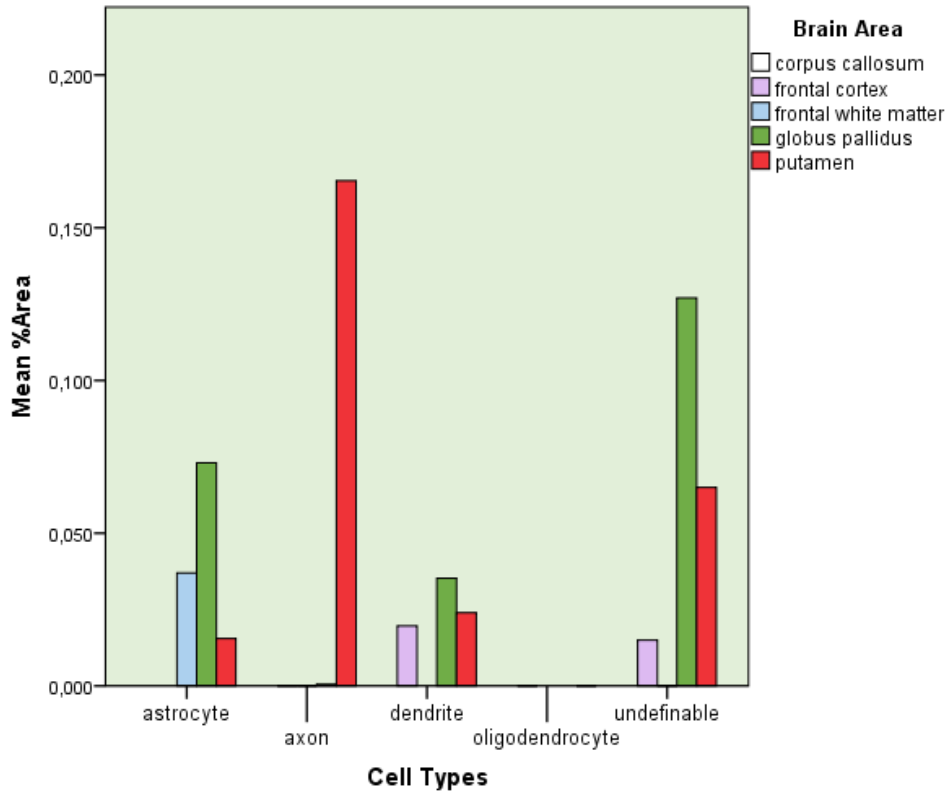

Figure 65: Bar Graph of % Area per Cell Type and Brain Area in Mitochondria
Highest % area of mitochondrial transition metal content was found in an axon in the putamen (*Max.=,827*). 3 mitochondria which were observed in proposed oligodendrocitic processes showed no transition metal content (*Max.=,000)*.

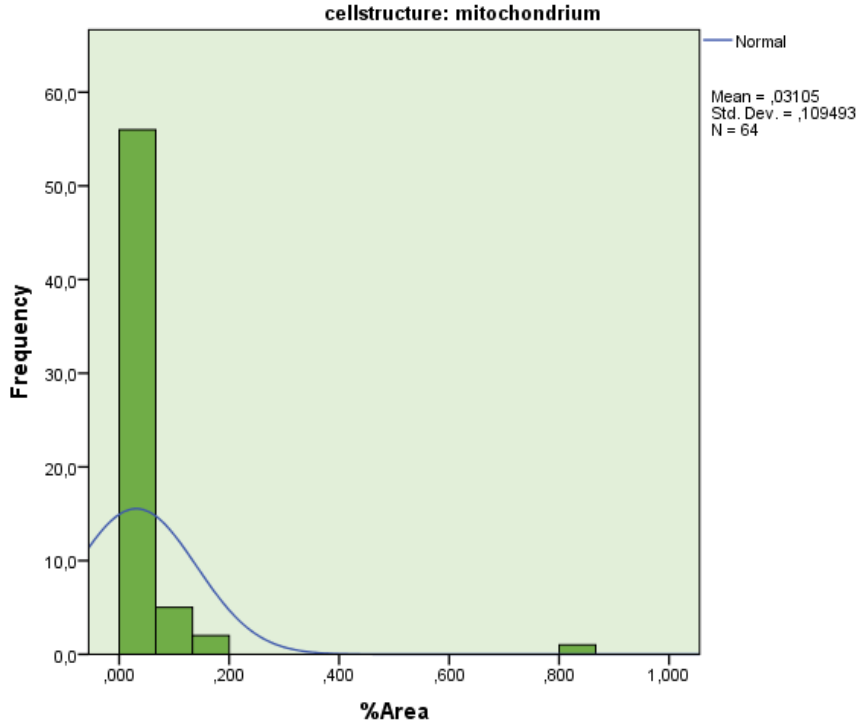

Figure 66: Histogram of % Area Frequencies of Mitochondria

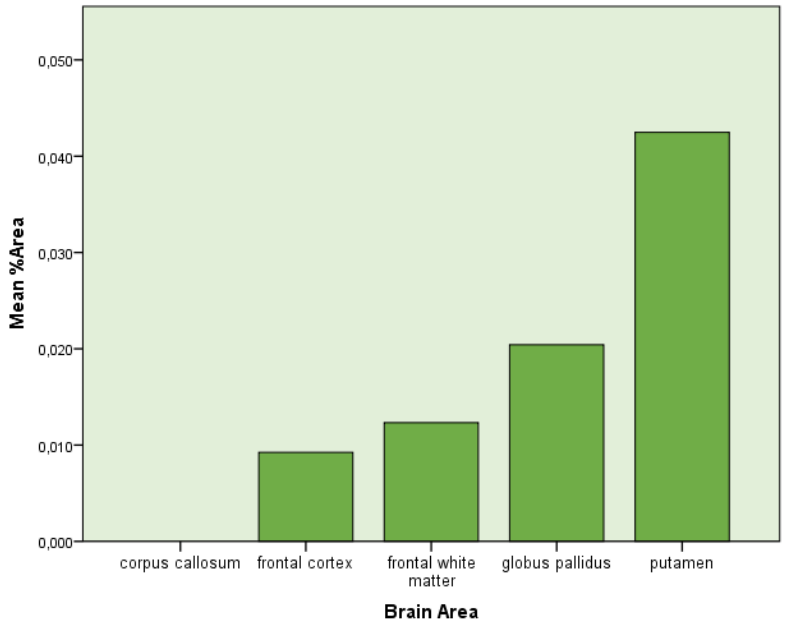

Figure 67: Bar Graph of Mean % Area of Mitochondria per Brain Area

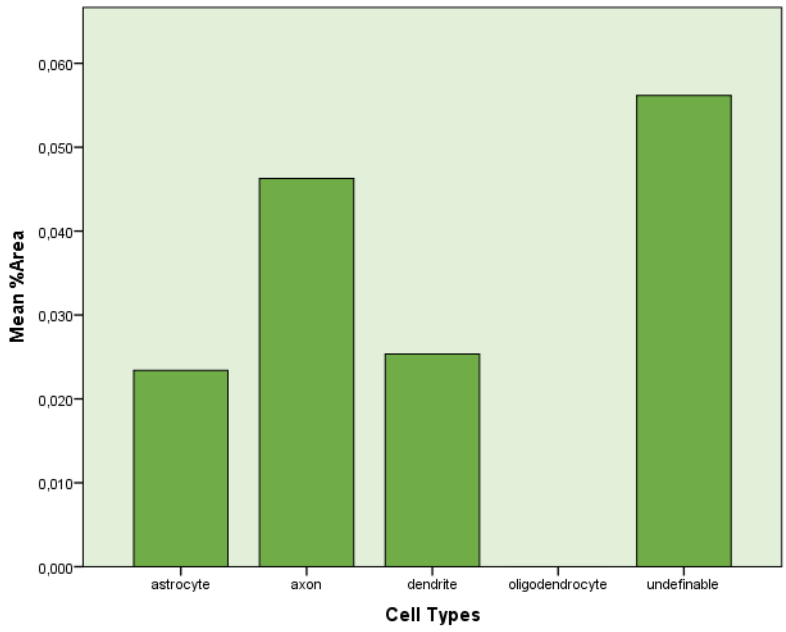

Figure 68: Bar Graph of Mean % Area of Mitochondria per Cell Type

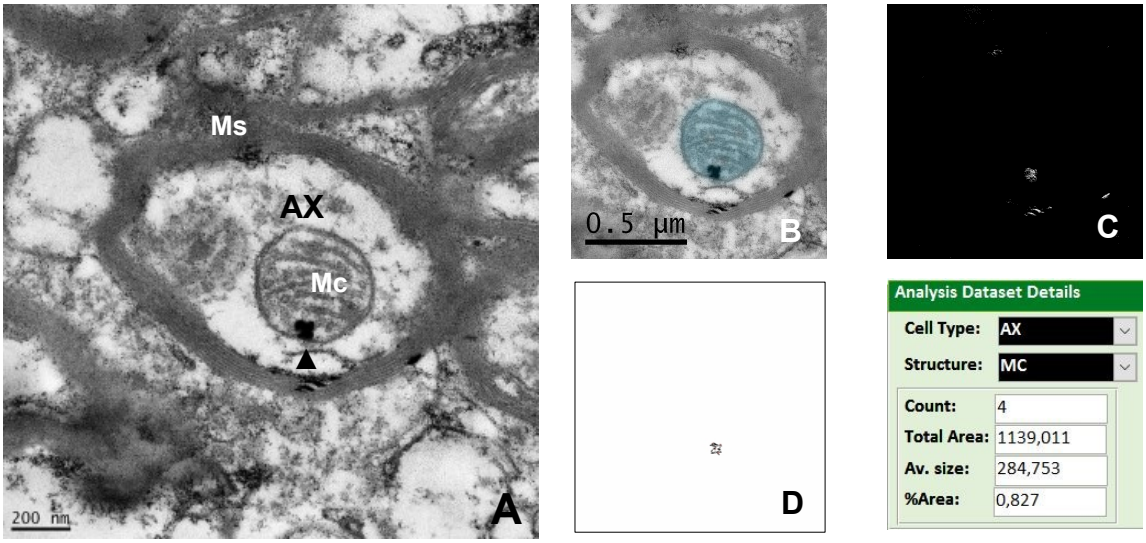

Figure 69: Axonal Mitochondrium in Putamen
(**A**): Within the axon (AX) a transversally sectioned mitochondrion (Mc) with putative transition metal content can be seen (▲). The image was obtained at 11,5 k in TEM mode. Elastic image with colored area (**B**) / EFTEM Iron M Map (**C**) / Inverted EFTEM with particle analysis outcome of colored region of interest (**D**). Particle analysis data shows transition metal content of an percentage area of *,827* within the mitochondrion. The shown mitochondrion contains the highest % area found in all observed mitochondria.

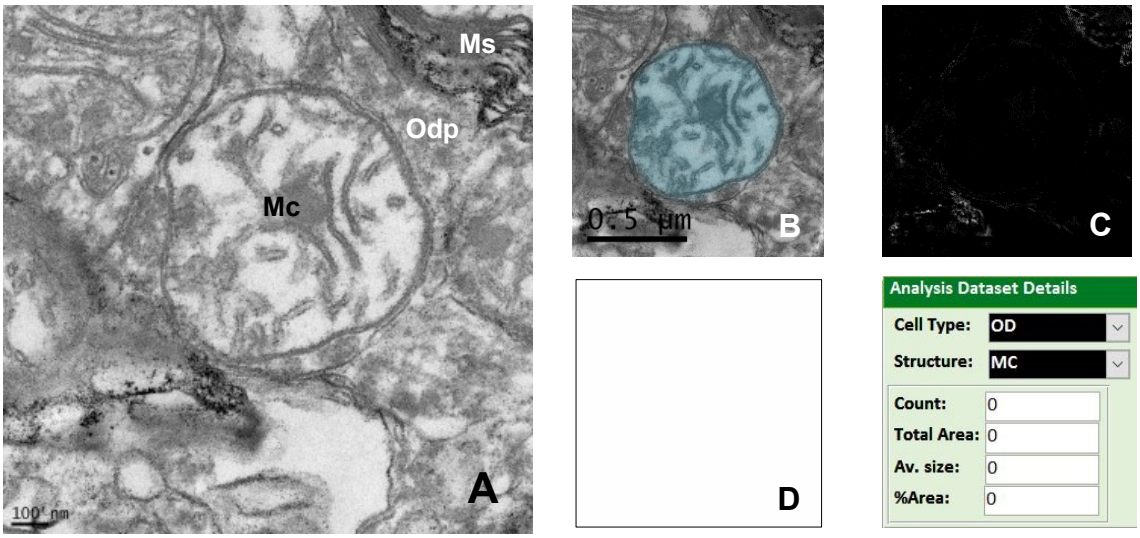

Figure 70: Mitochondrium in Oligodendrocitic Process in Frontal Cortex
(**A**): TEM image at 19 k suspects mitochondrium (Mc) in an oligodendrocitic process (Odp) due to dense cytoplasm and the proximity a myelin sheath (Ms). Arrow points to a putative intermembrane swelling visible in the mitochondrium. The mitochondrion appears swollen with a diameter of *713 nm*. (**B**): Elastic image of colored mitochondrion as region of interest. (**C**): Iron M Map of the whole region. (**D**): Inverted elemental map and corresponding particle analysis show no stainable content.

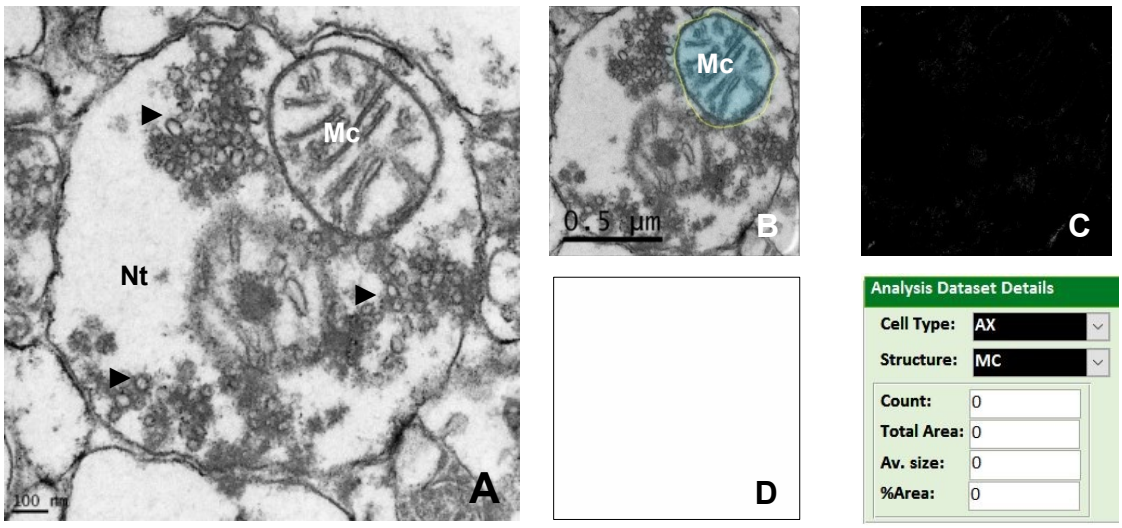

Figure 71: Mitochondrium in Nerve Terminal in the Putamen
(**A**): TEM image of axonal nerve terminal (Nt) with multiple vesicles visible (►). The mitochondrion (Mc) appears swollen with a diameter of *478,758 nm*. (**B**): Elastic image of the axon with mitochondrion colored and highlighted ROI within Fiji (yellow outlines) for particle analysis. (**C**) / (**D**): Iron M Maps of the whole region (original and inverted version after IrfanView processing) shows some diffusely distributed, small transition metal content. Next to it are the analysis details of the mitochondrium region of interest, where no transition metal content was detected.

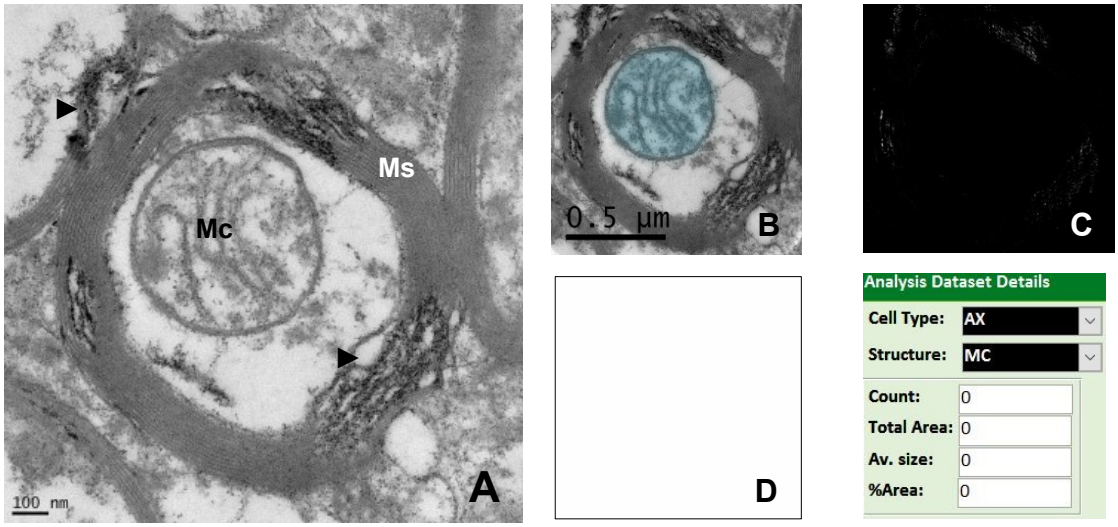

Figure 72: Mitochondrium in Axon in the Globus Pallidus
(**A**): TEM image of axoplasmatic mitochondrium (Mc) taken at 14,5 k magnification. The surrounding myelin sheath shows disruptions interpreted as shearing defects (**B**): Elastic image of colored mitochondrial region (**C**): Iron M Map of the total image region. (**D**): Inverted version of elemental map with selected mitochondrium. Analysis details revealed no transition metal content.

5.3.6.2 Lipofuscin Granules

A total of 10 structures were categorized as lipofuscin granules within the datasets (***Table 38***). Accumulations of lipofuscin granules, which are considered cytotoxic compounds, were only found in the globus pallidus, the putamen and the frontal white matter.

Table 38: Lipofuscin Granules Frequencies per Brain Area

		Frequency	Percent
Valid	frontal white matter	2	20,0
	globus pallidus	6	60,0
	putamen	2	20,0
	Total	10	100,0

Table 39: % Area of Transition Metal Content in Lipofuscin Granules

Descriptive Statistics

celltypes	cellstructure	brainarea		N	Min.	Max.	Mean	SD
astrocyte	lipofuscin granules	frontal white matter	**%Area**	**2**	**,009**	**12,121**	**6,06500**	**8,564477**
			Valid N (listwise)	2				
		globus pallidus	**%Area**	**6**	**,148**	**2,462**	**1,41200**	**,947748**
			Valid N (listwise)	6				
		putamen	**%Area**	**2**	**,008**	**4,562**	**2,28500**	**3,220164**
			Valid N (listwise)	2				

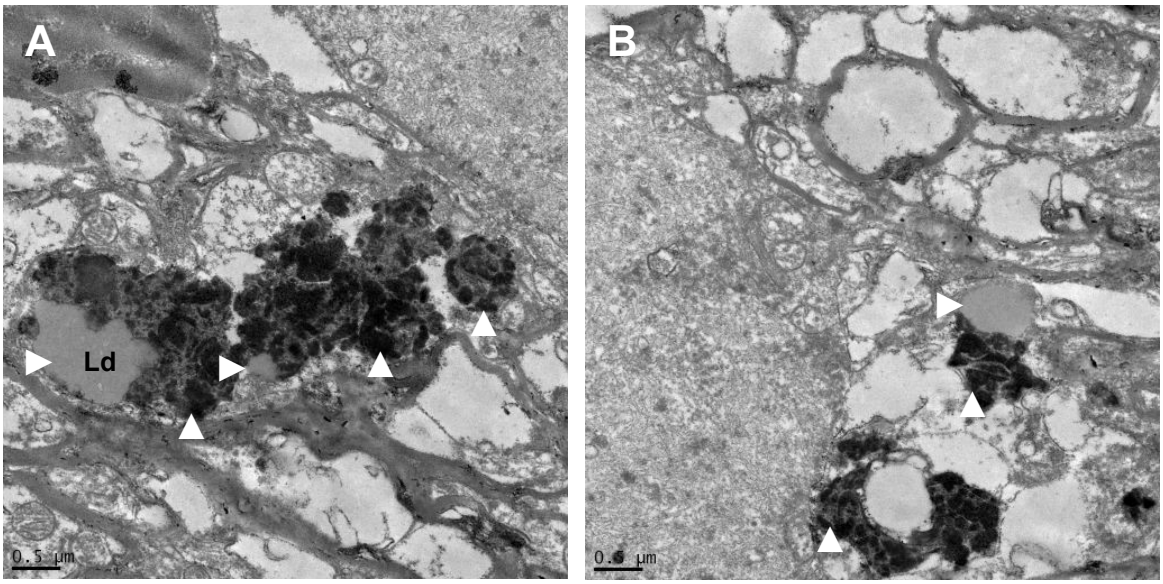

Figure 73: Overview of Lipofuscin granules in Putamen
(A)+**(B)**: Various lipofuscin granules (▲) can be seen on the overview TEM images at 3,5 k magnification of a human putamen. In close proximity, lipid droplets (Ld) are visible (►).

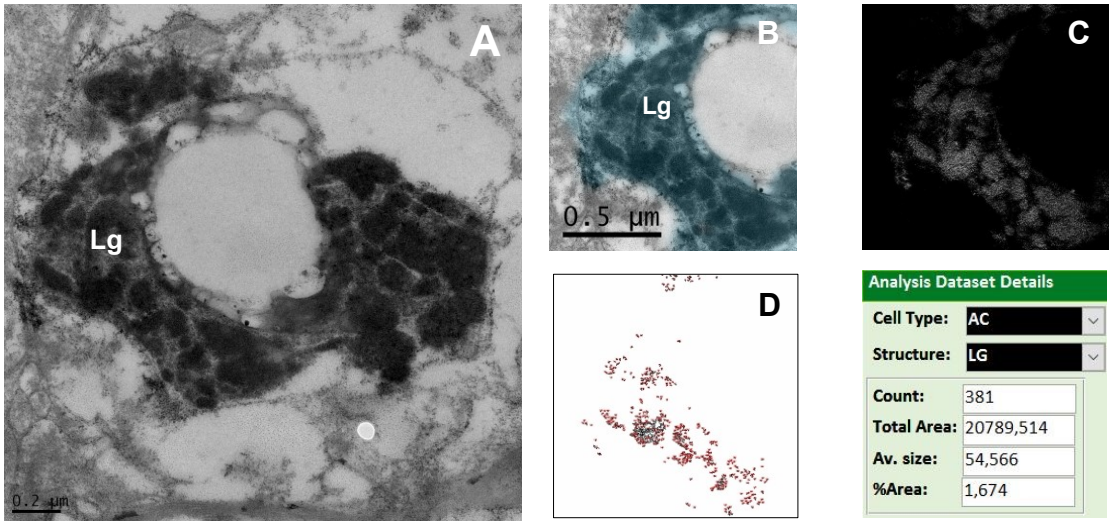

Figure 74: Lipofuscin Granule in Putamen
(**A**): A lipofuscin granule (Lg) in an astrocyte taken at 9,6 k magnification in TEM mode. (**B**): Elastic image with coloring of one of the lipofuscin granule. (**C**): Iron M elemental map of whole area. (**D**): Inverted elemental mapping and analysis of region show transition metal content within the lipofuscin inclusions of a % area of *1,674*.

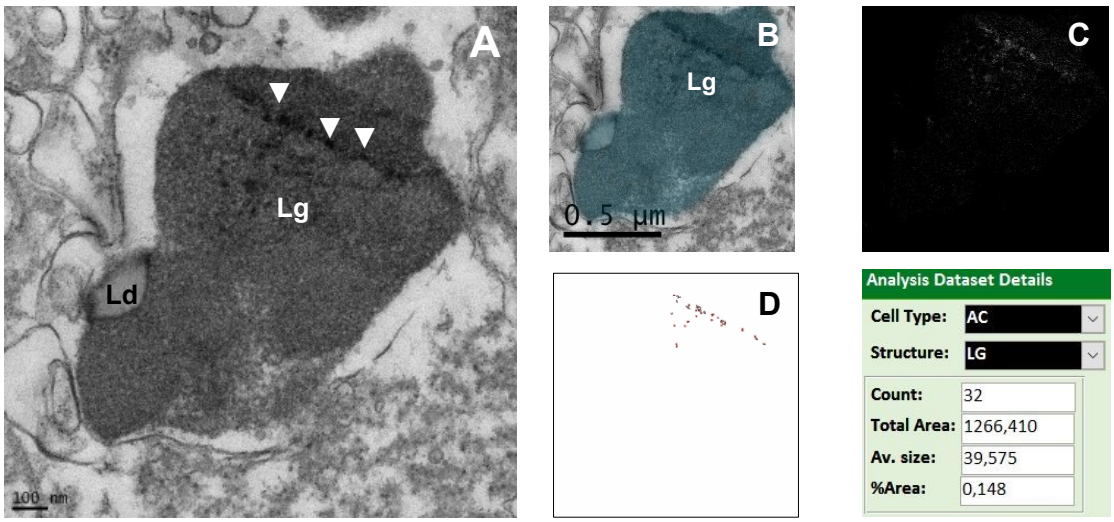

Figure 75: Lipofuscin Granule in Globus Pallidus
(**A**): A lipofuscin granule (Lg) with a lipid droplet (Ld) in an astrocyte taken at 14,5 k magnification in TEM mode. Several dark spots can be seen within the residual body (▼) (**B**): Elastic image with coloring of one of the lipofuscin granule. (**C**): Iron M elemental map of whole area. (**D**): Inverted elemental mapping and analysis of region show transition metal content within the lipofuscin inclusions of a % area of *,148*.

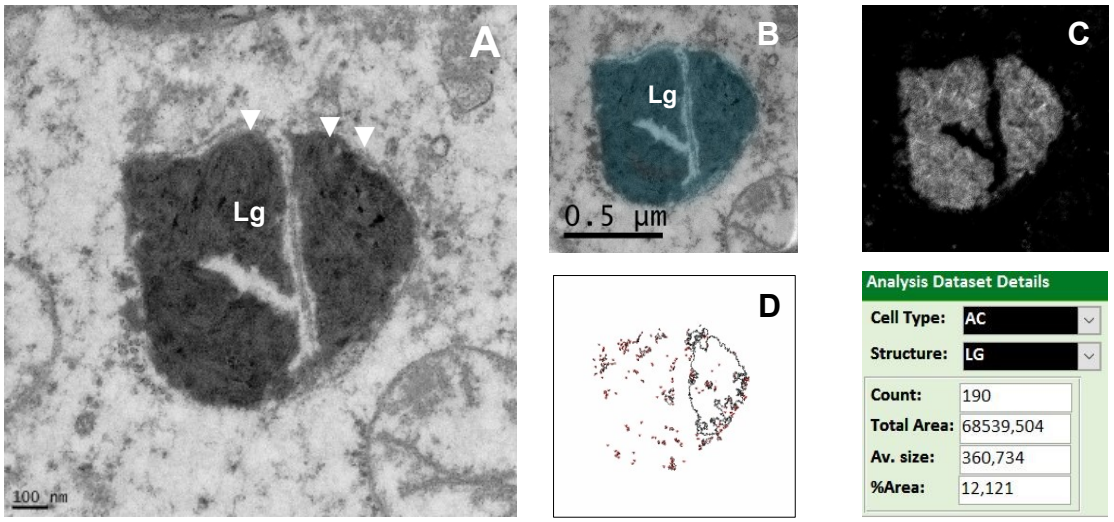

Figure 76: Lipofuscin Granule in Frontal White Matter
(**A**): TEM image taken at 14,5 k magnification of a lipofuscin granule (Lg) of an astrocyte (**B**): Elastic image with coloring of the lipofuscin granule. (**C**): Iron M elemental map of whole area. (**D**): Inverted elemental mapping and analysis of region shows highest transition metal content found within the lipofuscin granules with a % area of *12,121*.

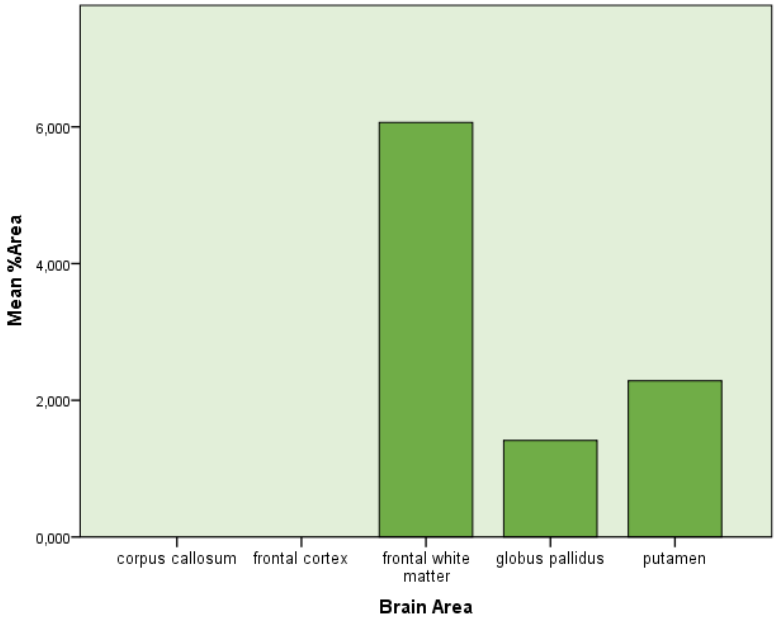

Figure 77: Bar Graph of Lipofuscin Granules per Brain Area

The frontal white matter showed by far the highest transition metal content within lipofuscin granules (*Max=12,121*), but with limited reliability due to the smale sample size (*n=2*).

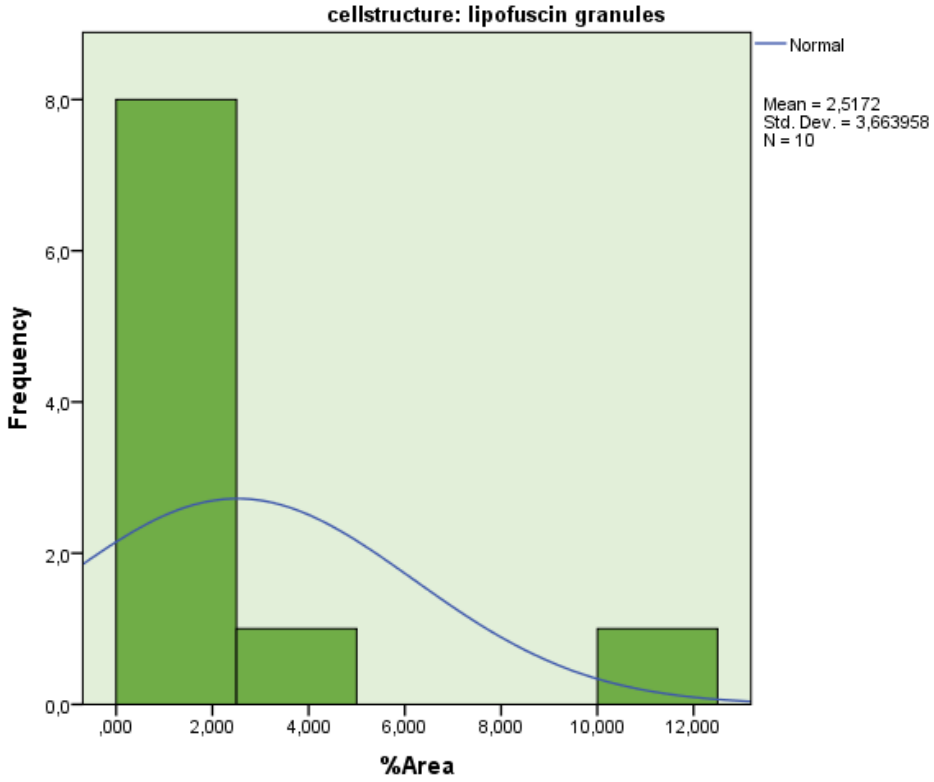

Figure 78: Histogram of % Area Frequencies of Lipofuscin Granules

5.3.6.3 Lipid Droplets

Lipid droplets (*N=6*) were found in 3 brain areas (***Table 40***), whereby the majority of them were observed in close proximity to, or enclosed within, lipofuscin granules. All 6 were categorized as originating from within astrocytes and analyzed (***Table 41***).

Table 40: Lipid Droplet Frequencies per Brain Area

		Frequency	Percent
Valid	corpus callosum	1	16,7
	globus pallidus	2	33,3
	putamen	3	50,0
	Total	6	100,0

Table 41: % Area of Transition Metal Content in Lipid Droplets

Descriptive Statistics

celltypes	cellstructure	brainarea		N	Min.	Max.	Mean	SD
astrocyte	lipid droplet	corpus callosum	**%Area**	**1**	**,044**	**,044**	**,04400**	**.**
			Valid N (listwise)	1				
		globus pallidus	**%Area**	**2**	**,141**	**2,778**	**1,45950**	**1,864641**
			Valid N (listwise)	2				
		putamen	**%Area**	**3**	**,000**	**,239**	**,13733**	**,123427**
			Valid N (listwise)	3				

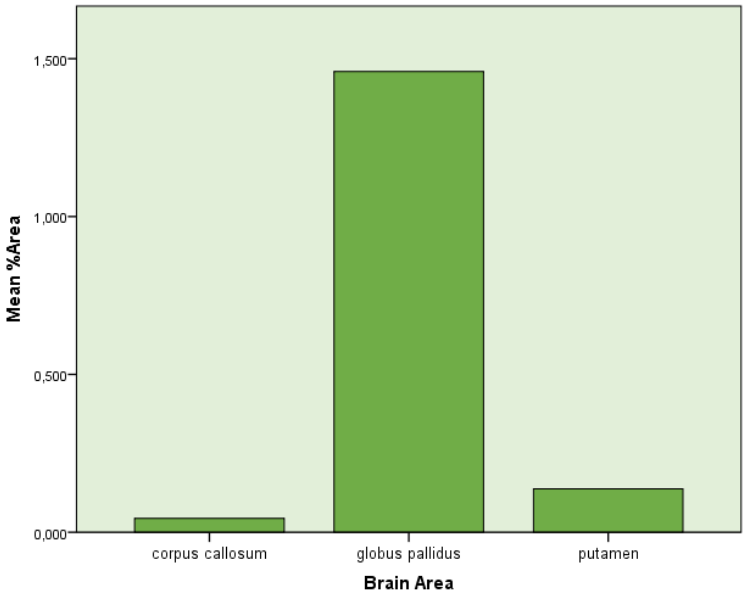

Figure 79: Bar Graph of Lipid Droplets per Brain Area

The highest % area of transition metal content by far was found in the globus pallidus (*Max.=,141; Mean=1,4595; SD=1,8646*), whereas no global assumptions can be made due to small sample size (*n=2*)

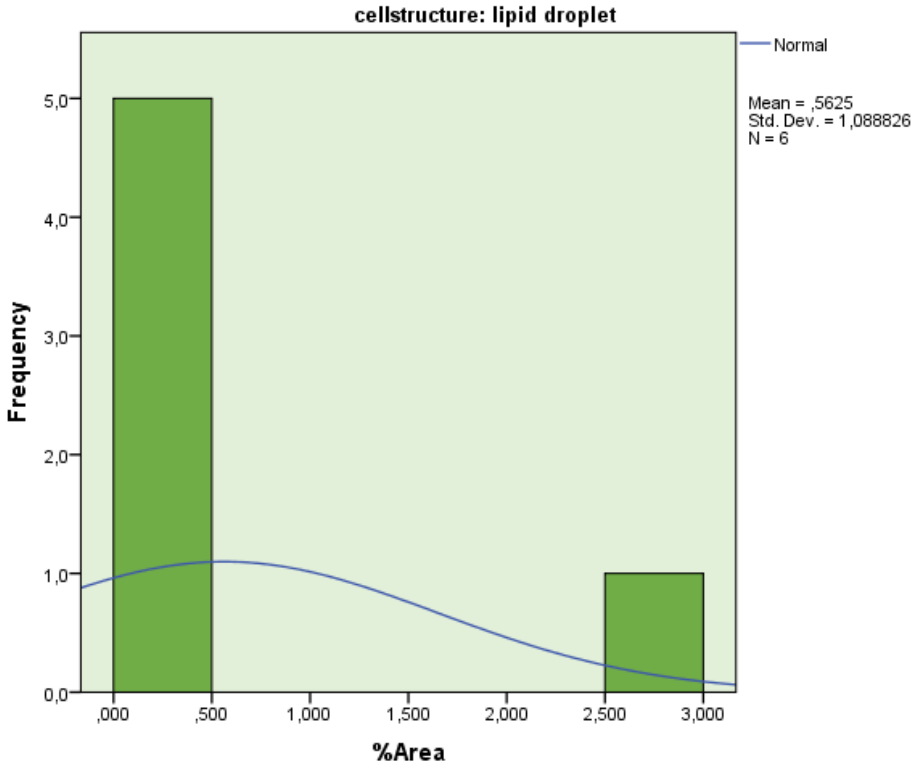

Figure 80: Histogram of % Area Frequencies of Lipid Droplets

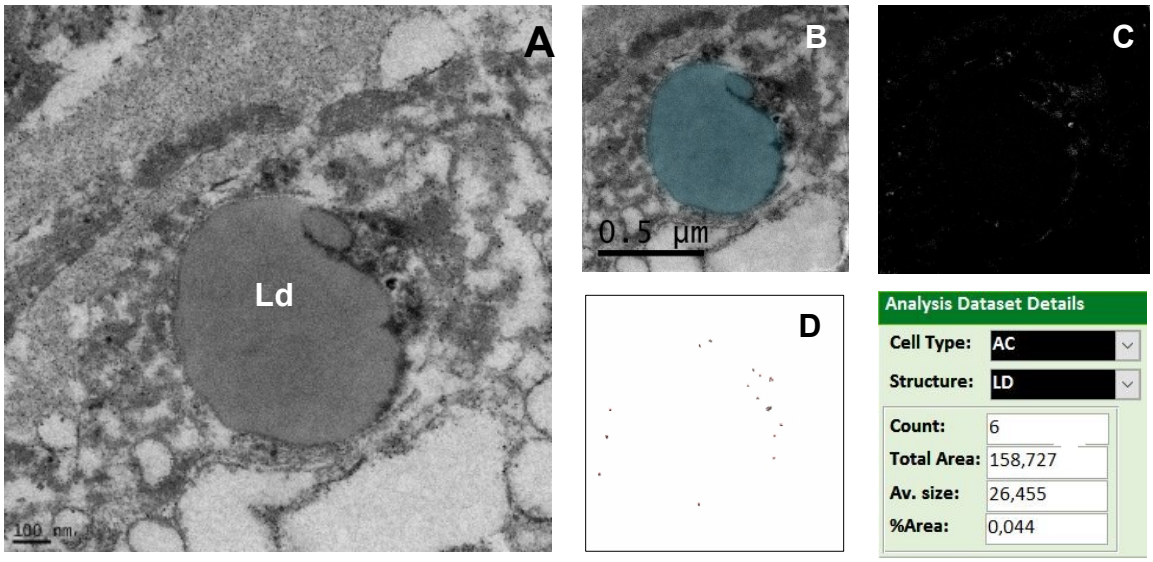

Figure 81: Lipid Droplet in Corpus Callosum
(**A**): A lipid droplet (Ld) within the corpus callosum, taken in TEM at 14,5 k. (**B**): Elastic image with coloring of the lipid droplet. (**C**): Iron M elemental map of whole area. (**D**): Inverted elemental mapping shows transition metal content of a % area of *,044*.

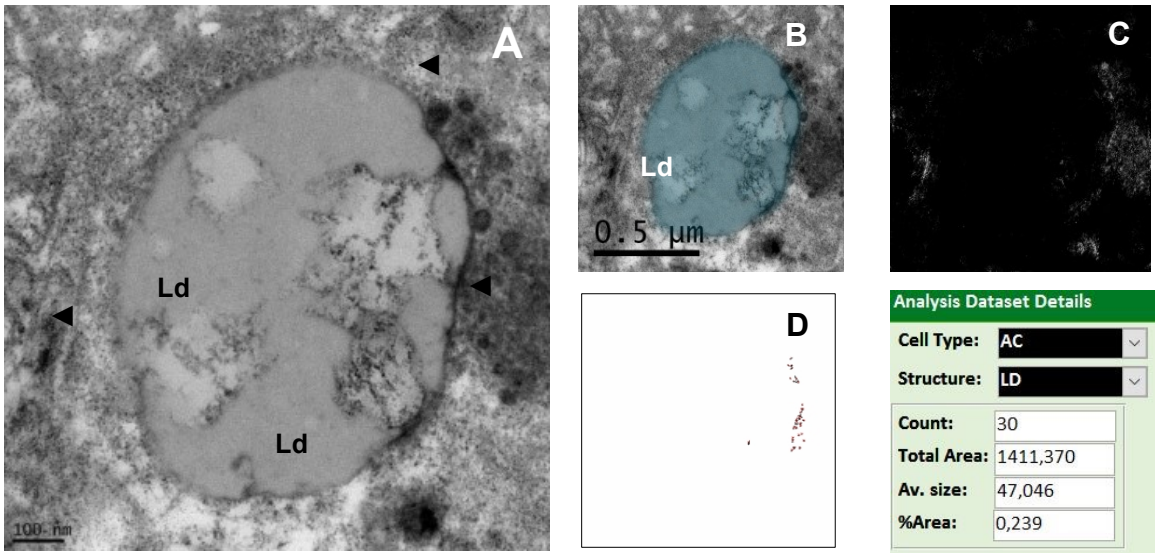

Figure 82: Lipid Droplets in Globus Pallidus
(**A**): A solitary lipid droplet (Ld) with several light inclusions in a TEM image taken at 14,5 k in a suspected astrocyte. (◄). (**B**): Elastic image with coloring of one of the lipid droplets. (**C**): Iron M elemental map of whole area. (**D**): Inverted elemental mapping shows transition metal content of a % area of *,141*.

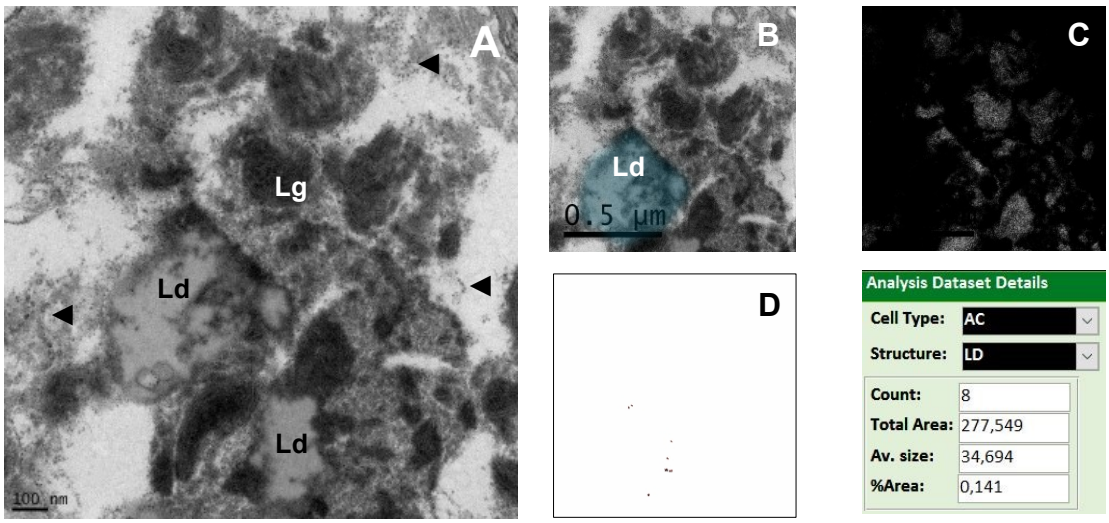

Figure 83: Lipid Droplets in Globus Pallidus
(**A**): Several lipofuscin granules (Lg) with two enclosed lipid droplets (Ld) in a TEM image taken at 14,5 k in the globus pallidus. The overlying cell type is an astrocyte, in which multiple glycogen particles can be seen (◄). (**B**): Elastic image with coloring of one of the lipid droplets. (**C**): Iron M elemental map of whole area. (**D**): Inverted elemental mapping shows transition metal content of a % area of *,141*.

5.3.6.4 Nucleus

1 Nucleus of an astrocyte was identified in a frontal white matter sample.

Table 42: % Area of Transition Metal Content in Nucleus

Descriptive Statistics

celltypes	cellstructure	brainarea		N	Min.	Max.	Mean	SD
astrocyte	nucleus	frontal white matter	%Area	1	10,361	10,361	10,36100	.
			Valid N (listwise)	1				

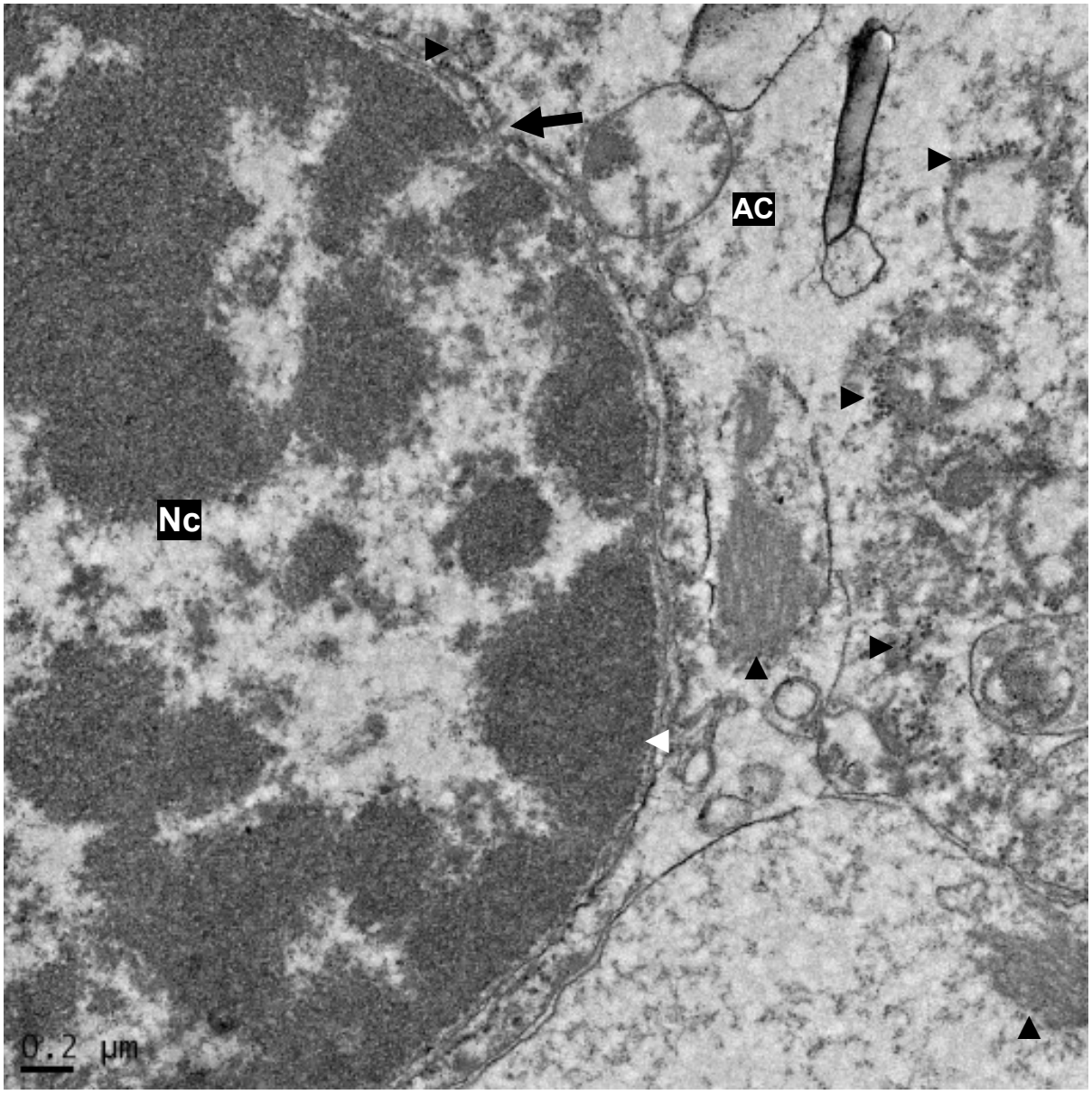

Figure 84: TEM Overview of Nucleus in Frontal White Matter
TEM image taken at 5 k of a nucleus (Nc) of an astrocyte (AC). Multiple gliafilaments (▲) and smooth endoplasmatic reticulum (►) are visible around the nucleus. One nuclear pore (←) can be seen In the upper part of the image. The heterochromatin (◄) presents itself as dark spots within the nucleus.

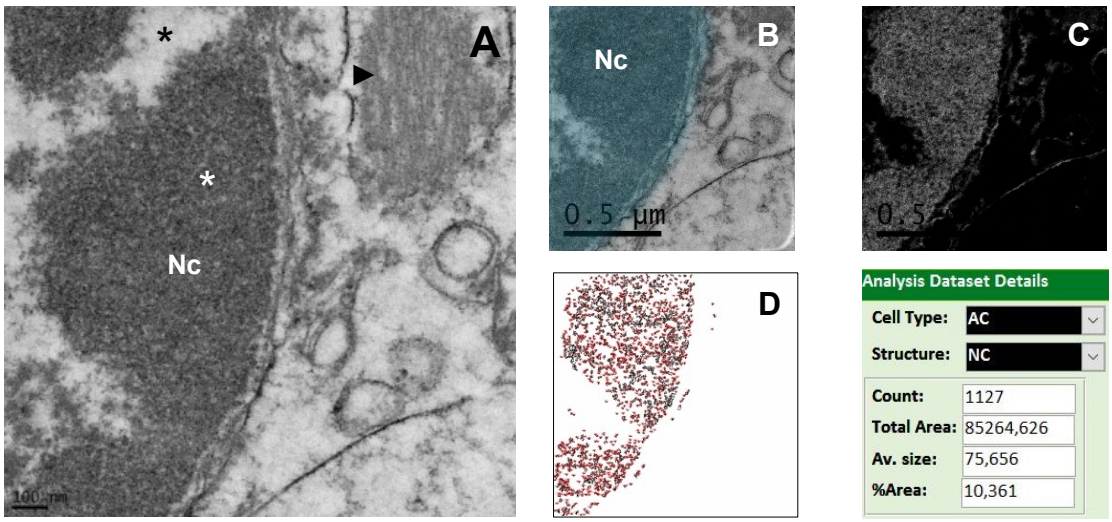

Figure 85: Nucleus in Frontal White Matter
(**A**): TEM image of the astrocyte nucleus (Nc) at 14,5 k magnification. The gliofilaments can be seen next to the nucleus section (►). Heterochromatin (*white* *) is present as dark spots in between the euchromatin (*black* *). (**B**): Elastic image with coloring of the nucleus. (**C**): Iron M elemental map of whole area. (**D**): Inverted elemental mapping shows diffuse abundant transition metal content of a % area of *10,361* mainly distributed within the heterochromatin.

5.3.6.5 Glycogen

1 glycogen inclusion was found in a presumed axon within a frontal white matter sample.

Table 43: % Area of Transition Metal Content in Glycogen

Descriptive Statistics

celltypes	cellstructure	brainarea		N	Min.	Max.	Mean	SD
axon	glycogen	frontal white matter	%Area	1	2,295	2,295	2,29500	.
			Valid N (listwise)	1				

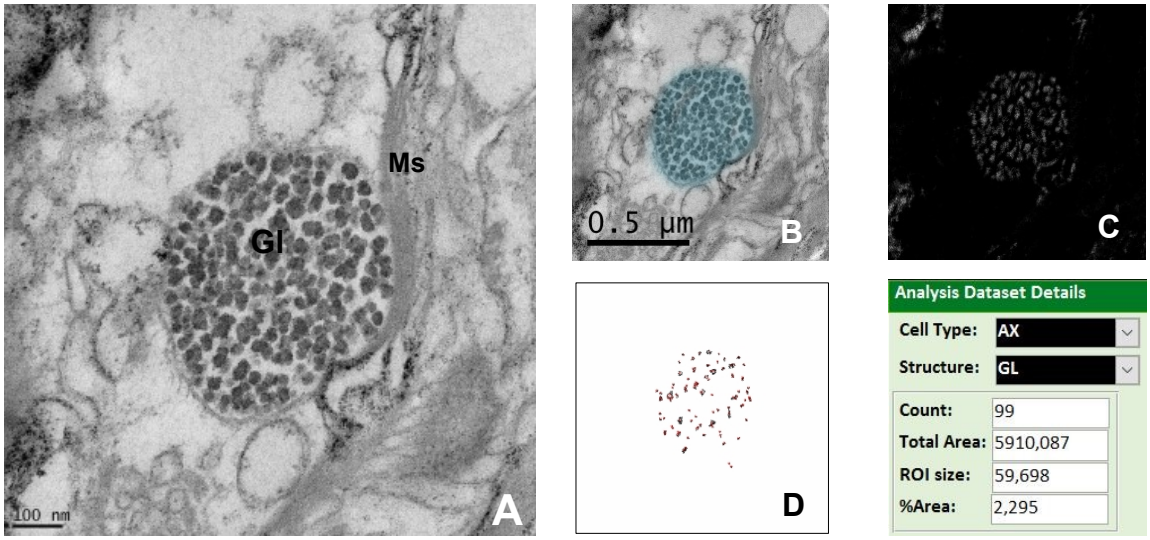

Figure 86: Glycogen in Frontal White Matter
(**A**): TEM image taken at 19 k of a glycogen body (Gl), presumably within an axon. The glycogen granules are bound to the adjacent myelin sheath (Ms). (**B**): Elastic image with coloring. (**C**): EFTEM Iron M Map. (**D**): Inverted EFTEM with particle analysis outcome of colored region of interest. Particle analysis shows transition metal content of a percentage area of *2,295* for the stained glycogen inclusions.

5.4 Brain Regions

Images were acquired for 17 samples from a total of 5 brain regions. As the analysis of cell types and cell structures of the sample images according to their brain areas were presented in the previous section, the present chapter will focus on the re-alignment of the sample datasets to compare the different brain regions according to their structure.

Table 44: Frequencies of Image Datasets of Brain Areas

		Frequency	Percent
Valid	corpus callosum	79	9,3
	frontal cortex	61	7,2
	frontal white matter	68	8,0
	globus pallidus	355	42,0
	putamen	283	33,5
	Total	846	100,0

5.4.1 Basal Ganglia

5.4.1.1 Globus pallidus

Number of brains:	**N=3**
Number of Specimens per Brain:	**1 / 2 / 2**
Total Number of Specimens:	**5**

Table 45: Frequencies of Cell Types in Globus Pallidus

		Frequency	Percent
Valid	astrocyte	45	12,7
	axon	192	54,1
	dendrite	67	18,9
	oligodendrocyte	50	14,1
	undefinable	1	,3
	Total	355	100,0

Table 46: Frequencies of Cell Structures in Globus Pallidus

		Frequency	Percent
Valid	axoplasm	29	8,2
	astrocytic process	36	10,1
	Dendritic Spines	63	17,7
	lipid droplet	2	,6
	lipofuscin granules	6	1,7
	mitochondrium	17	4,8
	myelin sheath	67	18,9
	nerve terminal	26	7,3
	oligodendrocitic process	50	14,1
	whole neurite	59	16,6
	Total	355	100,0

Table 47: % Area of Cell Structures in Globus Pallidus

Descriptive Statistics

celltypes	cellstructure		N	Min.	Max.	Mean	SD
astrocyte	astrocytic process	**%Area**	**36**	**,000**	**4,051**	**,24800**	**,723556**
		Valid N (listwise)	36				
	lipid droplet	**%Area**	**2**	**,141**	**2,778**	**1,45950**	**1,864641**
		Valid N (listwise)	2				
	lipofuscin granules	**%Area**	**6**	**,148**	**2,462**	**1,41200**	**,947748**
		Valid N (listwise)	6				
	mitochondrium	**%Area**	**1**	**,073**	**,073**	**,07300**	**.**
		Valid N (listwise)	1				
axon	axoplasm	**%Area**	**29**	**,000**	**1,666**	**,10341**	**,330540**
		Valid N (listwise)	29				
	mitochondrium	**%Area**	**11**	**,000**	**,006**	**,00055**	**,001809**
		Valid N (listwise)	11				
	myelin sheath	**%Area**	**67**	**,000**	**5,455**	**1,00263**	**1,306249**
		Valid N (listwise)	67				
	nerve terminal	**%Area**	**26**	**,000**	**1,625**	**,18050**	**,379283**
		Valid N (listwise)	26				
	whole neurite	**%Area**	**59**	**,000**	**3,860**	**,54564**	**,731924**
		Valid N (listwise)	59				
dendrite	Dendritic Spines	**%Area**	**63**	**,000**	**5,408**	**,28167**	**,787758**
		Valid N (listwise)	63				
	mitochondrium	**%Area**	**4**	**,000**	**,080**	**,03525**	**,041436**
		Valid N (listwise)	4				
Oligodendro-cyte	oligodendrocitic process	**%Area**	**50**	**,000**	**8,443**	**,66028**	**1,413389**
		Valid N (listwise)	50				
undefinable	mitochondrium	**%Area**	**1**	**,127**	**,127**	**,12700**	**.**
		Valid N (listwise)	1				

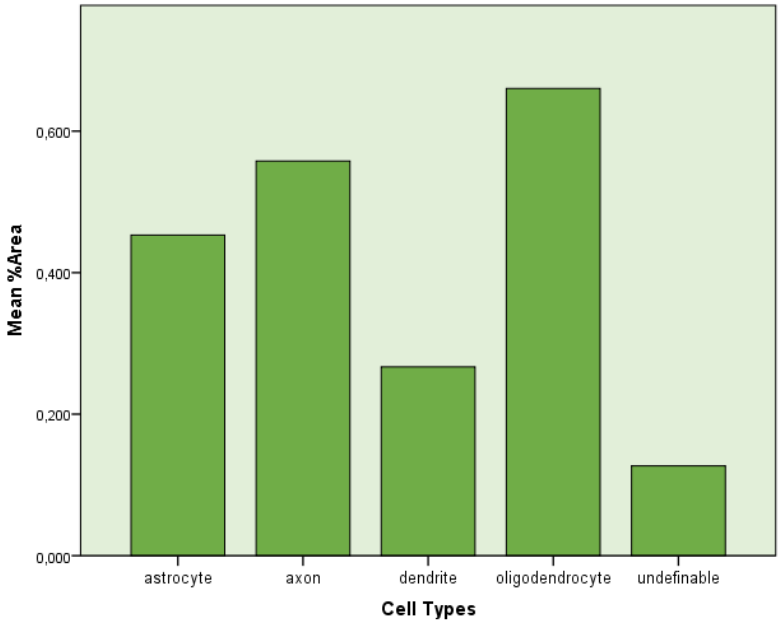

Figure 87: Bar Graph of Cell Types in Globus Pallidus
For cell types, oligodendrocytes contained the highest mean % area in transition metal content (*N=50; M=,66028; SD=1,4133*) within the globus pallidus, followed by axonal and astrocytic structures.

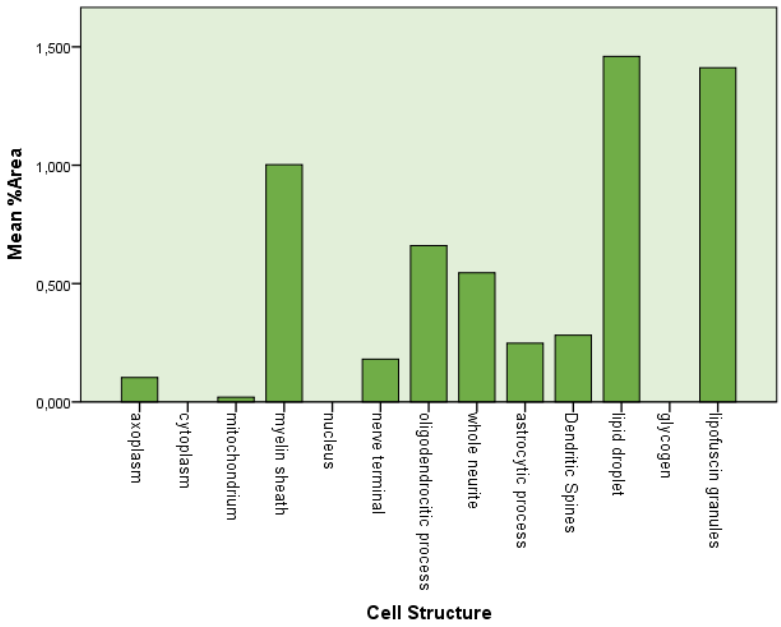

Figure 88: Bar Graph of Cell Structures in Globus Pallidus
In separated cell structures, the highest mean % area peak of transition metal content was observed in lipid droplets (*N=2; M=1,4595; SD=1,8646*), followed by lipofuscin granules and myelin sheaths. This observation might be linked to the lipid-binding characteristics of osmiumtetroxide and the spectral overlaps given by the utilization of the iron M peak in the feasibility study.

5.4.1.2 Putamen

Number of brains:	**N=2**
Number of Specimen per Brain:	**2 / 6**
Total Number of Specimens:	**8**

Table 48: Frequencies of Cell Types in Putamen

		Frequency	Percent
Valid	astrocyte	39	13,8
	axon	101	35,7
	dendrite	83	29,3
	oligodendrocyte	57	20,1
	undefinable	3	1,1
	Total	283	100,0

Table 49: Frequencies of Cell Structures in Putamen

		Frequency	Percent
Valid	axoplasm	13	4,6
	astrocytic process	26	9,2
	Dendritic Spines	67	23,7
	lipid droplet	3	1,1
	lipofuscin granules	2	,7
	mitochondrium	36	12,7
	myelin sheath	26	9,2
	nerve terminal	16	5,7
	oligodendrocitic process	53	18,7
	whole neurite	41	14,5
	Total	283	100,0

Table 50: % Area of Cell Structures in Putamen

Descriptive Statistics

celltypes	cellstructure		N	Min.	Max.	Mean	SD
astrocyte	astrocytic process	**%Area**	**26**	**,000**	**1,859**	**,22685**	**,422257**
		Valid N (listwise)	26				
	lipid droplet	**%Area**	**3**	**,000**	**,239**	**,13733**	**,123427**
		Valid N (listwise)	3				
	lipofuscin granules	**%Area**	**2**	**,008**	**4,562**	**2,28500**	**3,220164**
		Valid N (listwise)	2				
	mitochondrium	**%Area**	**8**	**,000**	**,115**	**,01550**	**,040327**
		Valid N (listwise)	8				
axon	axoplasm	**%Area**	**13**	**,000**	**,213**	**,02969**	**,062084**
		Valid N (listwise)	13				
	mitochondrium	**%Area**	**5**	**,000**	**,827**	**,16540**	**,369846**
		Valid N (listwise)	5				
	myelin sheath	**%Area**	**26**	**,000**	**2,226**	**,81323**	**,713948**
		Valid N (listwise)	26				
	nerve terminal	**%Area**	**16**	**,000**	**,198**	**,02231**	**,049562**
		Valid N (listwise)	16				
	whole neurite	**%Area**	**41**	**,000**	**1,973**	**,37171**	**,464061**
		Valid N (listwise)	41				
dendrite	dendritic spines	**%Area**	**67**	**,000**	**1,686**	**,15036**	**,295244**
		Valid N (listwise)	67				
	mitochondrium	**%Area**	**16**	**,000**	**,173**	**,02394**	**,048894**
		Valid N (listwise)	16				
oligodendro-cyte	mitochondrium	**%Area**	**4**	**,000**	**,000**	**,00000**	**,000000**
		Valid N (listwise)	4				
	oligodendrocitic process	**%Area**	**53**	**,000**	**4,714**	**,21387**	**,736086**
		Valid N (listwise)	53				
undefinable	mitochondrium	**%Area**	**3**	**,000**	**,195**	**,06500**	**,112583**
		Valid N (listwise)	3				

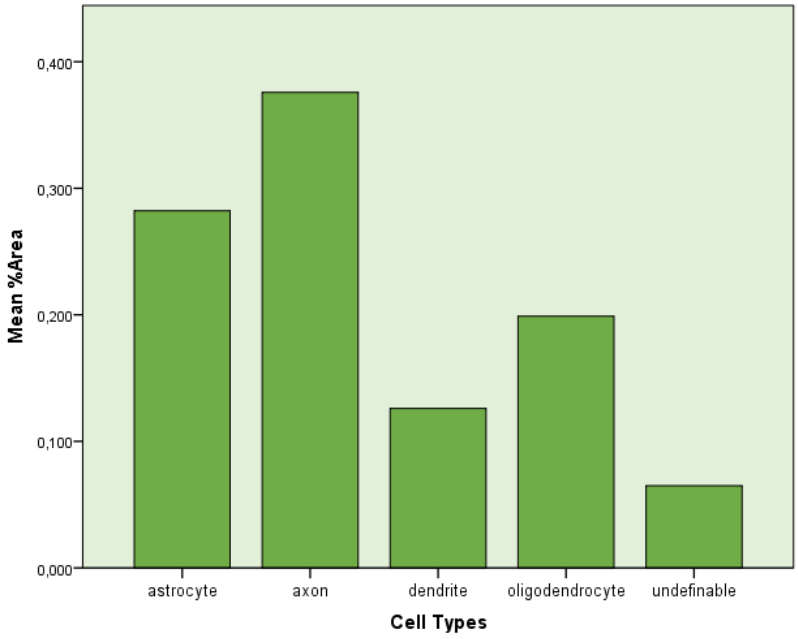

Figure 89: Bar Graph of % Area of Cell Types in Putamen
Axons (*N=101)* contained the highest % area of transition metal content in putamen brain samples, followed by astrocytes and oligodendrocytes.

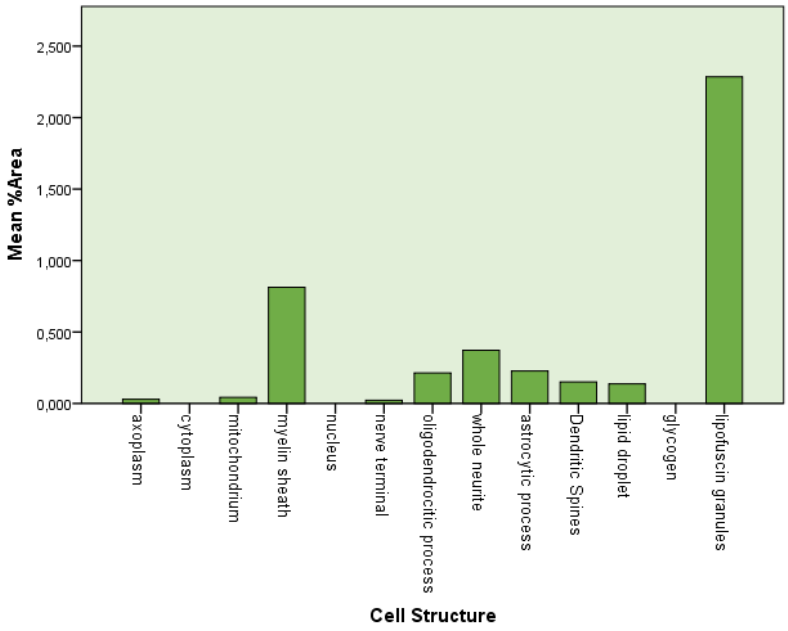

Figure 90: Bar Graph of % Area of Cell Structures in Putamen
Lipofuscin granules contained by far the highest transition metal content within putamen (N=2; M=2,2850; SD=3,2201), followed by myelin sheaths.

5.4.2 Corpus Callosum

Number of brains:	**N=1**
Number of Specimen per Brain:	**1**
Total Number of Specimen:	**1**

Table 51: Frequencies of Cell Types in Corpus Callosum

		Frequency	Percent
Valid	astrocyte	7	8,9
	axon	44	55,7
	dendrite	14	17,7
	oligodendrocyte	14	17,7
	Total	**79**	**100,0**

Table 52: Frequencies of Cell Structures in Corpus Callosum

		Frequency	Percent
Valid	axoplasm	8	10,1
	astrocytic process	6	7,6
	dendritic spines	14	17,7
	lipid droplet	1	1,3
	myelin sheath	19	24,1
	nerve terminal	1	1,3
	oligodendrocitic process	14	17,7
	whole neurite	16	20,3
	Total	**79**	**100,0**

Table 53: % Area of Cell Structures in Corpus Callosum

Descriptive Statistics

celltypes	cellstructure		N	Min.	Max.	Mean	SD
astrocyte	astrocytic process	**%Area**	**6**	**,000**	**,102**	**,02783**	**,043065**
		Valid N (listwise)	6				
	lipid droplet	**%Area**	**1**	**,044**	**,044**	**,04400**	**.**
		Valid N (listwise)	1				
axon	axoplasm	**%Area**	**8**	**,000**	**,311**	**,05612**	**,108836**
		Valid N (listwise)	8				
	myelin sheath	**%Area**	**19**	**,015**	**5,354**	**,81658**	**1,215195**
		Valid N (listwise)	19				
	nerve terminal	**%Area**	**1**	**,000**	**,000**	**,00000**	**.**
		Valid N (listwise)	1				
	whole neurite	**%Area**	**16**	**,046**	**,754**	**,21506**	**,198577**
		Valid N (listwise)	16				
dendrite	dendritic spines	**%Area**	**14**	**,000**	**,033**	**,00321**	**,009150**
		Valid N (listwise)	14				
Oligodendro-cyte	oligodendrocitic process	**%Area**	**14**	**,000**	**,675**	**,16293**	**,236546**
		Valid N (listwise)	14				

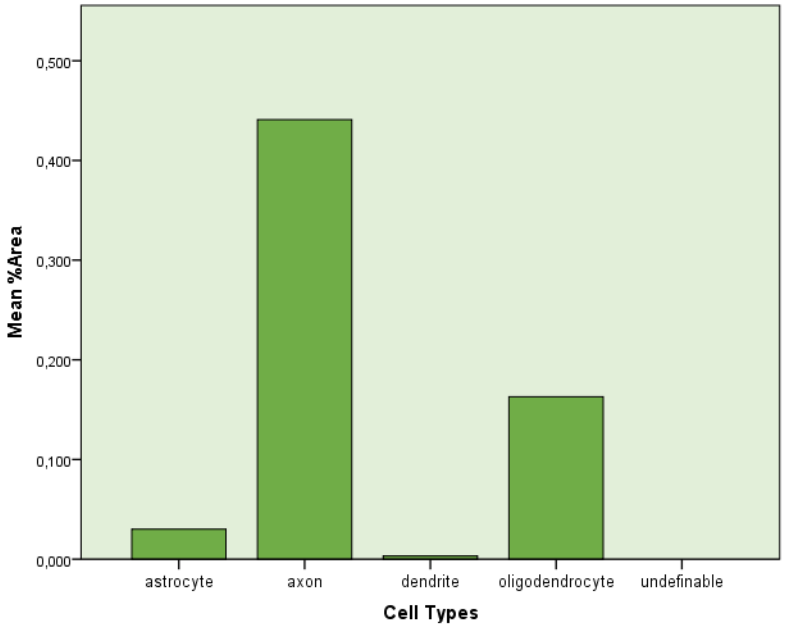

Figure 91: Bar Graph of % Area of Cell Types in Corpus Callosum

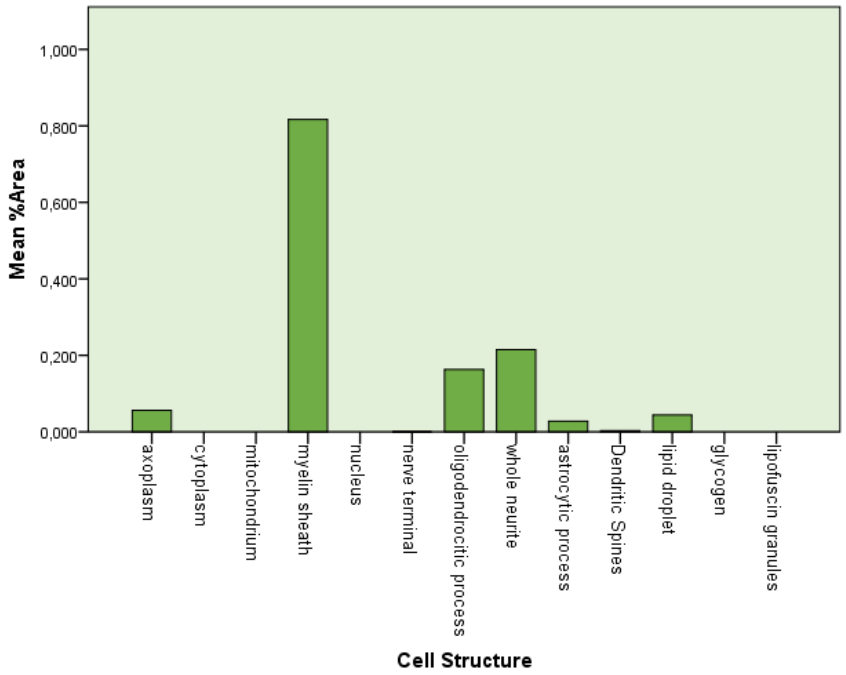

Figure 92: Bar Graph of % Area of Cell Structures in Corpus Callosum

Within the CC, the myelin sheath by far showed the most abundant transition metal content (*N=19, M=,81658*).

5.4.3 Frontal Cortex

Number of brains:	**N=1**
Number of Specimen per Brain:	**2**
Total Number of Specimen:	**2**

Table 54: Frequencies of Cell Types in Frontal Cortex

		Frequency	Percent
Valid	astrocyte	1	1,6
	axon	31	50,8
	dendrite	17	27,9
	oligodendrocyte	11	18,0
	undefinable	1	1,6
	Total	61	100,0

Table 55: Frequencies of Cell Structures in Frontal Cortex

		Frequency	Percent
Valid	axoplasm	4	6,6
	astrocytic process	1	1,6
	dendritic spines	14	23,0
	mitochondrium	8	13,1
	myelin sheath	6	9,8
	nerve terminal	8	13,1
	oligodendrocitic process	8	13,1
	whole neurite	12	19,7
	Total	61	100,0

Table 56: % Area of Cell Structures in Frontal Cortex

Descriptive Statistics

celltypes	cellstructure		N	Min.	Max.	Mean	SD
astrocyte	astrocytic process	**%Area**	**1**	**2,375**	**2,375**	**2,37500**	**.**
		Valid N (listwise)	1				
axon	axoplasm	**%Area**	**3**	**,000**	**,000**	**,00000**	**,000000**
		Valid N (listwise)	3				
	cytoplasm	**%Area**	**1**	**1,299**	**1,299**	**1,29900**	**.**
		Valid N (listwise)	1				
	mitochondrium	**%Area**	**1**	**,000**	**,000**	**,00000**	**.**
		Valid N (listwise)	1				
	myelin sheath	**%Area**	**6**	**,085**	**3,204**	**1,19600**	**1,469176**
		Valid N (listwise)	6				
	nerve terminal	**%Area**	**8**	**,000**	**1,966**	**,40613**	**,643406**
		Valid N (listwise)	8				
	whole neurite	**%Area**	**12**	**,098**	**,735**	**,34217**	**,194279**
		Valid N (listwise)	12				
dendrite	dendritic spines	**%Area**	**14**	**,000**	**1,203**	**,23250**	**,334194**
		Valid N (listwise)	14				
	mitochondrium	**%Area**	**3**	**,000**	**,059**	**,01967**	**,034064**
		Valid N (listwise)	3				
oligodendro-cyte	mitochondrium	**%Area**	**3**	**,000**	**,000**	**,00000**	**,000000**
		Valid N (listwise)	3				
	oligodendrocitic process	**%Area**	**8**	**,000**	**1,472**	**,33325**	**,487491**
		Valid N (listwise)	8				
undefinable	mitochondrium	**%Area**	**1**	**,015**	**,015**	**,01500**	**.**
		Valid N (listwise)	1				

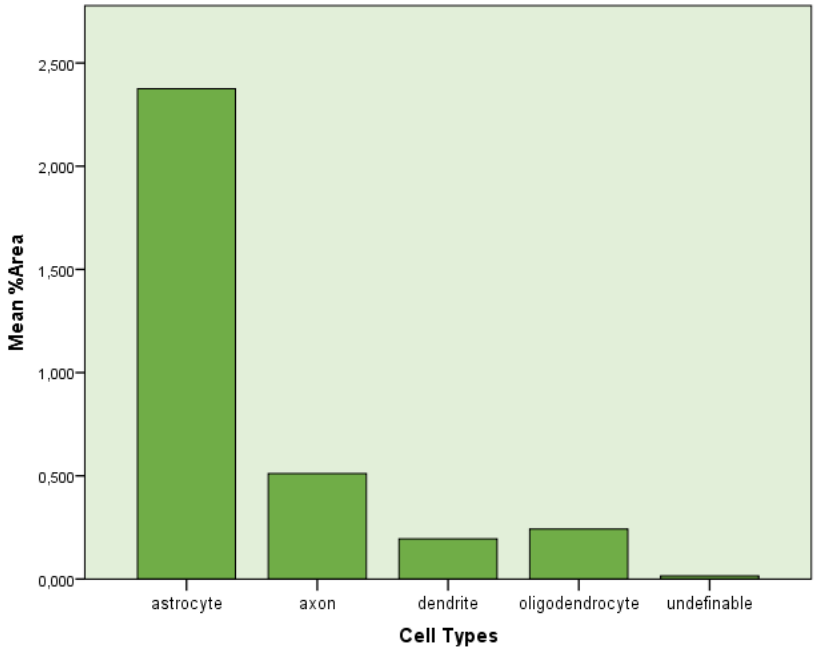

Figure 93: Bar Graph of % Area of Cell Types in Frontal Cortex

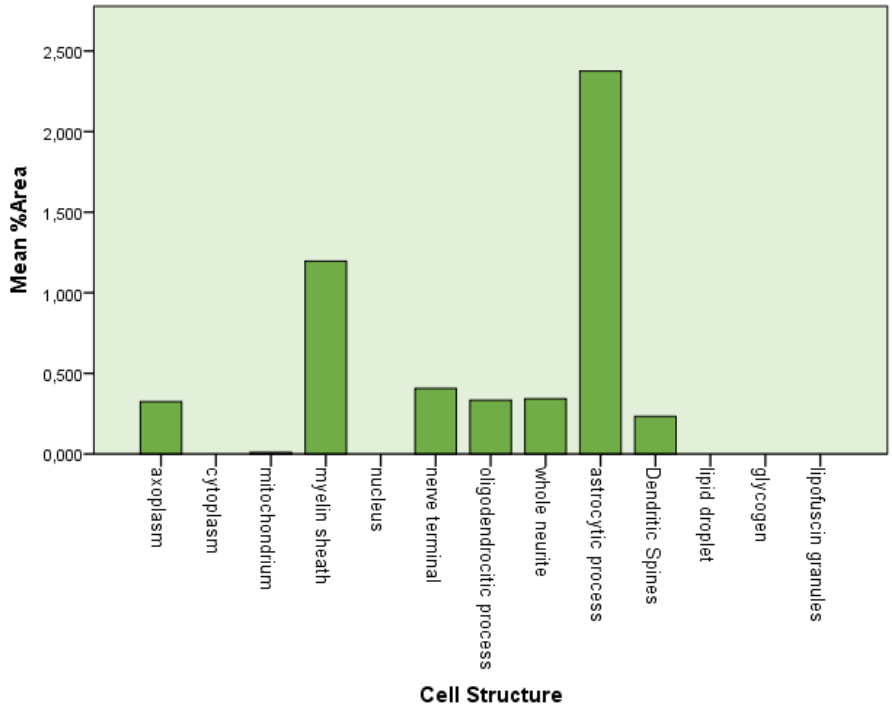

Figure 94: Bar Graph of % Area in Cell Structures in Frontal Cortex

Most abundant transition metal content in frontal cortex samples was found in a single astrocytic process (*N=1, M=2,3750*). As the sample size of the astrocyte was limited to 1 in the specific area, no predictions can be made.

5.4.4 Frontal White Matter

Number of brains:	N=1
Number of Specimen per Brain:	2
Total Number of Specimen:	2

Table 57: Frequencies of Cell Types in Frontal White Matter

		Frequency	Percent
Valid	astrocyte	8	11,8
	axon	43	63,2
	dendrite	7	10,3
	oligodendrocyte	9	13,2
	undefinable	1	1,5
	Total	68	100,0

Table 58: Frequencies of Cell Structures in Frontal White Matter

		Frequency	Percent
Valid	axoplasm	3	4,4
	astrocytic process	4	5,9
	Dendritic Spines	7	10,3
	glycogen	1	1,5
	lipofuscin granules	2	2,9
	mitochondrium	3	4,4
	myelin sheath	20	29,4
	nucleus	1	1,5
	nerve terminal	2	2,9
	oligodendrocitic process	9	13,2
	whole neurite	16	23,5
	Total	68	100,0

Table 59: % Area of Cell Structures in Frontal White Matter

Descriptive Statistics

celltypes	cellstructure		N	Min.	Max.	Mean	SD
astrocyte	astrocytic process	**%Area**	**4**	**,083**	**,302**	**,16025**	**,101700**
		Valid N (listwise)	4				
	lipofuscin granules	**%Area**	**2**	**,009**	**12,121**	**6,06500**	**8,564477**
		Valid N (listwise)	2				
	mitochondrium	**%Area**	**1**	**,037**	**,037**	**,03700**	**.**
		Valid N (listwise)	1				
	nucleus	**%Area**	**1**	**10,361**	**10,361**	**10,36100**	**.**
		Valid N (listwise)	1				
axon	axoplasm	**%Area**	**3**	**,000**	**,033**	**,01100**	**,019053**
		Valid N (listwise)	3				
	glycogen	**%Area**	**1**	**2,295**	**2,295**	**2,29500**	**.**
		Valid N (listwise)	1				
	mitochondrium	**%Area**	**1**	**,000**	**,000**	**,00000**	**.**
		Valid N (listwise)	1				
	myelin sheath	**%Area**	**20**	**,073**	**5,937**	**2,24595**	**2,025316**
		Valid N (listwise)	20				
	nerve terminal	**%Area**	**2**	**,000**	**,023**	**,01150**	**,016263**
		Valid N (listwise)	2				
	whole neurite	**%Area**	**16**	**,000**	**2,406**	**,88356**	**,769493**
		Valid N (listwise)	16				
dendrite	dendritic spines	**%Area**	**7**	**,000**	**,106**	**,03186**	**,042113**
		Valid N (listwise)	7				
oligodendro-cyte	oligodendrocitic process	**%Area**	**9**	**,000**	**5,278**	**1,67622**	**2,066763**
		Valid N (listwise)	9				
undefinable	mitochondrium	**%Area**	**1**	**,000**	**,000**	**,00000**	**.**
		Valid N (listwise)	1				

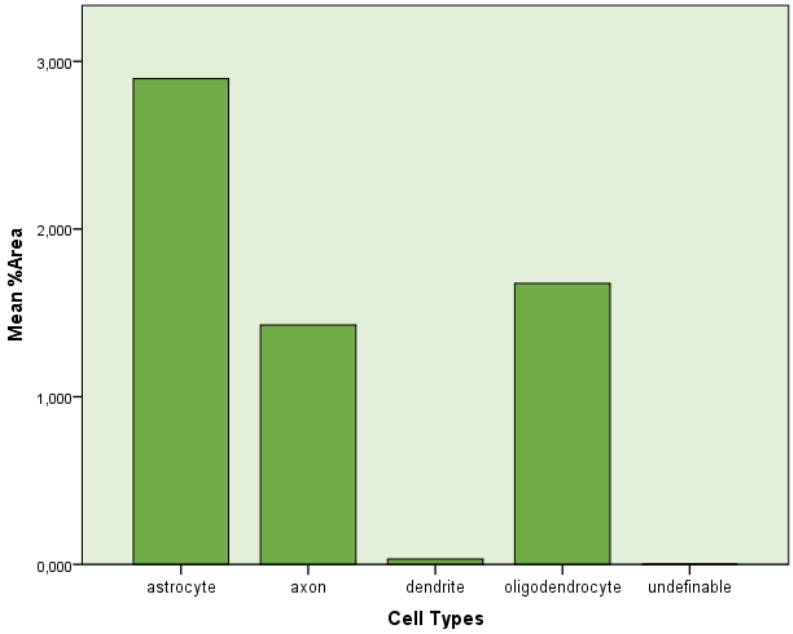

Figure 95: Bar Graph of % Area of Cell Types in Frontal White Matter

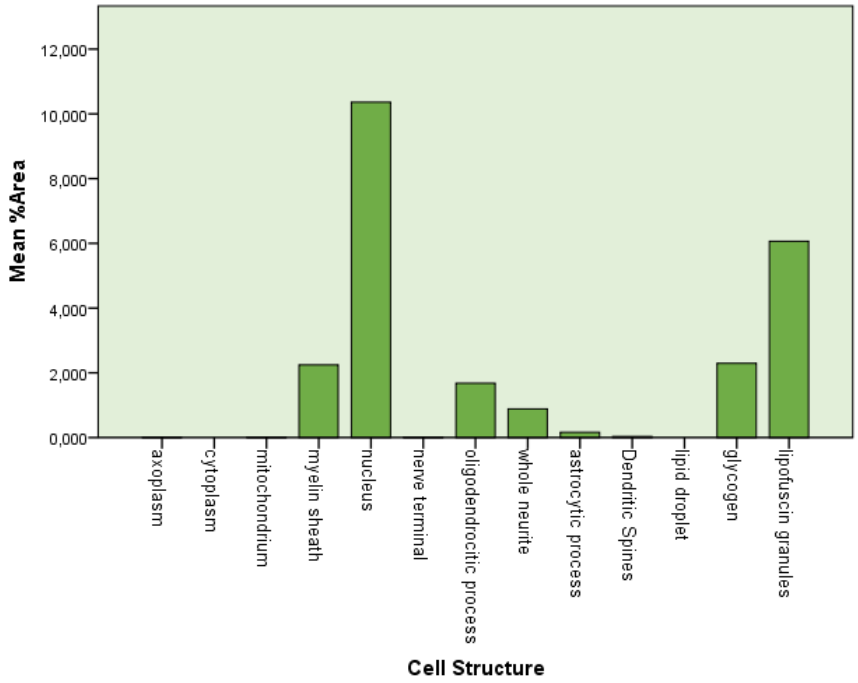

Figure 96: Bar Graph of % Area of Cell Structures in Frontal White Matter

5.4.5 Summary of Brain Regions

Table 60: Summary of % Area of all Cell Structures Observed

Descriptive Statistics

celltypes	cellstructure		N	Min.	Max.	Mean	SD
astrocyte	astrocytic process	**%Area**	**73**	**,000**	**4,051**	**,24670**	**,620022**
		Valid N (listwise)	73				
	lipid droplet	**%Area**	**6**	**,000**	**2,778**	**,56250**	**1,088826**
		Valid N (listwise)	6				
	lipofuscin granules	**%Area**	**10**	**,008**	**12,121**	**2,51720**	**3,663958**
		Valid N (listwise)	10				
	mitochondrium	**%Area**	**10**	**,000**	**,115**	**,02340**	**,040178**
		Valid N (listwise)	10				
	nucleus	**%Area**	**1**	**10,361**	**10,361**	**10,36100**	**.**
		Valid N (listwise)	1				
axon	axoplasm	**%Area**	**57**	**,000**	**1,666**	**,09063**	**,291408**
		Valid N (listwise)	57				
	glycogen	**%Area**	**1**	**2,295**	**2,295**	**2,29500**	**.**
		Valid N (listwise)	1				
	mitochondrium	**%Area**	**18**	**,000**	**,827**	**,04628**	**,194848**
		Valid N (listwise)	18				
	myelin sheath	**%Area**	**138**	**,000**	**5,937**	**1,12993**	**1,406872**
		Valid N (listwise)	138				
	nerve terminal	**%Area**	**53**	**,000**	**1,966**	**,15702**	**,377221**
		Valid N (listwise)	53				
	whole neurite	**%Area**	**144**	**,000**	**3,860**	**,47998**	**,616020**
		Valid N (listwise)	144				
dendrite	Dendritic Spines	**%Area**	**165**	**,000**	**5,408**	**,18995**	**,535423**
		Valid N (listwise)	165				
	mitochondrium	**%Area**	**23**	**,000**	**,173**	**,02535**	**,044646**
		Valid N (listwise)	23				
oligodendro-cyte	mitochondrium	**%Area**	**7**	**,000**	**,000**	**,00000**	**,000000**
		Valid N (listwise)	7				
	Oligodendrocitic process	**%Area**	**134**	**,000**	**8,443**	**,48046**	**1,171275**
		Valid N (listwise)	134				
undefinable	mitochondrium	**%Area**	**6**	**,000**	**,195**	**,05617**	**,084203**
		Valid N (listwise)	6				

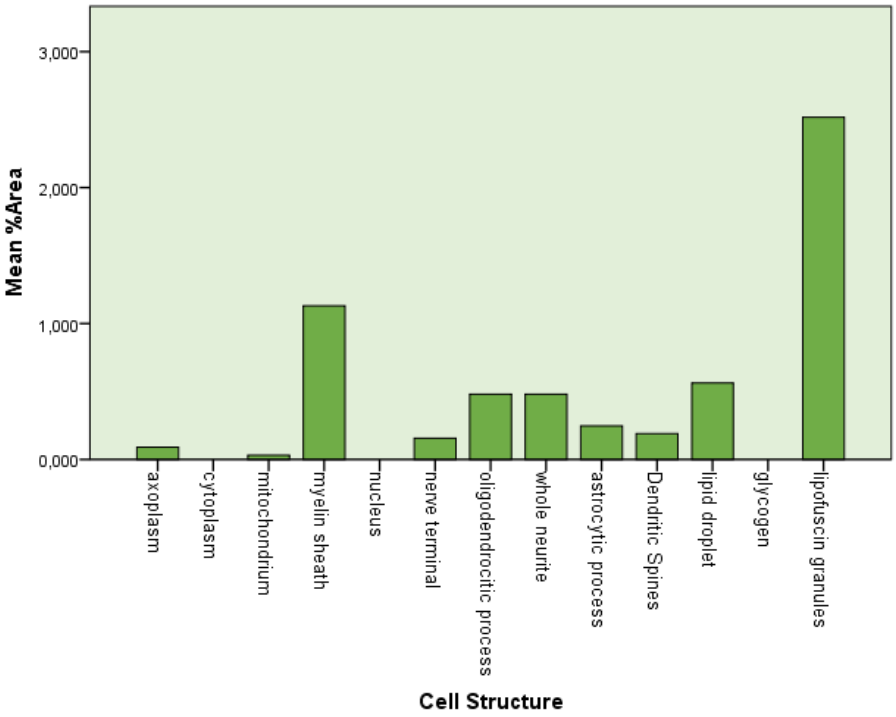

Figure 97: Bar Graph of Mean Summary % Areas of all Structures
Nucleus and glycogen were excluded from bar graph as both were only observed in 1 image. The abundance in unsaturated fatty acids in lipofuscin granules, myelin sheaths and lipid droplets might have resulted in an accumulation of osmiumtetroxide as observed with the iron M peak used for sample images.

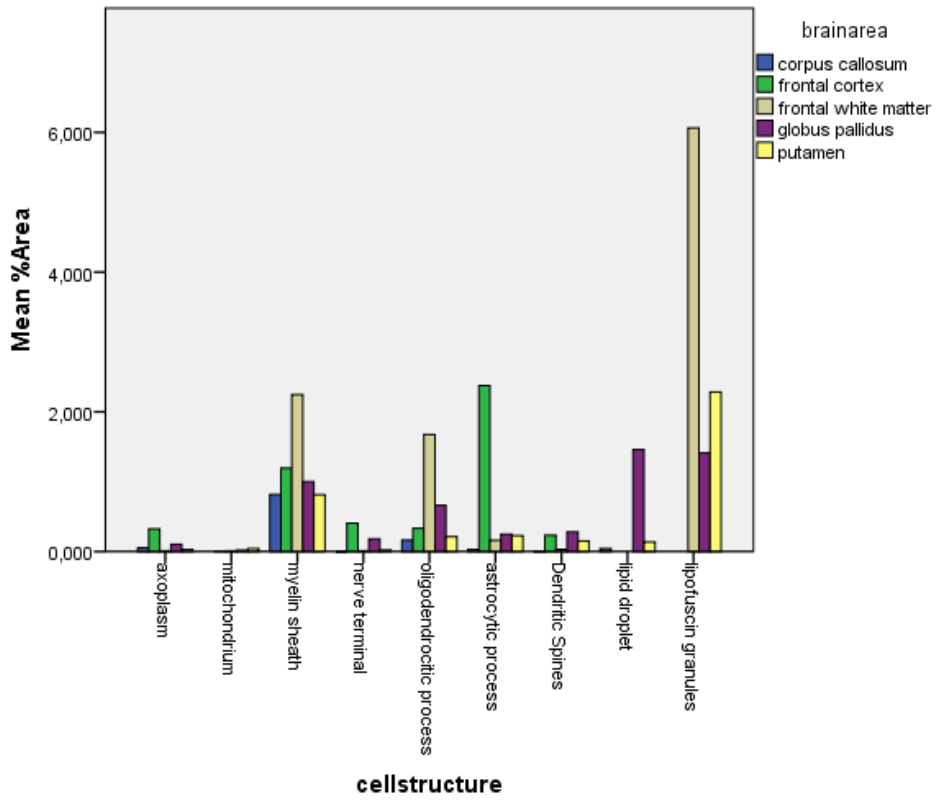

Figure 98: Bar Graph of % Areas of all Structures in Brain Areas
Nucleus and glycogen were excluded from bar graph as both were only observed in 1 image.

6 Discussion

The methodology used and elaborated within the presented feasibility study resulted in a workflow that will be suitable for the actual study with few adaptations or corrections. Therefore, by working with the techniques used in the upcoming study, several distinct points and recommendations have emerged in order to improve the workflow of the actual research on iron accumulation and prevent methodological errors. These recommendations will be presented in the current section.

6.1 Statistical Considerations

Analysis of example datasets exported by DATEM involved mainly descriptive statistics, i.e. mean/standard deviation/frequencies of specified cell types, underlying structures and the brain area. In order to apply inferential statistics, all means from the cell iron counts would have to be arranged as individual sets with each overlying brain in a row in order to avoid *pseudoreplication*. This term was first introduced by Hurlbert in 1984 (89) and describes the fact that replicate samples in experiments are often treated as if they individually act as single experimental units, although they are dependent on each other either by spatiotemporal affinity, physical interconnection and/or are actually multiple measurements from a single unit (90). Apparently, all cells from each individual brain are inter-dependent and therefore – in case of inferential statistics - must be treated as multiple measurements of the same N, conterminously the original brains they were taken from. ***Table 61*** and ***Table 62*** on the next page elaborate this thought on the basis of sample statistical datasets.

Table 61: Sample Dataset for First Descriptive Analysis

The following example dataset shows each colored cell structure with corresponding brain, brain area, cell type and cell structure in a single row. The red brackets **(A)** imply that any inferential statistics applied to this type of initial dataset would constitute pseudo-replication, as cells are in reality not separated unities, but are linked to their brain area and the overlying brain as an individual subject, which have to be treated as categorical variables (brain id, brain area) in the current dataset.

imageid	brainid	brainarea	celltypes	cellstructure	Total Area	Average Size	%Area
100	178	CC	2	7	0	0	0
100	178	CC	4	8	842,012	60,144	0,382
101	178	CC	2	5	1248,656	35,676	0,390
101	178	CC	2	11	373,388	62,231	0,134
101	178	CC	2	8	0	0	0
102	178	CC	1	12	158,727	26,455	0,044
102	178	CC	1	10	766,427	47,902	0,102

A

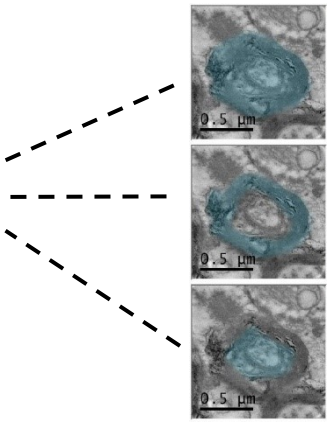

Table 62: Sample Dataset for Final Inferential Statistics

Schematic example dataset shows how final inferential statistics should be conducted on a newly created dataset depending on the first. Means of percentage areas of the descriptive statistics datasets should be obtained by structure and brain region according to their individual brains and are to be summarized as outlined below. Finally, each row should represent one individual brain in order to perform a "*within subjects*" **(B)** and a "*between subjects*" **(C)** analysis. "*Within subjects*" constitute differences in the dependent repeated measures means from within one brain (brain area - here between corpus callosum (CC) – axon (AX) – myelin sheath (MS) area percentage and the same structure analysis of the frontal cortex (FC)) - differences in iron content in brain regions. "*Between subjects*" would include differences between healthy control and i.e. brains suffering from neurodegenerative disorders (here implementation of "healthy control" as categorical variable with i.e. group 1 and other brains with i.e. positive Gallyas-Braak staining as group 2).

B

brainid	age	group	CC-ax-nrt%	CC-ax-ms%	CC-ax-axp%	FC-ax-nrt%	FC-ax-ms%	FC-ax-axp%
001	66	1	0,123	373,388	62,231	1125,361	125,040	3674,745
002	87	1	0,382	158,727	26,455	8426,557	142,823	47,249
003	74	2	0,390	766,427	47,902	8346,174	149,039	8248,743
004	68	1	0,087	7144,980	170,119	80,383	26,794	211,858
005	89	2	0,134	6708,183	172,005	1663,775	75,626	100,594
006	72	2	0,044	335,182	111,727	7107,064	88,838	58,329
007	70	1	0,102	697,663	139,533	8435,657	147,994	23,624

C

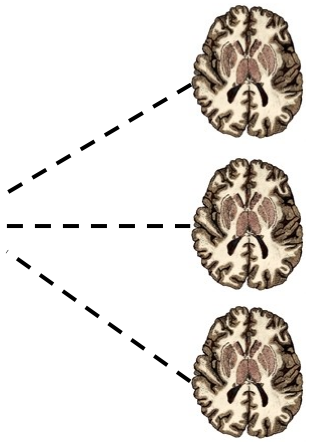

Taking the mean values of % areas for the proposed inferential statistics as displayed in ***Table 62*** will result in data loss. Therefore, it could be advantageous to implement certain derived variables, such as the range of % area per structure and brain area, as well as the maximum. In addition, strong focus has to be put on how to handle outliers, as they will ultimately affect each individual mean value. In regards to the measures of central tendencies, the median could additionally be used in the analysis. The main point however should be the avoidance of pseudo-replication in the given research when applying inferential statistical models.

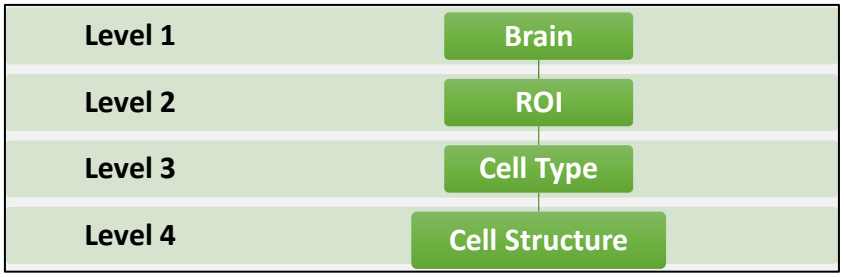

Figure 99: Hierarchical structure of the research

The different levels of the given hierarchy can be found in ***Figure 99***. ***Figure 100*** shows the hierarchical level structure of a sample taken from the frontal cortex in further detail of the lower levels involved. Cell structure determination plays an essential role for the descriptive statistics, individual values however become irrelevant in the inferential analysis.

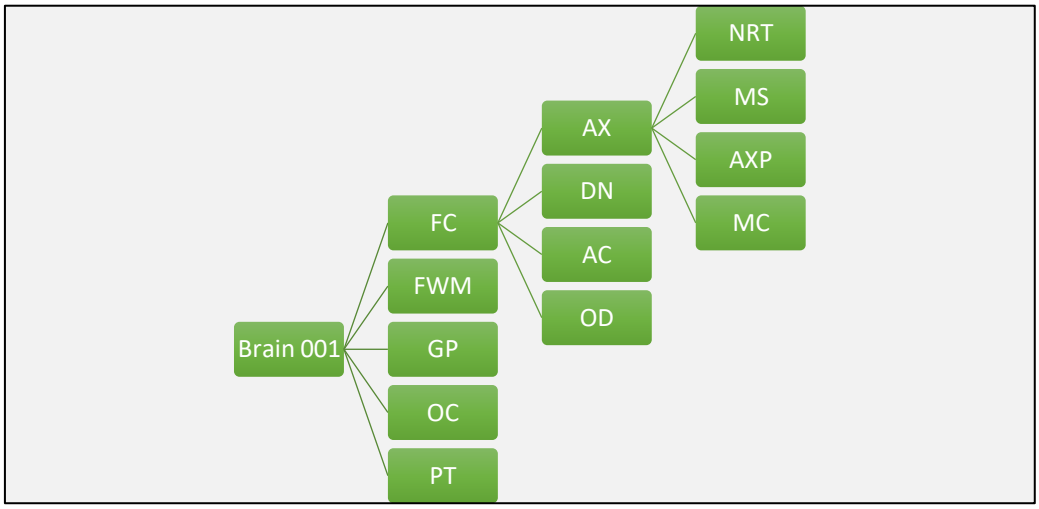

Figure 100: Example of hierarchical structure of a sample

6.2 Brain Samples

The role of iron accumulation under ischemic conditions has long been proposed in preclinical animal studies (91). As the human brain samples are taken from deceased individuals, the time between death, extraction and fixation of samples may prove detrimental to the validity of the findings of iron accumulation seen due to death-induced stagnation of perfusion and its resulting global cerebral ischemia. These implications raise the question on how accurate iron quantifications of a deceased brain can be applied to the amount present in-vivo. Therefore, predefined timeframes between sample extraction and fixation should be computed within in the study protocol. These timeframes should be kept by all involved parties, starting from patient autopsy to the possible time of sample extraction to the period of fixation of samples taken. For all deceased patients, the time should be noted, so that potential deviations in structural preservation according to timeframes of sample preparation may be subsequently discussed. Ultrastructural changes of mitochondria, such as swelling after cerebral ischemia, have been described in the literature (92) and were visible in various brain regions (see ***Figure 70***). However, for the upcoming research it is not clear which percentage of mitochondrial deformation was induced by the period of time between subject death and sample fixation or was already present at time of death.

Furthermore, an appropriate sample size should be calculated prior to study start to ensure that inferential statistics can be applied to the experiment. It remains pivotal to enforce essential documentation of sample obtaining procedures via pre-defined forms, which include time and date of sample extraction, receipt at involved institutes, time of sample preparation, etc. Despite the fact of having brain samples of deceased who were neurologically non-impaired, the importance of thorough documentation of demographics and medical history has to be stressed. Especially when it comes to the patient's age, the possibility of potential stratification in subsequent inferential statistics might be of interest.

The selection of certain brain regions should be expanded, i.e. for quantifications of brain iron in regions associated with AD, such as hippocampal structures and the motor cortex (93). Uniform random sampling methods may provide an unbiased form of obtaining specimens from various regions of interest. Especially as the numerical density of iron will be an endpoint, every brain part dissected should obtain the same probability of being included in the research (94).

6.3 Recommendations for Methodology

An article from 2012 published in Nature journal called for optimization of methodology in research (95). Within the article, reporting standards for study design were elaborated. Even though presented for animal research studies, most points can be transposed to any research being conducted. To cite the article, the following core set should be implemented as present in ***Table 63***.

Table 63: "A core set of reporting standards for rigorous study design", Landis et. al

Landis et al: "A call for transparent reporting to optimize the predictive value of preclinical research"	
Randomization	*Animals should be assigned randomly to the various experimental groups, and the method of randomization reported.*
	Data should be collected and processed randomly or appropriately blocked.
	Blinding
	Allocation concealment: the investigator should be unaware of the group to which the next animal taken from a cage will be allocated.
	Blinded conduct of the experiment: animal caretakers and investigators conducting the experiments should be blinded to the allocation sequence.
	Blinded assessment of outcome: investigators assessing, measuring or quantifying experimental outcomes should be blinded to the intervention.
	Sample-size estimation
	An appropriate sample size should be computed when the study is being designed and the statistical method of computation reported.
	Statistical methods that take into account multiple evaluations of the data should be used when an interim evaluation is carried out.
Data handling	*Rules for stopping data collection should be defined in advance.*
	Criteria for inclusion and exclusion of data should be established prospectively.
	How outliers will be defined and handled should be decided when the experiment is being designed, and any data removed before analysis should be reported.
	The primary end point should be prospectively selected. If multiple end points are to be assessed, then appropriate statistical corrections should be applied.
	Investigators should report on data missing because of attrition or exclusion.
	Pseudo replicate issues need to be considered during study design and analysis.
	Investigators should report how often a particular experiment was performed and whether results were substantiated by repetition under a range of conditions.

Despite the utopia of a completely ideal setting for research, the following steps may be taken to improve methodology when referring to Landis et al. (95):

Randomization

1. ***"Animals should be assigned randomly to the various experimental groups, and the method of randomization reported."***
   As there is no administration of medication, etc. this does not apply to the current research methodology.

2. ***"Data should be collected and processed randomly or appropriately blocked."***
   Implementation of uniform random sampling procedures for the dissection of brain regions was already elaborated in ***section 6.2***. To go down further in the clustered data hierarchy of the study, a similar process could be established for the selection of cells when acquiring electron microscope images. To reduce any bias on which structures are examined, automated selection according to raster pitches could be considered to generate grid maps, or a random number generator for coordinates could be implemented as used in research conducted by Reichmann et al (94). After setting up predefined experimental conditions and settings manually, programmed application macros could take over manual coordination.

3. ***"Blinding"***
   As all brains are derived from neurologically healthy individuals, and positive Gallyas-Braak staining will be visible to the observer, no efficient blinding can be performed in the research.

4. ***"Allocation concealment: the investigator should be unaware of the group to which the next animal taken from a cage will be allocated."***
   There is no separate allocation of any treatment; therefore this point does not apply to the current research methodology.

5. ***"Blinded conduct of the experiment: animal caretakers and investigators conducting the experiments should be blinded to the allocation sequence."***
   Does not apply to the current research.

6. ***"Blinded assessment of outcome: investigators assessing, measuring or quantifying experimental outcomes should be blinded to the intervention."***
   As elaborated under "blinding", all brains belong to the healthy control group and Gallyas-Braak staining will be visible to the examiners. Therefore, no blinding can be applied.

7. ***"Sample-size estimation"***
   For general part of the study, sample size of brains needed for proper conduct of inferential statistical analysis is to be computed.

8. ***"An appropriate sample size should be computed when the study is being designed and the statistical method of computation reported."***
   Especially when considering the avoidance of pseudoreplication within the hierarchy explained in ***section 6.1***, in-depth discussion on sample size calculation is to be considered regarding potential inferential statistics in upcoming research.

9. ***"Statistical methods that take into account multiple evaluations of the data should be used when an interim evaluation is carried out."***
   No interim analysis is planned for the upcoming study conduct.

Data Handling

1. ***"Rules for stopping data collection should be defined in advance."***
   After sample size calculation, the number of brain samples per group and approximate end of the research can be defined.

2. ***"Criteria for inclusion and exclusion of data should be established prospectively."***

   Exclusion and inclusion criteria could apply to age of the deceased people (i.e. patient age <50 years are to be excluded, time between autopsy and brain extraction should be less than 12 hours, etc.).

3. ***"How outliers will be defined and handled should be decided when the experiment is being designed, and any data removed before analysis should be reported."***

   With regards to the type and methodology of research, an exact definition of outliers prior to image analysis is not recommended, except for previously distinct i.e. erroneous EFTEM maps and/or unidentifiable structures which match exclusion criteria. The most reasonable procedure would be to then look at analysis data after transmission to DATEM for maximum values in % area via the data management feature to see whether any clearly faulty data were overlooked. Additionally, outliers to be potentially excluded can be looked for their validity after image analysis and transmission of data to SPSS. Generation of box plots for observed structures seems like the most reasonable point to figure out extreme outliers and check consistency of obtained data.

4. ***"The primary end point should be prospectively selected. If multiple end points are to be assessed, then appropriate statistical corrections should be applied."***

   For the electron microscopy part of the study, endpoints will, predictably, mainly involve the % area (metric variable) and - if feasible and replicable with upcoming in-depth particle analysis procedures – the mean size of ferritin cores.

5. ***"Investigators should report on data missing because of attrition or exclusion."***

   Function of categorization of exclusion criteria for excluded images is given for DATEM at this point. In case EFTEM elemental map seems irrational i.e., this feature can come into play.

6. ***"Pseudo replicate issues need to be considered during study design and analysis."***

   When conducting final inferential analysis according to recommendations in ***section 6.1***, pseudo-replication can be avoided within the research.

7. ***"Investigators should report how often a particular experiment was performed and whether results were substantiated by repetition under a range of conditions."***

   This point implies that "*a statistically significant result does not provide information on the magnitude of the effect and thus does not necessarily mean that the effect is robust*" (95). Assuming, for example, that statistically significant differences in iron content between regions of brains can be found, the electron microscopic results can as well be correlated with findings of the MRI part of the study (Bravais-Pearson correlation, backed by scatter charts).

6.4 Categorization of Cells/Structures

Difficulties arose at some time points on the correct categorization, especially regarding overlying cell type of observed structures, leading either to an uncertain evaluation (likely/unlikely) or exclusion (undefinable cell type). In order to avoid problems in differentiation, it is vital that all areas in TEM view should be taken with a small magnification of either light microscope or maximum of 5 k first to obtain a clear overview of the area.

For categorization of structures, preferably at least two reviewers should be present for the judgement of structure categorizations next to the uploading user. In addition, each reviewer should be blinded for the other party's decision on observed structures. This can not only prevent assignment of erroneous structures, but may - when looked at after inconsistencies after first review – give additional rise to discussion regarding structures where no distinct consensus has been found between examiners after the first review cycle. Furthermore, inter-

reliability of the raters could be measured by applying Cohen's Kappa to a nominal scale (each for cell type and cell structure variables).

6.5 Process after Image Acquisition

For the upcoming study, coloring with Adobe Photoshop CS3 is not recommended, as several images were excluded due to erroneous coloring. Preferably, boundaries of cell structures present should only be drawn within the image analysis application and saved as an image file, so that the selection is reproducible for other users. If boundaries were not drawn correctly and therefore cannot be verified by the reviewer, then the individual images can be excluded or updated.

6.6 Outlook

The upcoming research may play a pivotal role in the possibility of revealing iron involvement in neurodegenerative diseases by applying multidisciplinary procedures. Eventually, EFTEM may provide an additional path of further exploring the role of iron accumulation in the brain, especially when it comes to finding differences on the nanometer scale between healthy aging individuals and patients suffering from neurodegenerative diseases. Nevertheless, the biggest challenge of EFTEM lies in the thorough compliance with an in-depth protocol on standardized settings for observations.

7 Conclusion

Electron Microscopy Techniques

Validation of EFTEM procedures with EDX is feasible and the spectrum analysis is able to reflect iron content visible in the elemental maps. In combination with standardized procedures of acquisition and subsequent particle analysis, EFTEM is suitable for detection of iron particles in biological samples. However, focus must be put on a possible overlap with other elements. Therefore, the iron M map used for sample images within this diploma thesis does not seem appropriate due to its close peak to osmium, and osmium-tetroxide was applied in the process of tissue sample fixation. For future research, elemental mapping should implicitly be performed with the iron L peak instead, if osmium-tetroxide is used as a fixative.

Utilization of Image Database

Using Microsoft Access is generally controversial amongst developers. Nevertheless, Access allows the quick creation of back-end as well as the front-end of complex applications at absolutely minimal costs (i.e. Office 365 account), also providing a seamless compliance with other Office applications (i.e. MS Excel). Overall, DATEM gave a reasonable and comprehensible overview of all sample images obtained and was constantly easy to adapt according to any needs identified during image acquisition process.

Particle Analysis

Although Fiji /Image J offers a lot of additional plugins by developers, difficulties arise when having to handle multiple image files at once. This is however a prerequisite, as both elastic image and elemental map have to be open concurrently in order to transpose the drawn region of interest onto the elemental map for analysis. For terms of facilitation, it might be advantageous to equivocate on other image analysis applications for the research.

Sample Image Analysis

Given the fact that an interference may be given between iron M and Osmium O map, any supposed iron content has to be regarded as putative and was therefore referred to as transition metal content. By far the most transition metal content was traceable within lipofuscin granules, their related lipid droplets and within axonal structures, especially the myelin sheath. As the possibility of significant overlaps between Osmium O map and iron M map is given, it cannot be ruled out that the abundant accumulation of transition metal content within high-lipid content structures such as the myelin sheath, lipid droplets and lipofuscin granules might be linked to lipid-binding characteristics of osmiumtetroxide (84), rather than its true iron content. Despite the overlaps and inconsistencies in EFTEM peaks which were identified (see ***chapter 5.2***). It will be interesting to see in which way results of the upcoming main study might potentially reflect the sample image analysis after corrective actions have been implemented.

8 References

1. Koeppen AH. The history of iron in the brain. Journal of the neurological sciences. 1995;134 Suppl:1-9.
2. Ke Y, Ming Qian Z. Iron misregulation in the brain: a primary cause of neurodegenerative disorders. The Lancet Neurology. 2003;2(4):246-53.
3. Zecca L, Youdim MB, Riederer P, Connor JR, Crichton RR. Iron, brain ageing and neurodegenerative disorders. Nature reviews Neuroscience. 2004;5(11):863-73.
4. MacKenzie EL, Iwasaki K, Tsuji Y. Intracellular iron transport and storage: from molecular mechanisms to health implications. Antioxidants & redox signaling. 2008;10(6):997-1030.
5. Prado EL, Dewey KG. Nutrition and brain development in early life. Nutrition reviews. 2014;72(4):267-84.
6. Conrad ME, Umbreit JN. Iron absorption and transport-an update. American journal of hematology. 2000;64(4):287-98.
7. Waldvogel-Abramowski S, Waeber G, Gassner C, Buser A, Frey BM, Favrat B, et al. Physiology of iron metabolism. Transfus Med Hemother. 2014;41(3):213-21.
8. Hurrell R, Egli I. Iron bioavailability and dietary reference values. The American journal of clinical nutrition. 2010;91(5):1461S-7S.
9. Abbaspour N, Hurrell R, Kelishadi R. Review on iron and its importance for human health. Journal of research in medical sciences : the official journal of Isfahan University of Medical Sciences. 2014;19(2):164-74.
10. Munoz M, Villar I, Garcia-Erce JA. An update on iron physiology. World J Gastroenterol. 2009;15(37):4617-26.
11. Meguro R, Asano Y, Odagiri S, Li C, Shoumura K. Cellular and subcellular localizations of nonheme ferric and ferrous iron in the rat brain: a light and electron microscopic study by the perfusion-Perls and -Turnbull methods. Archives of histology and cytology. 2008;71(4):205-22.
12. Conrad ME, Umbreit JN, Moore EG. Iron absorption and transport. The American journal of the medical sciences. 1999;318(4):213-29.
13. Connor JR, Menzies SL. Cellular management of iron in the brain. Journal of the neurological sciences. 1995;134 Suppl:33-44.
14. Moos T, Morgan EH. Transferrin and transferrin receptor function in brain barrier systems. Cellular and molecular neurobiology. 2000;20(1):77-95.
15. Mills E, Dong XP, Wang F, Xu H. Mechanisms of brain iron transport: insight into neurodegeneration and CNS disorders. Future medicinal chemistry. 2010;2(1):51-64.
16. Li L, Fang CJ, Ryan JC, Niemi EC, Lebron JA, Bjorkman PJ, et al. Binding and uptake of H-ferritin are mediated by human transferrin receptor-1. Proceedings of the National Academy of Sciences of the United States of America. 2010;107(8):3505-10.
17. Fisher J, Devraj K, Ingram J, Slagle-Webb B, Madhankumar AB, Liu X, et al. Ferritin: a novel mechanism for delivery of iron to the brain and other organs. American journal of physiology Cell physiology. 2007;293(2):C641-9.
18. Quintana C, Bellefqih S, Laval JY, Guerquin-Kern JL, Wu TD, Avila J, et al. Study of the localization of iron, ferritin, and hemosiderin in Alzheimer's disease hippocampus by analytical microscopy at the subcellular level. Journal of structural biology. 2006;153(1):42-54.
19. Gao G, Chang YZ. Mitochondrial ferritin in the regulation of brain iron homeostasis and neurodegenerative diseases. Frontiers in pharmacology. 2014;5:19.
20. Santambrogio P, Biasiotto G, Sanvito F, Olivieri S, Arosio P, Levi S. Mitochondrial ferritin expression in adult mouse tissues. The journal of histochemistry and cytochemistry : official journal of the Histochemistry Society. 2007;55(11):1129-37.

21. Moos T, Rosengren Nielsen T, Skjorringe T, Morgan EH. Iron trafficking inside the brain. Journal of neurochemistry. 2007;103(5):1730-40.
22. Connor JR, Benkovic SA. Iron regulation in the brain: histochemical, biochemical, and molecular considerations. Annals of neurology. 1992;32 Suppl:S51-61.
23. Skjorringe T, Burkhart A, Johnsen KB, Moos T. Divalent metal transporter 1 (DMT1) in the brain: implications for a role in iron transport at the blood-brain barrier, and neuronal and glial pathology. Frontiers in molecular neuroscience. 2015;8:19.
24. Ji B, Maeda J, Higuchi M, Inoue K, Akita H, Harashima H, et al. Pharmacokinetics and brain uptake of lactoferrin in rats. Life sciences. 2006;78(8):851-5.
25. Yuan X, Zhang L, Wang S, Ou Y, Wang Q, Peng W, et al. Mitochondrial apoptosis and autophagy in the process of adipose-derived stromal cell differentiation into astrocytes. Cell Biol Int. 2016;40(2):156-65.
26. Marques F, Sousa JC, Sousa N, Palha JA. Blood-brain-barriers in aging and in Alzheimer's disease. Molecular neurodegeneration. 2013;8:38.
27. Batista-Nascimento L, Pimentel C, Menezes RA, Rodrigues-Pousada C. Iron and neurodegeneration: from cellular homeostasis to disease. Oxid Med Cell Longev. 2012;2012:128647.
28. Daugherty A, Raz N. Age-related differences in iron content of subcortical nuclei observed in vivo: a meta-analysis. NeuroImage. 2013;70:113-21.
29. Altamura S, Muckenthaler MU. Iron toxicity in diseases of aging: Alzheimer's disease, Parkinson's disease and atherosclerosis. Journal of Alzheimer's disease : JAD. 2009;16(4):879-95.
30. Hidalgo C, Nunez MT. Calcium, iron and neuronal function. IUBMB life. 2007;59(4-5):280-5.
31. Hidalgo C, Carrasco MA, Munoz P, Nunez MT. A role for reactive oxygen/nitrogen species and iron on neuronal synaptic plasticity. Antioxidants & redox signaling. 2007;9(2):245-55.
32. Borges Fortes A. [Hallervorden-Spatz disease, anatomical and clinical contribution]. Rev Med Rio Gd Sul. 1947;3(15):149-61.
33. Rouault TA. Iron metabolism in the CNS: implications for neurodegenerative diseases. Nature reviews Neuroscience. 2013;14(8):551-64.
34. Brewer GJ. Iron and copper toxicity in diseases of aging, particularly atherosclerosis and Alzheimer's disease. Experimental biology and medicine. 2007;232(2):323-35.
35. Smith MA, Harris PL, Sayre LM, Perry G. Iron accumulation in Alzheimer disease is a source of redox-generated free radicals. Proceedings of the National Academy of Sciences of the United States of America. 1997;94(18):9866-8.
36. Jiang H, Wang J, Rogers J, Xie J. Brain Iron Metabolism Dysfunction in Parkinson's Disease. Molecular neurobiology. 2016.
37. You LH, Li F, Wang L, Zhao SE, Wang SM, Zhang LL, et al. Brain iron accumulation exacerbates the pathogenesis of MPTP-induced Parkinson's disease. Neuroscience. 2015;284:234-46.
38. Barbosa JH, Santos AC, Tumas V, Liu M, Zheng W, Haacke EM, et al. Quantifying brain iron deposition in patients with Parkinson's disease using quantitative susceptibility mapping, R2 and R2. Magnetic resonance imaging. 2015;33(5):559-65.
39. Visanji NP, Collingwood JF, Finnegan ME, Tandon A, House E, Hazrati LN. Iron deficiency in parkinsonism: region-specific iron dysregulation in Parkinson's disease and multiple system atrophy. Journal of Parkinson's disease. 2013;3(4):523-37.
40. Lee DW, Andersen JK. Iron elevations in the aging Parkinsonian brain: a consequence of impaired iron homeostasis? Journal of neurochemistry. 2010;112(2):332-9.
41. Craelius W, Migdal MW, Luessenhop CP, Sugar A, Mihalakis I. Iron deposits surrounding multiple sclerosis plaques. Arch Pathol Lab Med. 1982;106(8):397-9.

42. Stephenson E, Nathoo N, Mahjoub Y, Dunn JF, Yong VW. Iron in multiple sclerosis: roles in neurodegeneration and repair. Nature reviews Neurology. 2014;10(8):459-68.
43. Bartzokis G, Sultzer D, Cummings J, Holt LE, Hance DB, Henderson VW, et al. In vivo evaluation of brain iron in Alzheimer disease using magnetic resonance imaging. Archives of general psychiatry. 2000;57(1):47-53.
44. Lanciego JL, Luquin N, Obeso JA. Functional neuroanatomy of the basal ganglia. Cold Spring Harbor perspectives in medicine. 2012;2(12):a009621.
45. Crossman AR. Functional anatomy of movement disorders. Journal of anatomy. 2000;196 (Pt 4):519-25.
46. Bartzokis G, Tishler TA. MRI evaluation of basal ganglia ferritin iron and neurotoxicity in Alzheimer's and Huntingon's disease. Cellular and molecular biology. 2000;46(4):821-33.
47. Wallis LI, Paley MN, Graham JM, Grunewald RA, Wignall EL, Joy HM, et al. MRI assessment of basal ganglia iron deposition in Parkinson's disease. Journal of magnetic resonance imaging : JMRI. 2008;28(5):1061-7.
48. Trepel M, Dalkowski K. Neuroanatomie: Struktur und Funktion. Neuroanatomie: Struktur und Funktion: Elsevier Health Sciences Germany; 2011. p. 208.
49. Purves D, Augustine GJ, Fitzpatrick D, al. e. Projections to the Basal Ganglia. Neuroscience, 2nd Edition: Sinauer Associates; 2001.
50. Gittis AH, Berke JD, Bevan MD, Chan CS, Mallet N, Morrow MM, et al. New roles for the external globus pallidus in basal ganglia circuits and behavior. The Journal of neuroscience : the official journal of the Society for Neuroscience. 2014;34(46):15178-83.
51. Morris CM, Candy JM, Oakley AE, Bloxham CA, Edwardson JA. Histochemical distribution of non-haem iron in the human brain. Acta anatomica. 1992;144(3):235-57.
52. Telford R, Vattoth S. MR anatomy of deep brain nuclei with special reference to specific diseases and deep brain stimulation localization. The neuroradiology journal. 2014;27(1):29-43.
53. Smith Y, Wichmann T. Functional Anatomy and Physiology of the Basal Ganglia: Motor Functions. In: Tarsy D, Vitek JL, Starr PA, Okun MS, editors. Deep Brain Stimulation in Neurological and Psychiatric Disorders. Totowa, NJ: Humana Press; 2008. p. 1-32.
54. Daugherty AM, Raz N. Accumulation of iron in the putamen predicts its shrinkage in healthy older adults: A multi-occasion longitudinal study. NeuroImage. 2015;128:11-20.
55. Purves D, Fitzpatrick D, Katz LC, Lamantia AS, McNamara JO, Williams SM, et al. Neuroglial Cells. Neuroscience: Sinauer Associates; 2001.
56. Lodish H, Berk A, Matsudaira P, Baltimore D, Zipursky SL, Darnell J. Section 21.1: Overview of Neuron Structure and Function. Molecular Cell Biology: W. H. Freeman; 1995.
57. Purves D, Fitzpatrick D, Katz LC, Lamantia AS, McNamara JO, Williams SM, et al. Neural Circuits. Neuroscience, 2nd Edition: Sinauer Associates; 2001.
58. Moos T, Morgan EH. The metabolism of neuronal iron and its pathogenic role in neurological disease: review. Annals of the New York Academy of Sciences. 2004;1012:14-26.
59. Hirano A. [Fine structure of neuronal and glial processes in neuropathology, a personal historical note]. Rinsho shinkeigaku = Clinical neurology. 2009;49(11):719-23.
60. Connor JR, Menzies SL. Relationship of iron to oligodendrocytes and myelination. Glia. 1996;17(2):83-93.
61. Saher G, Simons M. Cholesterol and myelin biogenesis. Sub-cellular biochemistry. 2010;51:489-508.
62. Connor JR, Menzies SL, St Martin SM, Mufson EJ. Cellular distribution of transferrin, ferritin, and iron in normal and aged human brains. Journal of neuroscience research. 1990;27(4):595-611.

63. Todorich B, Zhang X, Connor JR. H-ferritin is the major source of iron for oligodendrocytes. Glia. 2011;59(6):927-35.
64. Todorich B, Zhang X, Slagle-Webb B, Seaman WE, Connor JR. Tim-2 is the receptor for H-ferritin on oligodendrocytes. Journal of neurochemistry. 2008;107(6):1495-505.
65. Hulet SW, Heyliger SO, Powers S, Connor JR. Oligodendrocyte progenitor cells internalize ferritin via clathrin-dependent receptor mediated endocytosis. Journal of neuroscience research. 2000;61(1):52-60.
66. Sofroniew MV, Vinters HV. Astrocytes: biology and pathology. Acta neuropathologica. 2010;119(1):7-35.
67. Alvarez JI, Katayama T, Prat A. Glial influence on the blood brain barrier. Glia. 2013;61(12):1939-58.
68. Pekny M, Pekna M. Astrocyte reactivity and reactive astrogliosis: costs and benefits. Physiological reviews. 2014;94(4):1077-98.
69. Lane DJ, Robinson SR, Czerwinska H, Bishop GM, Lawen A. Two routes of iron accumulation in astrocytes: ascorbate-dependent ferrous iron uptake via the divalent metal transporter (DMT1) plus an independent route for ferric iron. The Biochemical journal. 2010;432(1):123-32.
70. Urrutia P, Aguirre P, Esparza A, Tapia V, Mena NP, Arredondo M, et al. Inflammation alters the expression of DMT1, FPN1 and hepcidin, and it causes iron accumulation in central nervous system cells. Journal of neurochemistry. 2013;126(4):541-9.
71. Wang L, Zhu M, Li X, Gui Q. [The application of Gallyas-Braak stainings in pathologic diagnosis of neurodegenerative diseases]. Zhonghua Nei Ke Za Zhi. 2002;41(2):120-3.
72. Wu JS, Kim AM, Bleher R, Myers BD, Marvin RG, Inada H, et al. Imaging and elemental mapping of biological specimens with a dual-EDS dedicated scanning transmission electron microscope. Ultramicroscopy. 2013;128:24-31.
73. Leapman RD. Detecting single atoms of calcium and iron in biological structures by electron energy-loss spectrum-imaging. Journal of microscopy. 2003;210(Pt 1):5-15.
74. Leapman RD, Sun SQ, Hunt JA, Andrews SB. Biological electron energy loss spectroscopy in the field-emission scanning transmission electron microscope. Scanning Microsc Suppl. 1994;8:245-58; discussion 58-9.
75. Winey M, Meehl JB, O'Toole ET, Giddings TH, Jr. Conventional transmission electron microscopy. Molecular biology of the cell. 2014;25(3):319-23.
76. Egerton RF. Electron energy-loss spectroscopy in the TEM. Reports on Progress in Physics. 2009;72(1):016502.
77. Hofer F, Grogger W, Warbichler P, Papst I. Quantitative Energy-Filtering Transmission Electron Microscopy (EFTEM). Microchimica Acta.132(2):273-88.
78. Seal S. Energy-filtered Electron Microscopy. Functional Nanostructures: Processing, Characterization, and Applications: Springer New York; 2010. p. 488-92.
79. Ahn CC. Quantitative Elemental Mapping. Transmission Electron Energy Loss Spectrometry in Materials Science and the EELS Atlas: Wiley; 2006. p. 82-4.
80. Company F. Principles of Interactions and Chemical Formation Tecnai Basic General Introduction.
81. Vymazal J, Brooks RA, Patronas N, Hajek M, Bulte JW, Di Chiro G. Magnetic resonance imaging of brain iron in health and disease. Journal of the neurological sciences. 1995;134 Suppl:19-26.
82. Harrison PM, Banyard SH, Hoare RJ, Russell SM, Treffry A. The structure and function of ferritin. Ciba Found Symp. 1976(51):19-40.
83. Pan YH, Sader K, Powell JJ, Bleloch A, Gass M, Trinick J, et al. 3D morphology of the human hepatic ferritin mineral core: new evidence for a subunit structure revealed by

single particle analysis of HAADF-STEM images. Journal of structural biology. 2009;166(1):22-31.
84. Stearns RC, Katler M, Godleski JJ. Contribution of osmium tetroxide to the image quality and detectability of iron in cells studied by electron spectroscopic imaging and electron energy loss spectroscopy. Microscopy research and technique. 1994;28(2):155-63.
85. Peters A. The effects of normal aging on myelin and nerve fibers: a review. J Neurocytol. 2002;31(8-9):581-93.
86. Bowley MP, Cabral H, Rosene DL, Peters A. Age changes in myelinated nerve fibers of the cingulate bundle and corpus callosum in the rhesus monkey. The Journal of comparative neurology. 2010;518(15):3046-64.
87. Peters A. The effects of normal aging on myelinated nerve fibers in monkey central nervous system. Frontiers in neuroanatomy. 2009;3:11.
88. Xie F, Liang P, Fu H, Zhang JC, Chen J. Effects of normal aging on myelin sheath ultrastructures in the somatic sensorimotor system of rats. Molecular medicine reports. 2014;10(1):459-66.
89. Hurlbert SH. Pseudoreplication and the Design of Ecological Field Experiments. Ecological Monographs. 1984;54(2):187-211.
90. Schank JC, Koehnle TJ. Pseudoreplication is a pseudoproblem. Journal of comparative psychology. 2009;123(4):421-33.
91. Selim MH, Ratan RR. The role of iron neurotoxicity in ischemic stroke. Ageing research reviews. 2004;3(3):345-53.
92. Solenski NJ, diPierro CG, Trimmer PA, Kwan AL, Helm GA. Ultrastructural changes of neuronal mitochondria after transient and permanent cerebral ischemia. Stroke; a journal of cerebral circulation. 2002;33(3):816-24.
93. Singh N, Haldar S, Tripathi AK, Horback K, Wong J, Sharma D, et al. Brain iron homeostasis: from molecular mechanisms to clinical significance and therapeutic opportunities. Antioxidants & redox signaling. 2014;20(8):1324-63.
94. Reichmann F, Painsipp E, Holzer P, Kummer D, Bock E, Leitinger G. A novel unbiased counting method for the quantification of synapses in the mouse brain. Journal of neuroscience methods. 2015;240:13-21.
95. Landis SC, Amara SG, Asadullah K, Austin CP, Blumenstein R, Bradley EW, et al. A call for transparent reporting to optimize the predictive value of preclinical research. Nature. 2012;490(7419):187-91.